THESIS FOR THE DEGREE OF DOCTOR OF PHILOSOPHY IN APPLIED ACOUSTICS

Simulating rolling noise on ballasted and slab tracks: vibration, radiation, and pass-by signals

JANNIK STEFAN THEYSSEN

Department of Architecture and Civil Engineering
Division of Applied Acoustics
CHALMERS UNIVERSITY OF TECHNOLOGY

Gothenburg, Sweden 2022

Simulating rolling noise on ballasted and slab tracks:
vibration, radiation, and pass-by signals
JANNIK STEFAN THEYSSEN
ISBN 978-91-7905-756-5

Doktorsavhandlingar vid Chalmers tekniska högskola.
Ny serie nr. 5222
ISSN 0346-718X

Department of Architecture and Civil Engineering
Division of Applied Acoustics
Chalmers University of Technology
SE-412 96 Gothenburg
Sweden
Telephone: +46 (0)31-772 1000

Cover:
"High-speed train silently moving through undulating landscape in morning mist on a spring day, oil painting", generated by DALL·E.

Chalmers Reproservice
Gothenburg, Sweden 2022

Simulating rolling noise on ballasted and slab tracks: vibration, radiation, and pass-by signals
Thesis for the degree of Doctor of Philosophy in Applied Acoustics
JANNIK STEFAN THEYSSEN
Department of Architecture and Civil Engineering
Division of Applied Acoustics
Chalmers University of Technology

Abstract

Shifting to rail-bound freight and passenger traffic is key in Europe's strategy towards transport decarbonisation. However, increasing railway traffic can increase environmental noise pollution. Rolling noise is often the dominant noise source. It originates from the interaction of the rough running surfaces of wheel and rail. Predicting rolling noise and performing acoustic optimisation of existing and new tracks requires validated, flexible, and physics-based prediction tools. This is especially relevant for the different designs of ballastless tracks, which are increasingly used for high-speed lines. Therefore this thesis aims to develop and implement a modelling approach for rolling noise in the time and frequency domain to increase understanding of sound radiation, investigate noise mitigation measures, and allow research of the perception of transients in rolling noise.

To achieve this, models for vibration in wheels and several types of ballasted and slab tracks have been implemented using the Waveguide Finite Element method. This method allows an efficient prediction of the track vibration up to high frequencies. Next, models for the sound radiation from wheel and track were implemented using adaptions of the Boundary Element method (BEM), such as the Fourier series BEM and the wavenumber domain BEM. The computational efficiency was addressed in multiple ways. Finally, an approach to simulate the sound produced at a stationary track-side receiver has been developed and implemented based on moving Green's functions. The simulations were largely implemented in in-house Python code. The ballasted and slab track dynamic models have been tuned and compared with measurements on full-scale tracks.

The developed models have been used to analyse the vibrations in track and wheel and the acoustic radiation from these vibrations. This allowed the investigation of noise mitigation measures. Further, the necessary complexity of the dynamic track model for predicting rolling noise in time domain was investigated. Two parameter studies were carried out with a focus on track design with lower noise emission. Slab tracks with booted sleepers showed a potential for noise reduction without increasing loads on the track structure. A continuous rail support lowered the radiated sound power at high frequencies. The contributions of different wheel modes to the radiated sound were investigated considering the directivity of each mode, and dominant modes were identified. The established models produce time signals usable for auralisation, which, among others, has the potential to research human perception of transients in rolling noise.

Keywords: Railway rolling noise, Numerical modelling, Time domain, Slab track, 2.5D FE/BE, Green's functions, Spherical harmonics

Preface

The work in this thesis has been accomplished from September 2017 to November 2022 at the Department of Architecture and Civil Engineering at Chalmers University of Technology within the research project VB13 “Prediction and mitigation of noise from vehicles on slab track”. It has been a part of the research activities within the Centre of Excellence Chalmers Railway Mechanics (CHARMEC). In particular, the support from Trafikverket (the Swedish Transport Administration) is acknowledged. Parts of the funding was provided by the European Union’s Horizon 2020 research and innovation programme in the projects In2Track2 and In2Track3 under grant agreements Nos 826255 and 101012456. Several simulations have been performed on resources at Chalmers Centre for Computational Science and Engineering (C3SE) provided by the Swedish National Infrastructure for Computing (SNIC).

I would like to thank my supervisor Wolfgang Kropp. Wolfgang, your support during these five years has been invaluable, both for this project and me as a person. In my project, you gave me the freedom to explore, the feeling that anything is possible, and the guidance to find my way back when I got lost. From the Fourier transform to fiskbensparkett, I’m thankful for our many discussions and your knowledgable advice. I would also like to thank Astrid Pieringer for her co-supervision. Astrid, I’m very grateful for your expertise on rolling contact modelling, your structure and organisation, your thorough proofreading, and not least for your insistence on Friday fika.

This project would not have been the same without the regular feedback from the members of my reference group. I would especially like to thank Jens Nielsen, Andreas Andersson, Martin Schilke, and Monica Waaranperä. Jens, thank you for your encouragement and expertise. Your input to this project was most valuable. Andreas, thank you for your curiosity in this project and our fruitful discussions. Thank you, Monica and Martin, I felt that you cared for me personally as much as for my project. I am grateful for the support of CHARMEC, and especially Anders Ekberg and Roger Lundén. Your dedicated and skilled work has built a knowledge hub in which my project could flourish.

Dear colleagues at Applied Acoustics, past and present, you all contribute to an environment that feels like a second home to me, and I (too) am proud to be a member of the family. Carl, thank you for all our discussions, it’s good to have someone who can relate. Börje, your kindness, empathy, and authenticity will be missed. And all your technical support, of course. Tommi, thanks for your insights on spherical harmonics.

I would also like to express my gratitude to Assoc. Prof. Shengyang Zhu and Prof. Wanming Zhai for our good cooperation when conducting the measurements in your excellent testing facility. Emil, it was a pleasure working and travelling with you. Your thorough work contributed a lot to our joint article, and I’m happy that we now know the difference between a pharmacy and a supermarket (or do we?).

My dear friends in Sweden, Germany, or wherever (looking at you, Arthur), thank you for all your support during these years. Tack, Lotte och Thomas, att jag fick känna mig hemma hos er. Meine liebe Familie, ihr seid immer mit dabei. Danke für die Sicherheit und Zuversicht, die ihr mir gebt. Katrin, tack för allt ditt stöd, förståelse, tålamod och uppmuntran. Vilken tur att jag har dig!

Stockholm, November 2022
Jannik Theyssen

Thesis

This thesis consists of an extended summary and the following appended papers.

Paper A	J. Theyssen, E. Aggestam, S. Zhu, J. Nielsen, A. Pieringer, W. Kropp and W. Zhai. Calibration and validation of two dynamic slab track modelling approaches using measurements from a full-scale test rig. *Engineering Structures* (2021).
Paper B	J. Theyssen, A. Pieringer and W. Kropp. The Influence of Track Parameters on the Sound Radiation from Slab Tracks. *Noise and Vibration Mitigation for Rail Transportation Systems* (2021).
Paper C	J. Theyssen, A. Pieringer and W. Kropp. Efficient calculation of the three-dimensional sound pressure field around a railway track. *To be submitted for international publication.*
Paper D	J. Theyssen. Towards time-domain modelling of wheel/rail noise: effect of the dynamic track model. *Contribution to the 12th International Conference on Contact Mechanics and Wear of Rail/Wheel systems, Melbourne, Australia, 4-7 September 2022.*
Paper E	J. Theyssen, A. Pieringer and W. Kropp. Optimizing components in the rail support system for dynamic vibration absorption and pass-by noise reduction. *Contribution to the 14th International Workshop on Railway Noise, Shanghai, 7-9 December 2022.*
Paper F	F. Fabre, J. Theyssen, A. Pieringer and W. Kropp. Sound Radiation from Railway Wheels including Ground Reflections: A half-space formulation for the Fourier Boundary Element Method. *Journal of Sound and Vibration* (2021).
Paper G	J. Theyssen, T. Deppisch, A. Pieringer and W. Kropp. On the efficient simulation of pass-by time signals from railway wheels. *To be submitted for international publication.*

The appended papers were prepared in collaboration with the co-authors. The planning and realisation of the measurements, the numerical simulations and the writing of *Paper A* were conducted in close collaboration with Emil Aggestam. The development of the method and implementation of the half-space BE formulation leading up to *Paper F* was carried out in collaboration with François Fabre. Thomas Deppisch enhanced *Paper G* with his advice on spherical harmonics and by writing the corresponding theory section. Elsewhere, the author of this thesis was responsible for the major progress of the work including developing the paper ideas and methodology, the numerical implementation, performing the simulations and writing of the draft.

The following publications are not included in this thesis due to an overlap in content or content going beyond the scope of the thesis:

1. J. Theyssen, A. Pieringer, and W. Kropp, An efficient simulation model for the dynamic behaviour of slab tracks at high frequencies, 20th Nordic Seminar on Railway Technology, Gothenburg, Sweden, 11.-12. May 2018 (abstract only).
2. W. Kropp, A. Aglat, J. Theyssen, A. Pieringer, The application of dither for suppressing curve squeal, Proceedings of the International Congress on Acoustics, pp. 1551-1558, 2019.
3. J. Theyssen, Modelling the acoustic performance of slab tracks, Licentiate thesis, Chalmers University of Technology, Gothenburg, Sweden, June 2020.
4. J. Theyssen, A. Pieringer, and W. Kropp, The low-noise potential of low-vibration track, in: Proceedings DAGA 2021, Vienna, Austria, 15.-18. August 2021.
5. J. Theyssen, A. Pieringer, and W. Kropp, Using track-elasticity for noise mitigation on low-vibration track, in: Proceedings DAGA 2022, Stuttgart, Germany, 21.—24. March 2022.
6. J. Theyssen, A. Pieringer, and W. Kropp, Noise and vibration mitigation on low-vibration track, 21st Nordic Seminar on Railway Technology, Tampere, Finland, 21.-22. June 2022 (abstract only).
7. W. Kropp, J. Theyssen, and A. Pieringer, The application of dither to mitigate curve squeal, Journal of Sound and Vibration, 2021.

Contents

Abstract i

Preface iii

Thesis v

Contents vii

I Extended summary 1

1 Introduction 1
1.1 The role of railway transport in the perspective of global warming 1
1.2 Railway noise pollution 2
1.3 Railway rolling noise 3
1.4 Scope of the thesis 4
1.5 Outline 6

2 Review of railway rolling noise models 7
2.1 General overview 7
2.2 Review of wheel/rail interaction models 8
2.3 Review of track models 10
2.3.1 Track vibration 11
2.3.2 Sound radiation from the track 14
2.4 Review of models for the wheels 16
2.4.1 Wheel dynamics 16
2.4.2 Wheel radiation models 18

3 Modelling track vibration and radiation 20
3.1 Vibration modelling of the track 20
3.1.1 The waveguide FE method for waves in a solid 20
3.1.2 Coupling between the rail and its support 24
3.2 Radiation from track vibration 29
3.2.1 The Wavenumber domain Boundary Element method 29
3.2.2 Methods to increase the numerical efficiency 31
3.3 Adapted inverse Fourier transforms for calculating the spatial sound pressure field 34
3.3.1 The sound field around a vibrating rail 34
3.3.2 The sound field produced by a vibrating sleepers 36
3.4 Sound of a passing force on a rail 42

4 Modelling wheel vibration and radiation **45**
4.1 Vibration modelling of the wheel 45
4.2 Radiation from wheel vibration 46
4.2.1 Radiation from a wheel in free space 47
4.2.2 Radiation from a wheel above a reflective plane 48
4.3 Sound of a passing wheel 49
4.3.1 Sound radiation from wheel modes 49
4.3.2 Spherical harmonics decomposition of wheel radiation 50
4.3.3 Prediction of pass-by signals 51

5 Applications of the model **54**
5.1 Modelling the dynamic response of a ballasted track 54
5.1.1 Model setup and parameters 55
5.1.2 Comparison to measured receptances 56
5.2 Modelling and calibrating the dynamic response of a slab track 59
5.2.1 Measurement setup 59
5.2.2 Model and tuning of modelling parameters 60
5.2.3 Comparison between measurements and the calibrated model 60
5.3 The sound power radiated by a slab track with varying rail pad stiffnesses and rail supports 63
5.3.1 Description of the model 63
5.3.2 Sound power produced by rail and slab surface 64
5.4 Addressing slab track vibration and noise performance with a two-stage elastic support 65
5.4.1 Model description and study parameters 65
5.4.2 Parameter study results and noise mitigation potential 67
5.5 Description and interpretation of precalculated acoustic transfer functions . . 69
5.5.1 Description of the acoustic geometries 69
5.5.2 Presentation and analysis of the acoustic transfer functions for a rail in free space 71
5.6 3D sound field produced by a harmonic force on a ballasted track 73
5.6.1 Description of the modelling parameters 73
5.6.2 Sound radiation from a discretely supported rail 73
5.6.3 Sound radiation from rigid, elastically supported sleepers 76
5.7 The influence of the dynamic track model on the predicted sound field 79
5.7.1 Modelling approaches for the track vibration 79
5.7.2 Comparison of the acoustic performance of the different dynamic track models 79
5.8 The structural vibrations of a railway wheel 85
5.9 Validity of a simplified half-space approximation for radiation from railway wheels 88
5.10 The radiation directivity of wheel modes and their contributions to the pass-by sound pressure 92
5.10.1 Directivity of wheel modes 93

5.10.2 Modal contribution to pass-by sound pressure 93

6 Conclusions and Future Work **99**
6.1 Simulation of track vibrations and sound radiation 99
6.1.1 An advanced model to predict railway track vibration and radiation 99
6.1.2 The acoustic performance of different track designs 100
6.2 Simulation of wheel vibrations and sound radiation 102
6.2.1 The use of WFE, FBEM and moving Green's functions for simulating sound radiation from the wheel 102
6.2.2 The stationary and pass-by sound radiated by a wheel 103
6.3 Future work towards a combined simulation tool for railway rolling noise . . . 103

7 Summary of the appended papers **105**

References **109**

A Appendix to Chapter 3 **122**
A.1 Optimisation of the spatial inverse Fourier integral for the rail 122
A.2 Validation of the method for calculating the 3D sound field from 2D solutions 125
A.3 Modelling railway sleepers flush with the surrounding plane 127

II Appended Papers A–G 131

List of Figures

1.1 Overview over thesis chapters, modules, and papers. 5
2.1 Typical procedure estimate rolling noise in simulations. 8
2.2 Components in a ballasted and slab track system included in the review. . 11
2.3 Characterisation of wheel modes. 17
3.1 Orientation of the coordinate system in the WFE method. 20
3.2 Discretised cross-section of the UIC60 rail geometry. 21
3.3 Cross-sectional deflections of selected wave types in the rail. 21
3.4 Dispersion relation of the waves in a free UIC60 rail. 22
3.5 Frequency dependent phase speed of the waves in a free UIC60 rail. . . . 23
3.6 Rail support configurations a to g. 25
3.7 Discrete coupling in configuration a and b. 26
3.8 Discrete coupling in configuration c and d. 28
3.9 Relation between K, κ, and α. 30
3.10 Mapping between f_n and f_0 for selected whole wavenumbers. 32
3.11 Visualisation of the precalculation of the acoustic transfer functions H_a. . 34
3.12 Normal velocity on top of a rail head over frequency and wavenumber. . . 35
3.13 Example velocity profile along the length of the track. 37
3.14 Normal velocity slice v_n over the length of the considered track section. . 37
3.15 Sleeper velocity profile over space and frequency, for an excitation at $x = 0$ m. 38
3.16 Vertical velocity profile of the track in the wavenumber-frequency domain. 39
3.17 Velocity profile $v(\kappa, \omega)$ limited to $\kappa < K$. 40
3.18 Velocity profile $v(x, \omega)$ limited to $\kappa < K$. 40
3.19 Process steps to calculate the pass-by signals given the transfer functions. 42
3.20 Aligning IRs with a moving force to compute a pass-by pressure signal. . 43
4.1 The curved waveguide model of the wheel. 45
4.2 Position of wheel and receiver points in the FBEM calculation. 50
4.3 Axis definition and position of the wheel and stationary microphone. . . . 52
5.1 Measured and simulated vertical transfer functions of the ballasted track. 57
5.2 Measured and simulated lateral transfer functions of the ballasted track. . 58
5.3 Cross-section of the CRTS-III track. 59
5.4 Locations of accelerometers and excitations in the measurement. 60
5.5 FE nodes of the cross-section of the slab track model. 61
5.6 Difference between predicted and measured TFs, vertical excitation. . . . 61
5.7 Difference between predicted and measured TFs, lateral excitation. 62
5.8 Model setup for the discretely and continuously supported rail. 63
5.9 Radiation from a 20 cm slab for different rail pad stiffnesses k_s. 64
5.10 Rail and slab contribution to total sonud power. 65
5.11 Radiating track surfaces including rail, sleepers, and slab. 66
5.12 Influence of support parameters on peak forces $\hat{F}_c$, $\hat{F}_a$, and $\hat{F}_b$. 67
5.13 Sound power radiated from the different components for different k_a. . . . 68

5.14 Dynamic maximum forces compared L_W for various track parameters. . . 69
5.15 Pre-calculated BE geometries. 70
5.16 Setup (iv) for which the acoustic transfer functions were evaluated. 70
5.17 TF from rail surface to a circle of receiver points. 71
5.18 TF from rail surface to receiver points at different frequencies. 72
5.19 TF from each source element on a rail the surface of the rail. 72
5.20 Rail and sleeper deflection and radiated sound pressure along the track. . 74
5.21 Wavenumber spectra of the rail receptance, relative to wavenumber in air. 76
5.22 Sound field surrounding a vibrating rail. 77
5.23 Sound field surrounding a vibrating sleeper. 78
5.24 Track models included in the study. 80
5.25 Difference in L_W radiated by analytical and WFE rail models. 81
5.26 Difference in L_p produced by analytical and WFE rail models. 82
5.27 Location at which the impulse responses are evaluated. 82
5.28 Decay of L_p in a line along the track. 83
5.29 Decay of L_p produced by a WFE-based rail that is acoustically free in space. 83
5.30 Comparison of impulse responses at 1 m and 64 m for different tracks. . . 84
5.31 Spectrogram of sound pressure at a stationary microphone during the pass-by. 85
5.32 Lower part of the wheel cross-section. 86
5.33 Dispersion relation of the eigenfrequencies of the wheel. 86
5.34 Vibrational mode shapes of the wheel. 87
5.35 Radial input mobility of the wheel. 87
5.36 Axial input mobility of the wheel. 88
5.37 Cross-mobility of the wheel. 88
5.38 Radiation ratio σ for different numbers of nodal diameters. 89
5.39 Radiation ratio σ for different heights of the reflective plane. 90
5.40 Comparing radiation ratios for the radiation into free field and half space. 90
5.41 Calculated L_p in free field and half-space. 91
5.42 Comparing mirror-source approximation and coupled half-space solution. 92
5.43 Directivity of the axial mode (1,0,a) for different frequencies. 94
5.44 Directivity of the axial mode (3,1,a) for different frequencies. 95
5.45 Contribution of each mode to L_p during the wheel pass-by. 96
5.46 Contribution of each mode to $L_{\mathrm{p,eq,1s}}$. 97
5.47 Effect of removing the contribution of a single mode on the $L_{\mathrm{p,eq,1s}}$. . . . 97
5.48 Spectrogram of a the pass-by sound pressure at a stationary microphone. 98
A.1 Example distribution of integration points around $k_c = 4$ rad/m. 122
A.2 The indicator for the quality of integration F for $n_{\mathrm{ip}} = 101$. 124
A.3 Quality of integration in dependency of n_{ip}. 125
A.4 Cross-section of the setup for the 2D/3D validation. 125
A.5 Calculated pressure at one field point. 126
A.6 Comparison of the mean difference at all field points. 127
A.7 Cross-section of the 3D BE model. 128
A.8 Radiation efficiency σ for different heights of the sleeper. 128

A.9 Directivity of a rectangular piston protruding an infinite baffle. 129
A.10 Maximum difference in L_p over frequency and angle. 129

List of Tables

5.1 Modelling parameters to match the measured input receptance. 55
5.2 Study parameters 66
A.1 Parameters for continuously supported Euler-Bernoulli rail 123
A.2 Parameters used in the genetic algorithm 125

List of Symbols

c	Speed of sound waves in air
d	Sleeper spacing
e	Euler's number, 2.71828...
f	Frequency
f_s	Sampling frequency
g	Impulse response
h_n	Spherical Hankel function of order n
i	Indexing variable
j	Unit imaginary number, solution to $x^2 + 1 = 0$
k	Spring stiffness of a linear elastic spring
l	Indexing variable
m	Mass or SH-degree
m'	Mass per unit length
n	SH-order
o	Observer position
p	Sound pressure
q	Source strength
r	Radius
t	Time
u	Element nodal displacement
v	Vehicle velocity
v_n	Surface normal velocity
w	Width of a sleeper
x, y, z	Cartesian coordinate system
θ, y, r	Cylindrical coordinate system
$\mathbf{n}$	surface normal vector
$\mathbf{p}$	Vector of surface pressures
$\mathbf{u}$	Vector of nodal displacements
$\mathbf{v}$	Vector of nodal velocities
$\mathbf{v}_n$	Vector of surface normal velocities
$\mathbf{x}$	Coordinate in Cartesian or cylindrical coordinates

A	Cross-sectional area
A_l	Modal amplitude
C	BEM coefficient
E	Young's Modulus
F	Force
G	Green's function in 3D
H	Heaviside step function
$\mathrm{H}_0^{(2)}, \mathrm{H}_1^{(2)}$	0^{th} and 1^{st} order Hankel function of second type
H_a	Acoustic transfer function
H_d	Dynamic transfer function
H_{da}	Coupled dynamic and acoustic transfer function
H_l	Modal acoustic transfer function of mode l
I	Second moment of inertia
K	Wavenumber in air
L_p	Sound pressure level
L_W	Sound power level
N	Number of discrete connections between the rail and its support
Y_n^m	Spherical harmonics of order n and degree m
$\mathbf{A}$, $\mathbf{C}$, $\mathbf{G}$	Coefficient matrices in the WBE method
$\mathbf{K}$, $\mathbf{M}$	Stiffness and mass matrix in the WFE method
α	Wavenumber in 2D cross-section
$\alpha_a, \alpha_b, \alpha_c,$ $\alpha_f, \alpha_r, \alpha_s$	Receptances in the discrete support
η	Damping loss factor
π	Ratio of a circle's circumference to its diameter, 3.14159...
κ	Wavenumber in x- or θ-direction
κ_n	Eigenvalue in the WFE system of equations
ρ	Density
σ	Radiation ratio
ξ	Index of interval in semi-analytical integration
ω	Angular frequency, $\omega = 2\pi f$
ζ_l	Modal damping ratio for mode l
Φ	Eigenvector (Φ_L - left; Φ_R - right)
Ψ	Fundamental solution to 2D Helmholtz equation
Γ	2D boundary of a structure
Λ_l	Modal mass of mode l
Ξ	Number of intervals in semi-analytical integration

Part I
Extended summary

1 Introduction

1.1 The role of railway transport in the perspective of global warming

The United Nations recognise sustainable transport as one of the key topics for reaching the sustainable development goals, as “transport is [...] a means allowing people to access what they need: jobs, markets, goods, social interaction, education, and a full range of other services contributing to healthy and fulfilled lives.” [1]. Between 2015 and 2050, the worldwide demand for passenger travel and goods transport is projected to more than double [2, 3]. The International Transport Forum (ITF) predicts that, even if all current commitments to decarbonise transport are fully implemented, this doubling will lead to a 16% increase in greenhouse gas (GHG) emissions by 2050 compared to 2015 [3]. One difficulty in decarbonising transport is that more than 90% of all transport is currently based on oil products [4]. Both the ITF and the International Energy Agency (IEA) stress that ambitious decarbonisation policies could reduce the transport GHG emissions significantly closer towards reaching the goal of the Paris Agreement [2, 3].

In the European Union (EU), the transport sector consumes about 31% of the total energy, 93% of which are used on the road. In 2019, the transport sector produced 25.8% of EU GHG emissions, followed by the energy industries (24.1%) and the manufacturing and construction industry (20.7%)[5][1]. While in other sectors, GHG emissions have decreased by 20% to 45% with respect to 1990, emissions from the transport sector have increased by about 30%. Increased civil aviation and road traffic are the largest drivers for the increased GHG emissions [5]. In response, the European Commission aims to reduce GHG emissions from transport by 60% by 2050 compared to 1990 [7]. The key goals are to shift 50% of road freight to rail or water transport and to achieve the majority of medium-distance intercity passenger travel by rail, because of the higher energy efficiency of railway transport: Today, railway freight transport constitutes 12% of freight transport (road 52%, sea 29%) and 7% of passenger traffic (passenger cars 71.6%, buses 8.1%, air 9.7%) in the EU [5]. However, rail transport produces only 0.4% of direct emissions and the increasing electrification of the railway network combined with the increasing share of renewable sources in the energy mix leads to low indirect emissions [8][2].

The envisioned shift towards rail-bound traffic is substantial. The EU projects that both freight transport and passenger rail will increase by 79% from 2010 to 2050 [9]. According

[1] similar in the United States, with 27%, 25%, and 24%, respectively [6]

[2] Worldwide, rail networks carry 8% of passengers and 7% of freight but use only 2% of energy [2].

to this projection from 2013, 37% of passenger traffic will be high-speed in 2050. In the last decade, global traffic on high-speed railway lines has grown substantially, from 245 billion passenger-km (pkm) in 2010 to 956 billion pkm in 2018, largely a result of extensive expansion of the Chinese high-speed rail network [10].

This shift entails large secondary challenges. In many countries, not limited to Sweden [11], the existing railway network is at its capacity limits. Construction of new railway lines requires energy and a change of land use. Global cement production is the third largest source of anthropogenic carbon dioxide emissions, after fossil fuels and change in land use [12]. Even so, land use per passenger-km by rail is about 3.5 times lower than for passenger cars [13], and "building new railway lines saves CO_2 after one to three decades" [14]. However, the secondary challenges related to increasing railway traffic are not limited to GHG emissions.

1.2 Railway noise pollution

Traffic noise is a major health concern. The World Health Organisation (WHO) estimates that more than a million healthy human live years are lost, every year, in western Europe alone [15]. For Sweden, a 2017 study estimates this number to be 41 033 years, 90% of which are related to road traffic and 10% of which are due to railway traffic [16]. Especially sleep disturbances due to night-time noise have significant long-term effects on the cardiovascular system [15, 17].

The effect of noise on humans is measured by indicators such as L_{den}, a noise indicator used to assess annoyance during day, evening, and night, and L_{night}, which is used to assess sleep disturbance. These parameters measure a long-term average exposure on residents as defined in ISO 1996-1:2016(E) [18]. The WHO recommends an exposure of less than or equal to ($L_{\mathrm{den}}/L_{\mathrm{night}}$) 53/45 dB for road traffic, 54/44 dB for rail, 45/40 dB for air traffic. However, more than 18 million people are exposed to noise levels (L_{den}) larger than 55 dB due to railway traffic (road transport 100 million, air transport 4 million) [19]. The indicator L_{den} increases with an increasing number of trains per day on a given track. In combination with the intended shift to rail transport, a reduction in L_{den} /L_{night} can only occur by reducing or absorbing the noise radiated by individual vehicles and tracks, or by diverting some of the traffic to other or new routes.

Indicators like L_{den} correlate human annoyance with a daily average noise level exposure, which is the standard approach. However, Kaku and Yamashita show that impact noise can increase the perceived loudness of train noise by 3 dB to 7 dB, depending on impact and listening condition, at the same equivalent sound energy level [20]. For investigating human annoyance of impact noise, a modelling tool is desirable that can predict the sound of various impacts occurring on railway tracks (switches and crossings, rail defects, wheel flats, etc.) in time domain. A lack of adequate modelling approaches for impact noise was recently pointed out [21, 22].

Several sources of railway noise exist, including rolling noise, curve squeal, noise from bridges, aerodynamic noise, signal noise (horns, bells, warning signals at level crossings), fan noise and other noise from stationary vehicles, and shunting noise [23]. Rolling noise is the dominant noise source for most moving vehicles and is therefore the focus of this work.

1.3 Railway rolling noise

Railway rolling noise describes the audible noise generated by the wheels, the rail, and other components of the track when a train vehicle moves along a track. Rails and wheels are also involved in the generation of other types of noise, such as squeal noise and aerodynamic noise, but they have different excitation mechanisms. The excitation mechanism for rolling noise can be described as follows. The source of rolling noise is the dynamic interaction of wheel and rail, which can be understood as follows. The static load of the vehicle locally deforms the wheel and rail into an extended area of contact, the contact patch. The surface irregularities on the wheel and the rail, typically described as surface roughness, create a complex pattern of interacting peaks and troughs in the contact patch. The rolling motion of the wheel then leads to continuously new combinations of peaks and troughs, causing dynamic foces that lead to local deformation and vibrations in the wheel and rail [24, 25]. The properties of the vehicle, the track, and the contact determine the proportion of local deformation to component vibration and the relation between the vibration of different components.

This vibrational energy will either decay in these structures due to the material damping, be transmitted into supporting structures (such as the sleepers or the wheel suspension), or will be radiated as airborne sound. Although the transfer to airborne noise constitutes only a small portion of the losses of vibrational energy, the noise levels produced are high enough to have kept researchers, engineers, and policymakers busy for decades.

Rolling noise is speed dependent. It increases with vehicle speed and dominates the noise produced by a passing train up to about 300 km/h [26, 23]. At higher vehicle speeds, the aerodynamic noise radiated from the vehicle becomes more important. Below about 50 km/h, the noise from the engine, fans, and other onboard equipment dominates.

Different components contribute to the noise in different frequency ranges, for two reasons. Firstly, the mobility of the contact spring, the wheel, and the rail in the contact influence the relative vibration levels of the wheel and the rail [23]. The mobility of the wheel, for example, varies significantly over frequency, due to the lightly damped modes. Secondly, the radiation is influenced by the components' radiation efficiency, which depends, among others, on their shape and dominating vibration pattern. For a typical prediction of a ballasted track using the TWINS model, Thompson observed that the radiation from the sleeper vibration contributes in the frequency range up to about 250 Hz, above which the rail is the main source of noise up to about 1500 Hz, above which the wheel dominates [23]. Railway ballast can absorb some of the airborne noise above about 1000 Hz, but its vibration also excites sound waves in the surrounding air below 300 Hz [27].

Railway tracks without ballast (ballast-less tracks or slab tracks) are often described as producing higher levels of rolling noise. The difference to ballasted track is not only due to the lack of ballast absorption, as simulations show [28, 29, 30]. The rail support stiffness of slab tracks is typically lower compared to ballasted tracks, which means that the rail is more decoupled from the sleepers, allowing vibrations in the rail to propagate further [23]. Consequently, higher noise emissions are expected. The combined effect of lack of ballast absorption and higher vibration levels on the rail is predicted to increase the noise by 2 dB(A) to 4 dB(A) [28, 29, 30, 31]. This prediction is confirmed by measurements comparing sound pressure levels produced by trains on different tracks in several European countries [32, 31].

One way to imitate the dynamic properties of ballasted tracks on slab tracks is using elastically mounted sleepers. For example, Diehl et al. [28] propose such a system with monoblock sleepers. Their patented design reduces rail vibration firstly via a stiff connection between the sleepers and the rail, and secondly by introducing a damping layer in the sleeper, providing additional damping at the sleeper resonances [33]. Calculations in the software RIM show that the sound contribution of the rail decreases with (i) a stiffer coupling between rail and sleepers, (ii) with an increased damping in the coupling, and (iii) with an increased damping of the the sleeper resonances [34]. Track designs with individual booted sleepers can have similar dynamic properties.

In general, relying on measurements for quantifying the differences between track types implies that certain parameters can not be controlled for, such as rail/wheel roughness. These shortcomings can be overcome in numerical modelling approaches. However, here the predicted difference strongly depends on the initial assumptions about the track, such as the rail roughness and the track decay rate [35]. Further, a validated model for the surface vibrations of the slab is necessary. Modelling approaches for slab surface vibration and sound radiation have only recently been developed, one of which is presented in this thesis.

1.4 Scope of the thesis

The aim of this thesis is to develop a modular tool for the simulation of rolling noise in the time and frequency domain. The tool should be flexible enough to adapt to different track designs and detailed enough to capture the physical processes of rolling noise generation, in a frequency range relevant to human perception. The physics-based modelling chain, capturing relevant quantities from wheel and rail roughness over component vibration to sound pressure, should give insight into the processes of the generation of noise by, and vibrations in the structures. Still, the tool should allow conducting parameter studies with feasible numerical cost to, for example, compare different track designs or investigate noise mitigation measures. The time domain calculation of the pressure signals should allow an auralisation of the pass-by to facilitate investigating the effect of impulsive and continuous noise on human perception.

This thesis describes such a modular modelling approach aimed at calculating component

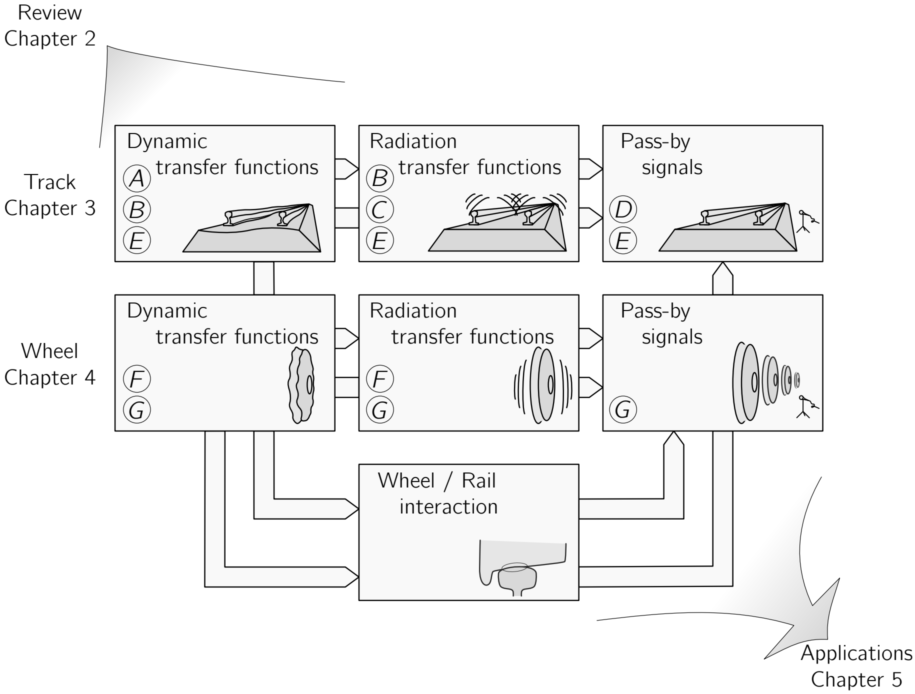

Figure 1.1: Structure of the thesis: Relation between chapters 2 to 5, papers A to G, and modules in the proposed model for rolling noise.

vibration and sound radiation. A special focus lies on the modelling of slab track vibration and sound radiation. Different types of models for slab track and ballasted track are developed. Modules are validated by comparison to analytical models, laboratory tests, and full-size measurements. Parametric studies are carried out with the aim of investigating the influence of track parameters on the sound radiation from different track designs. Finally, a physics-based time domain approach to model railway rolling noise is proposed.

It should be noted that this thesis does not cover modelling the vehicle-track interaction and thus excludes rolling contact modelling or vehicle dynamics simulations. Instead, an existing model is used to predict the rolling contact force due to roughness excitation in the time domain [25]. This thesis focusses primarily on the sound generation mechanism. Consequently, air-borne and structure-borne sound propagation into the vehicle or into buildings are not covered.

1.5 Outline

The extended summary consists of seven chapters. This first chapter introduces the topic, scope, and outline of the thesis.

Chapter 2 reviews the existing railway rolling noise models and components relevant to the model presented in the following chapters. It follows the structure presented in Figure 1.1 in that it reviews vibration in and radiation from tracks and wheels. It also provides a short review of wheel/rail interaction modelling approaches.

Chapter 3 summarises the modelling approach for railway track vibrations and radiation, involving methods developed in papers A to E. The first module predicts the dynamic transfer functions of the track, describing the structure-borne displacement reaction to a normalised excitation force. Here, a modelling approach for slab track surface vibration is introduced (cf. *Paper A*). Furthermore, a dynamic model for a two-stage elastic support, involving elastically booted sleepers on a flexible slab, is presented (cf. *Paper E*). Track vibrations can serve as input to the next module, covering radiation transfer functions. Radiation transfer functions describe the sound pressure produced at a receiver point by a normalised surface deflection. A combined model for sound radiation from the slab surface and the rail is developed (cf. *Paper B*), and a method for the efficient prediction of the sound radiation from track vibrations via precalculated transfer functions is shown (cf. *Paper C*). Finally, a modelling approach is introduced for the sound pressure signal produced by a force passing on a rail (cf. *Paper D*).

Chapter 4 outlines the modelling approaches for wheel vibration and radiation developed in papers *F* and *G*. The first module introduces a waveguide-based approach to the vibration modelling of the wheel (cf. *Paper F*). Then, radiation transfer functions are calculated using Boundary Element theory and equivalent sources (cf. *Paper G*). Finally, a method for predicting the sound radiated by the wheel modes in the time domain is presented (cf. *Paper G*).

Chapter 5 summarises results and applications of the modelling approach, for example, the parameter studies in *Paper B* and *Paper E* addressing noise mitigation measures using existing track components.

Chapter 6 concludes the extended summary and provides an overview of future research.

Chapter 7 provides a brief summary of the appended papers.

2 Review of railway rolling noise models

This section first gives a general overview on concepts used in railway noise modelling. Then modelling approaches for the interaction between the wheel and the rail are reviewed in Section 2.2. The subsequent Sections 2.3 and 2.4 present existing research on vibration and radiation of the track and wheels, respectively.

2.1 General overview

Railway rolling noise is generally simulated with one (or combinations) of three methods: Empirical models, analytical models, and numerical models. Empirical models predict the radiated sound based on measured data sets, such as combined roughness, vehicle assembly, and speed, as for example the CNOSSOS model [36]. Relevant quantities are estimated via standardised transfer functions and correction terms. These models only allow a limited insight into the physical processes behind the sound generation. In addition, they are based on a certain set of data from existing designs. Design solutions not contained in this data set are not covered by such models. Thus empirical models are not a suitable choice for the scope of this thesis.

Analytical models simplify the problem to elementary geometries, such as beams or plates. The mechanical and acoustical behaviour of these geometries is predictable via analytical expressions. A typical example is modelling the dynamic behaviour of the rail by using a beam model [37]. Measured data solely serves the purpose of tuning model parameters or validating the model. These models can be very useful to gain insight into generic cases, but the required simplifications are often a hinder to investigate more realistic cases.

Numerical models estimate the mechanical and acoustical behaviour of structures by dividing the problem into smaller, simpler parts which can again be described analytically. A solution for the entire problem is then found by connecting these simpler parts. Numerical modelling approaches thus allow for more complex problems in terms of geometry and material properties, often exceeding the limitations of analytical modelling approaches. Relating to the example above, the rail dynamic behaviour has also been modelled in a numerical approach [38, 39].

Railway rolling noise can be modelled in the time or frequency domain. Regarding the modelling of the wheel/rail interaction, Knothe and Grassie [40] remark that frequency domain models were the dominant modelling approach up to the 1970s, as they typically come with a lower computational cost. Time-domain models have since been increasingly used to investigate nonlinear effects in the wheel/rail interaction [39, 41, 25].

Analogously to expressing the temporal information in the frequency domain, a spatial dimension can be decomposed in the wavenumber domain. This approach can lead to significant gains in computational efficiency and is often used in the context of vibration and radiation of rail tracks [42]. Also the vibration and radiation of wheels can be

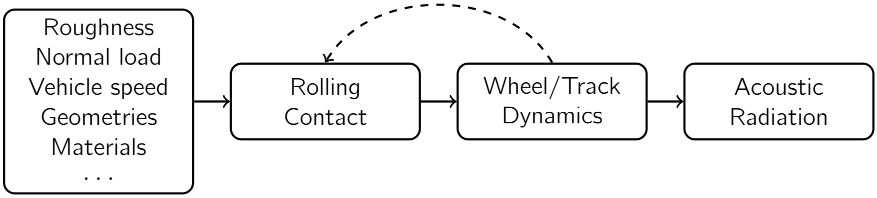

Figure 2.1: Typical procedure estimate rolling noise in simulations (adapted from [45]).

expressed in terms of wavenumbers [43, 44].

Estimating the total radiated sound typically involves four iterative steps as shown in Figure 2.1. The first step is to define the relevant properties of the interaction, the wheel, and the track. The rolling contact forces are estimated with these input parameters, taking into account the dynamic response of wheel and track at the contact. In turn, the contact forces excite vibrations on the wheel and the rail. The vibrations in the components also affect the contact forces, however, this feedback can only be considered in a time domain approach. In time domain, the nonlinearity of the contact [25, 45] can be considered, while a frequency domain approach demands a linearisation of the contact.

Only a few models cover the whole modelling chain, for both tracks and wheels, due to the complexity of each submodule. One prominent such model is the TWINS model [46, 47]. In [48], Thompson and Jones present a brief description of the TWINS model, together with a comprehensive summary of other research activities before the year 2000. Since then, several new modelling approaches have been developed for each sub-module. Often, different modelling approaches within a sub-module can produce valid inputs to the succeeding simulation steps. The following review is thus structured in the order of these submodules, starting with a brief overview on contact models followed by simulation approaches for the dynamic and acoustic behaviour of tracks and wheels.

2.2 Review of wheel/rail interaction models

The rolling surfaces of the rails and wheels are not perfectly smooth. When a wheel rolls over a rail, their combined roughness leads to a temporal variation of the pressure in the contact patch between wheel and rail. The varying pressure induces structural vibrations in the wheel and the rail, and a part of this vibrational energy is radiated into the surrounding air. Modelling this dynamic interaction between the vehicle and the track is central for researching the interaction forces and loads on the components, rolling surface wear, corrugation of the rail, out-of-round wheels, and the generation of rolling noise [49]. The dynamic vehicle/track interaction is extensively reviewed by Knothe and Grassie [40] and more recently, Connolly et al. [50]. Models aiming for, for example, running stability, curving behaviour, and ride comfort focus on the frequency range up to 20 Hz, often with modelling approaches involving multi-body dynamics [40, 51, 31, 50]. Rolling noise, however, is more high-frequent, which means that the involved wavelengths are shorter and the interacting components and the contact need to be modelled in more detail.

The high-frequency wheel/rail interaction can be modelled in the time domain or in the frequency domain. Frequency-domain models assume a linear dynamic response of the vehicle and the track and linearise the processes in the contact zone to a contact stiffness. The combined roughness of the wheel and the rail is expressed as a roughness spectrum, where each spectral component excites a vibration at the corresponding frequency.

A large number of frequency-domain modelling approaches exist. Knothe and Grassie [52] provide a comprehensive overview of the early developments that were, among others, pioneered by Remington [53, 54, 55]. This modelling approach was later advanced by Thompson [24, 56, 38, 57, 58], leading to the development of the TWINS software [46, 47].

Including non-linear behaviour in the contact requires a time-stepping solution, since at every time step, the model state is a function of the preceding time steps. This solution strategy is usually computationally more costly compared to frequency-domain approaches. A lack of high-frequency non-linear models for rolling noise prediction was pointed out by Thompson and Jones [48] in the year 2000, with computational cost being one challenge, as rolling noise predictions require an upper frequency limit of several kHz as discussed below. Models developed earlier for investigating corrugation, simulating the wheel-rail interaction in the time domain, worked only up to about 1.5 kHz [40]. There was also an interest in researching impact noise, to which frequency domain models are of limited use. Several approaches to solve the vertical wheel/rail interaction in time-domain exist, for example DIFF [39], which solves the problem via an extended state-space vector approach combined with a complex modal superposition technique. However, a different approach is used in this thesis and is presented in more detail in the following section.

If the vehicle and track are linear and time-invariant, their structural response can be represented by Green's functions. Green's functions, in this context, are impulse responses describing the structural response to an impact force at the contact point. This Green's functions approach is an efficient way to model the wheel/rail interaction in the time domain, because the Green's functions, being a property of the structures rather than the interaction, can be precalculated before the time-stepping computation. Introduced for modelling railway noise by Manfred Heckl [59], the approach was adopted for several subsequent studies. Nordborg [41] used a Green's functions approach to solve coupled vibrations of a moving wheel on a continuously or discretely supported track. By comparing to a linear model, he states that a time-domain model is necessary if there exists large corrugation on the rail, due to the occurring loss of contact. These results are also observed by Wu and Thompson [60], who additionally remark that a low static preload increases the risk of loss of contact, requiring a non-linear modelling approach. A further application of time-domain modelling of the contact is squeal noise, which introduces nonlinear behaviour in the contact patch [61, 62, 63]. The Green's function approach has been widely adapted [51, 25, 64, 65, 66, 66, 62, 67, 68].

The contact filter effect determines the the upper frequency limit of vibrations generated by the rolling contact interaction. It describes the effect that wavelengths which are short in comparison to the contact patch are attenuated. In numerical models, the effect can be introduced via preprocessing of the roughness spectra [69]. In a time-domain contact model as presented by Pieringer [25] the filtering effect is automatically included in the formulation of the contact, which is based on Kalker's variational method [70]. This non-Hertzian contact model considers the variation of roughness in the finite contact area. Comparing this formulation with simpler contact models such as a contact spring or a Winkler foundation, Pieringer observes that the predicted contact pressure varies significantly between the simplified and the non-Hertzian contact model, especially if the roughness is uncorrelated in lateral, parallel lines. The lower limit of the relevant frequency range for rolling noise is set by the sensitivity of human hearing, which is reduced below about 20 Hz [23, 51].

There also exist hybrid approaches to solving the wheel/rail interaction problem and the resulting sound radiation. Wu and Thompson [60] combined a time-domain model for the solution of the contact problem with a frequency-domain model for the sound radiation by translating the calculated contact pressure into an equivalent roughness. This approach was also adapted by Torstensson et al. [21] to investigate noise at railway crossings. It is pointed out that the characteristics of impact noise can not be evaluated with this hybrid approach, since the model does not predict sound pressure in time-domain but is based on averaged quantities during the pass-by.

In the context of researching transient effects on railway noise, multiple authors have pointed out the need for a physical model that allows the prediction of the sound pressure in the time domain during the pass-by of a wheel on a rail [21, 22]. Torstensson et al. [21] argue that the "total sound pressure level does not sufficiently well reflect the annoyance experienced by people exposed to impact noise from crossings". Researching the perception of transients in the wheel/rail interaction force on humans could be realised by auralising the sound field. Auralisation describes the rendering of audible sound fields, a term introduced by Kleiner et al [71] in the context of architectural acoustics. One aim of the EU-project SILVARSTAR (SoIL Vibration and AuRalisation Software Tools for Application in Railways) [72, 73] is to produce an auralisation tool to provide an immersive experience for communication with an audience outside of acoustics. The produced tool uses distributed monopoles to capture the sound radiated by different parts of the train and track based on previous work by Pieren [74] and input from the TWINS model [46, 75] to adjust the sound power of the monopoles. Those capabilities of the auralisation tool go beyond the scope of this thesis. However, fewer simplifications regarding the radiated sound field are made in this thesis when modelling main contributors to rolling noise: the rail, the sleepers or slab surface, and the wheels. The following sections summarise modelling approaches for the vibrations and radiation from these components.

2.3 Review of track models

Adapted to the particular requirements of the railway system, several different track designs exist. The review focusses primarily on tracks for freight and passenger traffic outside of cities and neglecting industrial applications, i.e., the most common ballasted

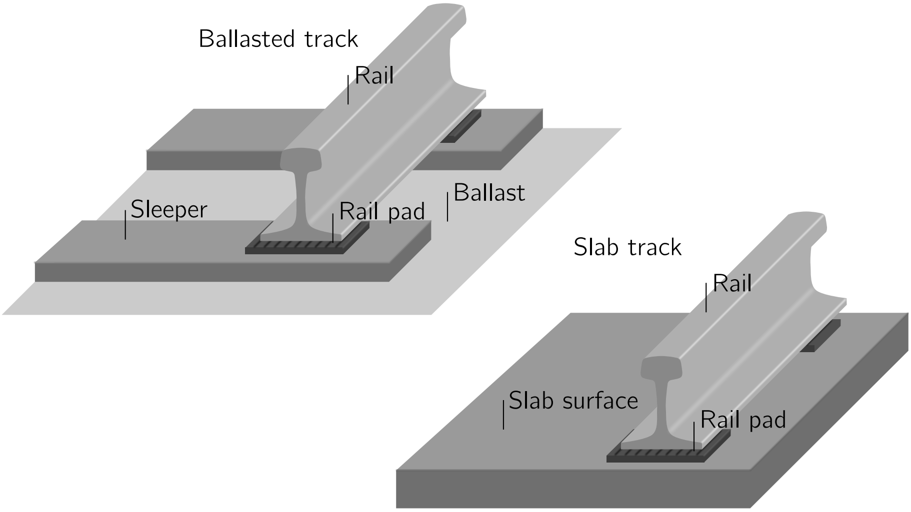

Figure 2.2: Considered components of ballasted and ballastless track systems that are included in the review.

and ballastless tracks. In ballasted tracks, the rails are supported, via rail pads, by concrete or wooden sleepers resting on a ballast layer. In ballastless tracks, also called slab tracks, ballast and sleepers are replaced by multiple supporting concrete layers. A more detailed introduction to different types of ballasted and ballasted tracks is presented in [76, 31, 77, 78].

Railway tracks are complex structures, both from a vibration and a sound radiation perspective. Therefore, modelling the vibrations and sound radiation of a railway track requires a reduction of this complexity to its central elements, presented in Figure 2.2. The rail seat is rather simplified as, among others, the clamping mechanism is omitted in the illustration and most modelling approaches. Below, models for the vibration in the structures are addressed, starting with models for the rail and then reviewing models for the supporting structures such as sleepers on ballast or the concrete panels of slab tracks. Then, models for acoustic radiation are discussed.

2.3.1 Track vibration

This section first introduces dynamic models for the rail and then covers models adapted to additionally include the dynamic behaviour of other track components such as sleepers and slab tracks.

Rail models

As early as 1926, Timoshenko published a model describing the harmonic response of the rail based on a continuously supported beam [37]. The beam model, later termed Timoshenko beam theory[3], is an analytical model based on Euler-Bernoulli beam theory that additionally accounts for the rotational inertia and shear deformation of the beam [80]. This analytical model has been widely adopted [81, 53, 52, 82, 83] and continues to be used in current studies, as it provides a good approximation of the dynamic behaviour of the rail in a wide frequency range.

Approximating the support as continuous is no longer valid when the influence of the rail seats becomes relevant. Among other effects, the discrete support leads to the pinned-pinned resonance frequency at around 900 to 1100 Hz, at which the bending wavelength equals twice the sleeper spacing, and so a bending wave field can exist almost unimpeded by the support. The support is periodic in space, which can be modelled using periodic element formulations as shown, among others, by Munjal and Heckl [84], Grassie [52], Nielsen [85], Ripke and Knothe [86], or Nordborg [41]. Mead [87] presents a summary of a part of the early work on continuous periodic structures. The support can also be modelled as a superposition of the response of the free rail and the response of the supports as presented by Maria Heckl [88, 89].

For frequencies beyond about 1.5 kHz, the cross-sectional deformation of the rail becomes relevant. Wu and Thompson [90] used two continuously supported Timoshenko-beams to model a single rail to increase the usable frequency range of this beam modelling approach. More commonly, the high-frequency response is predicted using numerical modelling approaches like the Finite Element (FE) method. Numerical approaches typically come with a higher computational cost, scaling with the dimension of the studied object. The length of the rail poses therefore a challenge to standard 3D FE models. Another issue is that FE models of finite length can create artificial reflections at the boundaries requiring appropriate measures. These challenges have been addressed in multiple ways. Again, the periodicity has been used successfully to describe high-frequency cross-sectional deflections. One downside of this approach is that it eliminates all decaying waves and is thus not well suited for describing the decay over the distance [91, 92, 93, 38].

A different FE formulation approximates the rail as an infinite waveguide with a constant cross section. The dynamic response of the rail is dominated by propagating, decaying waves along the length of the rail. Knothe et al. [94], Gavric [95], Bartoli et al. [96], and Ryue et al. [97] use methods for calculating the wavenumbers and associated cross-sectional modes of propagating waves in an unsupported rail. This method was, among others, adopted by Sheng et al. [98], Nilsson et al. [42] and Zhang et al. [99] for continuously supported rails. It also found wide application in the modelling of ground-borne vibrations [100, 101, 102, 103, 104], and for the modelling of noise from bridges [105]. This method is referred to as the Waveguide Finite Element (WFE) method, or 2.5 dimensional (2.5D) FE [4], since it assumes an infinitely long, constant cross section. As a

[3]Arguments are made it should instead be called Timoshenko-Ehrenfest beam theory [79].

[4]The abbreviation can be misleading: describing the problem in a different *d*omain does not influence

consequence, the WFE approach is inherently well suited for integrating a continuous support as for example demonstrated by Nilsson et al. [42]. A discrete support can be integrated using Heckl's superposition principle [88], which was shown by Sheng et al. [98] and Zhang et al. [99]. This WFE formulation can be combined with a standard FE model to introduce heterogeneity in the infinite track as described by Gras et al. [106]. The structure supporting the rail has a large influence on the vibration of the rail. Modelling approaches for different support types are further reviewed below.

Rail supported by sleepers on ballast

Track ballast introduces an elasticity to the dynamic track system. The infinite beam model of the rail with a continuous support can be expanded to a two-layer continuous support as described by Thompson [23]. The dynamic properties of the rail pads, sleepers, and ballast need to be evenly distributed along the rail. These three components can be combined into one frequency-dependent stiffness to which the rail is coupled when modelling a discretely supported track [88, 23].

Modelling the sleeper as a rigid mass is an approximation only valid as long as the bending wavelength in the sleeper is significantly larger than the sleeper itself. A more detailed description of sleeper vibration can be achieved with a finite Timoshenko beam model as for example shown by Grassie [107] who compares the dynamic response of a free Timoshenko beam model with measurements of resiliently suspended sleepers. Furthermore, Nielsen and Igeland [39] use a Winkler foundation to include the ballast elasticity under the sleepers, modelling different sections of the sleeper as connected beam elements.

Rail supported by slab tracks

Several models have been proposed for the structural response of a rail supported by a slab track system. One approach is to model the slab and supporting layers as Timoshenko beams [108, 109, 110, 111]. However, beam theory typically assumes that the wavelength is large compared to two dimensions of the structure. This limits the application of beam theory to relatively low frequencies. Further, non-symmetric excitation and support conditions cannot be represented by a 2D model. Such 3D effects are researched in numerical modelling approaches using Finite Elements [112, 113, 114, 115, 116]. The computational cost of solving 3D FE models is comparatively higher than the 2D beam models. One strategy to address this is to, again, assume that the slab structure acts as a waveguide and use the WFE method to solve 2D FE problems at several wavenumbers, for example presented by Zhang et al. [35, 117, 116].

Especially when researching ground vibrations, combinations of FE and Boundary Element (BE) method are common [118, 102, 119]. This modelling approach has the advantage

---

the information in that *d*imension. The '2.5D FE' method produces a description of the 3D vibration in the structure.

that the subgrade can be modelled as an elastic half-space, avoiding reflections from model boundaries.

2.3.2 Sound radiation from the track

Analogously to the section above, first models to predict the sound radiation from the rail are introduced, followed by models for the sound radiation from sleepers, ballast and slab tracks.

Radiation from the rail

The rail is the dominant source of noise on the railway track in the frequency range that is most relevant for human hearing [23]. When researching acoustic radiation from the vibration of its surface, Remington [54] proposes an analytical model assuming a line of monopoles, each scaled with the expected surface vibration of the rail. A similar approach based on equivalent-sources is implemented by Thompson et al. [46] in the software TWINS. The proposed radiation model is a 2D model. This 2D assumption was later tested by Thompson et al. [120], using two different modelling approaches to compare the radiation from a rail in 2D and 3D: the 2D model uses a 2D BE formulation, whereas the 3D model uses an array of dipole sources placed at the centre of the rail. They find that when the wavelength of structure-borne waves in the rail is long compared to the wavelength in air, the sound power radiated from a rail can be predicted using a 2D model. This is the case above 250 Hz. Below this frequency, a correction term is proposed. Further, the direction of radiation from the rail is investigated. The angle at which the sound is radiated, measured from the normal on the rail, is observed to exceed 45° when the wavelength in the structure approaches the wavelength in air.

To avoid the simplifying assumptions of equivalent sources in the 3D modelling approach, Nilsson et al. [42] use a wavenumber domain BE approach (WBE or 2.5D BE) based on earlier work by Duhamel [121] and Chandler-Wilde [122]. The WBE is similar to the WFE approach to calculate the structural response of the rail described above in that a series of 2D problems is solved for different wavenumbers along the rail instead of attempting to solve a computationally unfeasible 3D problem. Nilsson et al. [42] make use of the similarity of these calculation methods to predict the radiation from a WFE-based model for the structural vibration in a continuously supported rail. The vibration of the structure is assumed to be decoupled from the sound pressure waves in air; i.e. no backcoupling from the sound waves in air on the structural vibration is considered. This combined WFE/WBE model has been employed by Zhang et al. [123] to research the effect of ground proximity on the rail radiation efficiency. It is also possible to predict the sound pressure radiated from rails using other models for the structure-borne sound: Sheng et al. [124] use a 2.5D BE model to calculate the radiation from a Timoshenko beam-based rail model up to 3000 Hz. Li et al. [125] also apply Timoshenko beam theory for predicting the rail vibration and then predict the radiated sound field via a 2.5D BE model. The source strength of the rail sound field is in this case adapted to match the result predicted by TWINS [46]. This calculation successfully predicted the sound pressure level on the surface of a model train and a real size train, both stationary and during a pass-by. Recently, Li et al. [105] used a method entirely based on the 2.5D FE approach to investigate the radiation from the track. The FE approach requires a perfectly matched layer (PML) at the boundary of the mesh to simulate the free field radiation. This method is then used to research the sound pressure on the surface of railway vehicles in tunnels.

Ntotsios et al. [126] investigate the effect of the track unevenness and roughness on both rails. At wavelengths shorter than 3 m the two rails can be treated as uncorrelated. For calculating the sound radiated from both rails, each one can be calculated individually up to a vehicle speed of 360 km/h if the lowest frequency of interest is above 30 Hz [35].

Radiation from sleepers on ballast

Including railway sleepers in the calculation model for railway noise often implies taking two components into account: their vibration-induced sound radiation, and the absorption introduced by the porous track ballast in between.

With respect to vibration-induced sound radiation, there are several modelling approaches. Thompson [46] estimated sound radiation based on a rectangular piston in an infinite baffle, where the acoustic interaction between sleepers at low frequencies is included by a heuristic approach. Vincent et al. [127] used this approach to investigate the effect of the rail pad stiffness on the radiated sound power from sleepers. They found that a softer coupling between the rail and the sleeper led to a lower radiation from the sleeper, but an increased radiation from the rail, and suggested heavier sleepers with a smaller surface area as mitigation measure against sleeper noise. Nielsen [128] predicted the surface vibration of a monoblock sleeper based on the Rayleigh-Timoshenko beam theory on a Winkler foundation. Then, they evaluated the sound radiation from this sleeper using a BE model, placing the monoblock sleeper above a rigid ground. This approach is also used by Zhang et al. [129], who investigated the effect of several interacting monoblock sleepers. It is found that for frequencies below 100 Hz, where the rail couples several sleepers together, the sleeper's joint radiation is up to 5 dB higher compared to single sleepers. It is found that including three sleepers is sufficient to determine the radiation ratio. Li et al. [125] include sleeper radiation in a 2.5D BE formulation, however, not using discrete sleeper positions but instead using an approximation of the average spatial velocity. All these modelling approaches assume that the sleeper radiation is considered to be independent of the radiation from the rail.

The acoustic absorption of porous ballast was already researched in 1940 by Kaye and Evans [130]. There are several approaches to estimating the sound absorption properties of materials, often relying on a multitude of parameters. The model proposed by Delany and Bazley [131] is comparatively simple, as it relies only on one parameter, the flow resistivity. Other prominent models are proposed by Attenborough and Bias-Allard [132]. Attenborough [133] compared three modelling approaches to measurements of ballast absorption conducted by Heutschi et al. [134] on a double track. It is found that, while all three give reasonable results, the Delaney-Bazley method overestimates the absorption at the first ground-effect dip. Recently, Broadbent et al. [135] measured ballast absorption under laboratory and in situ conditions and found that ballast absorption is negligible at low frequencies, with an absorption factor that does not exceed 0.4 below about 700 Hz. It is further stated that an 3-layer, 4-parameter model was required for a good approximation of the frequency-dependent absorption. However, the Delany-Bazley model is still frequently used in modelling, for example by Zhang et al. [129, 123, 75], due to its simplicity.

The contribution of ballast vibration to sound radiation from the track surface has been researched in more detail by Zhang et al. [136], who found that ballast vibration can contribute significantly to sound radiation from sleepers below 300 Hz. They used a scale model and compared to measurements on full size sleepers. A method is proposed to evaluate the effect of ballast vibration on sleeper radiation by means of a Rayleigh integral.

Radiation from slab track

Model-based investigations of the sound radiated by slab track surfaces have not been the focus until recently. Van Lier [29] points out that the contribution of slab surface vibrations to the total sound is small when A-weighting the frequency-spectrum. Thompson [23] stated that the sound radiation from slab tracks is often negligible due to its high mechanic impedance. However, a recent investigation by Zhang et al. [35] finds that vibrations on the slab surface are the dominant sound source up to 100 Hz based on a numerical model. The radiation from the slab is calculated using a combined 2.5D FE/BE approach. A different approach is used by Sheng et al. [124], who calculate the sound field radiated from a baffled surface using the Rayleigh integral equation.

Similar prediction methods are applied when calculating the sound radiated by concrete bridges. Li et al. [137] develop an efficient computation approach to calculate the radiation from bridge modes. The efficiency is achieved by precalculating transfer functions from each bridge mode and using a 2D BEM calculation to calculate the 3D sound field around the bridge. The method is later used in a parameter study related to bridge noise mitigation and shows a good agreement with accompanying measurements [138].

2.4 Review of models for the wheels

2.4.1 Wheel dynamics

Modelling the dynamic response of the wheel is essential both for predicting the wheel/rail interaction and calculating the sound radiation from the wheels. Remington [53] proposed an analytical model in which the impedance of the wheel is approximated by the mass of the wheel plus one third of the axle weight up to 1000 Hz. Above 1000 Hz, the impedance

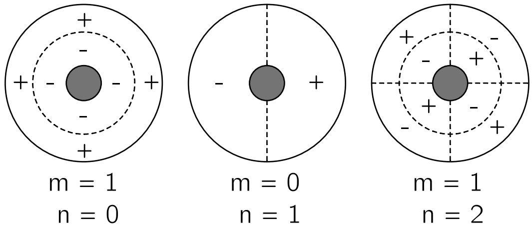

Figure 2.3: Sketch of the modes of a wheel characterized by their number of nodal diameters n and circles m, with a rigid axle in the centre.

is then approximated with an infinite beam with the same cross-section of only the wheel tread (without the web). Later, this model was revised by using the impedance of a ring [55]. Schneider and Popp [139] use a model consisting of ring elements based on Mindlin's plate theory to calculate the vibration modes of the wheel. These models can only capture the low-order vibrational modes in the structure. Thompson [56] developed a FE model using elements that take advantage of the axi-symmetry of the structure. This way, only the cross section needs to be discretised. The variation of each mode shape around the circumference is then assumed to be sinusoidal. The FE model is iteratively solved for a prescribed whole number of such sinusoidal oscillations.

The zero-crossings of this sinusoidal variation produce diameters across the wheel which are stationary, called nodal diameters. The number of nodal diameters n is used to characterise the modes. A second characteristic is the number of nodal circles m, which describes the number of stationary points along a radial line. Figure 2.3 shows some examples where the relative phase of the wheels is indicated by the plus and minus signs. The categorisation is applied to axial modes (out-of-plane direction of vibration) and radial or circumferential modes (in-plane direction of vibration). A notation later adopted by others is to describe modes as (n, m, a / r / c), with a, r, and c for the axial, radial, and circumferential modes, respectively. Thompson [56] introduces a summation of the modes to calculate the total forced response of the wheel.

Another numerical approach is to assume wave propagation in the circumferential direction, described by Nilsson [140] and Finnveden and Fraggstedt [141]. As before, the geometry and material properties of the structure are assumed to be constant along the circumference, and by using appropriate elements, only the cross-section needs to be modelled numerically. This, again, has a significant computational advantage compared to a standard 3D-FE formulation. Due to the different approach, the curved WFE model is solvable either for a prescribed number of nodal diameters or for a prescribed frequency. This has the advantage that it is possible to include nonproportional material damping. The method is thus frequently used in the context of car tyres [140, 142, 45]. The vibration response of the structure to a harmonic force is again found by modal sum.

Modelling the rotation of the wheel has been extensively studied. Thompson [58] shows that the peak at the resonance of the wheel splits into two peaks when the rotating wheel is observed from a stationary point. The two peaks, one above and one below the observed stationary resonance frequency, occur because of the forward- and backward-propagating circumferential waves. Baeza et al. use an approach based on Eulerian modal coordinates to observe these waves [143], and investigate the effect of the rotating wheel in the context of vehicle-track interaction [144, 145]. Pieringer et al. [146] compare two approaches for including the rotation of a rotating wheel, an Eulerian approach and a simplified model base on a rotating load and moving Green's functions in the context of wheel squeal, and no significant differences are observed in the considered rolling speed. Torstensson et al. [147] find large differences in the rolling force when comparing between stationary and rotating wheel models where resonance frequencies of different modes coincide due to wheel rotation. The change in the observed resonance frequency is further investigated in the context of modal veering [148, 149]. Sheng et al. [150] present a formulation for calculating the rotating wave field in wheels based on 2D axisymmetric elements.

2.4.2 Wheel radiation models

An analytical model for the radiation from railway wheels was introduced by Remington [54], building on the assumption that the primary radiating surface is the wheel web. The radiation is then assumed to be similar to a monopole, scaled according to wheel vibration levels and the assumed radiation efficiency of the wheel. Schneider and Popp [139] solve the radiated sound power and the sound pressure using a Rayleigh integral formulation, assuming that the wheel is baffled in an infinite plane. Thompson et al. [46] estimate the radiated sound power by combining average surface vibration spectra with radiation efficiencies. They observe that the number of nodal diameters affects the radiation efficiency.

Several numerical approaches exist. A BE formulation making use of the axi-symmetry have been presented by Seybert [151]. Here, the sound field and its boundary conditions are described in a Fourier expansion, similar to the WBE approach used for rails. Fingberg [152, 152] used this BE model to calculate the sound radiation from squealing wheels. He also investigated the directivity of individual mode shapes and found that the radiation efficiency is close to one for modes relevant to sound radiation. Kuijpers et al. [43] significantly improved the efficiency of this modelling approach by making use of the Fast Fourier Transform (FFT) algorithm. Thompson and Jones [44] use this BE approach to calculate the radiation ratios of several mode shapes of the wheel, and derive an engineering approximation for these ratios. They indicated that the directivity of the wheel can be approximated by monopole and dipole characteristics. Recently, the effect of a rotating wheel was investigated by using the rotating structure-borne wave field of a wheel as the input to an axi-symmetric BE formulation, among others shown by Zhong et al. [153] and Cheng et al. [154].

The models above all consider how a single wheel radiates into free space. Fabre et al. [155] adapt Kuijper's formulation so that ground reflections from a rigid ground can be included in the Fourier expansion. Multiple wheels were included by Li et al. [105], who predict the sound radiation from sleepers, rail and wheels in a straight 2.5D BE approach.

Li et al. [105] use a single monopole source to represent the radiation from the wheel. The source strength of this monopole is adjusted based on the TWINS model.

In a full 3D BE model originally developed to calculate the sound radiation of car tyres [156, 157], Zenzerovic [62] researched squealing noise. This model uses half-space Green's functions to efficiently incorporate ground reflections in the calculation. Yet, there are a large number of degrees of freedom required in this full 3D formulation. Nilsson [140] uses the curved WBE formulation introduced above to couple structural finite elements to air elements to predict the radiation from a tyre. This has the disadvantage that a perfectly matched layer is necessary to avoid reflections from the edges of the FE mesh.

3 Modelling track vibration and radiation

This chapter introduces modelling approaches for vibrations and radiation from several track types. Section 3.1 describes modelling approaches for the structural response. Approaches for modelling the sound radiation from these track types are introduced in Section 3.2. Section 3.3 introduces adapted algorithms for calculating the sound pressure in spatial domain for different track components, which is a prerequisite for Section 3.4 which presents a method to calculate the sound pressure signal produced by a contact force moving along a rail.

3.1 Vibration modelling of the track

Section 3.1.1 briefly summarises the Waveguide Finite Element (WFE) method, as it has many applications throughout this work. Then, several ways to model the coupling between the rail and its support are introduced in Section 3.1.2. Analytical models for rail vibration based on beam theory are well established and not introduced here (cf. Section 2.3.1 or [81, 158, 90, 23, 111, 159]).

3.1.1 The waveguide FE method for waves in a solid

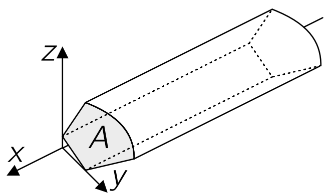

Figure 3.1: Orientation of the coordinate system in the WFE method (adapted from [42]).

Standard 3D FE models of structures as large as railway tracks can become computationally unfeasible when modelling high frequency vibrations. The WFE method makes use of the constant cross-section of the railway track along its length. Following this approach, only the 2D cross-section (A in Figure 3.1), which lies in the (y,z)-plane, needs to be discretized into finite elements. The third dimension (x) is included via a wave-type solution, assuming propagating, decaying waves.

In this work, the cross-section A is discretised using conventional 2-dimensional, nine-node, iso-parametric quadrilateral elements with quadratic polynomials as shape functions (see Figure 3.2). A stationary motion at circular frequency ω is assumed with the time dependency $e^{j\omega t}$. A matrix equation for the relationship between the element nodal displacements and the nodal forces is derived for each element by applying Hamilton's principle (see for example [42] for a more detailed derivation). Assembling the element

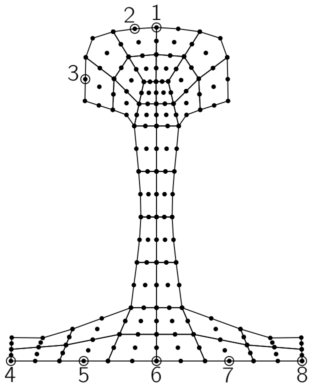

Figure 3.2: Discretised cross-section of the UIC60 rail geometry. Numbered nodes are referred to below.

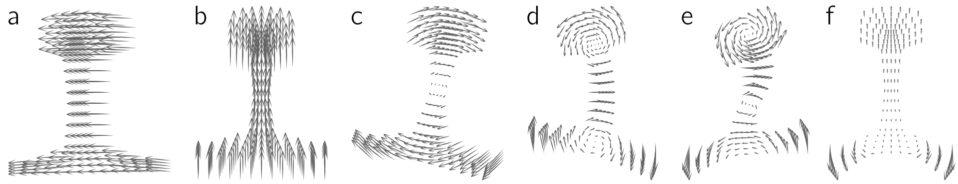

Figure 3.3: Cross-sectional deflections of selected wave types: a - lateral bending, b - vertical bending, c - torsion, d - web bending, e - head rotation, f - foot flapping.

matrices in the global matrix system gives the expression

$$\left[\mathbf{K}_2(-j\kappa)^2 + \mathbf{K}_1(-j\kappa) + \mathbf{K}_0 - \omega^2\mathbf{M}\right]\mathbf{u}(\kappa,\omega) = \mathbf{F}(\kappa,\omega) \tag{3.1}$$

with the mass matrix $\mathbf{M}$ and the vectors of the nodal displacements and forces $\mathbf{u}$ and $\mathbf{F}$, respectively. $\mathbf{K}_i$ are generalised stiffness matrices, and κ is the wavenumber. The equation has been transformed to the wavenumber domain using the Fourier transform with

$$\mathbf{u}(\kappa,\omega) = \int_{-\infty}^{\infty} \mathbf{u}(x,\omega)\mathrm{e}^{i\kappa x}\mathrm{d}x \tag{3.2}$$

and likewise for $\mathbf{F}$.

The harmonic system

$$\left[\mathbf{K}_2(-j\kappa)^2 + \mathbf{K}_1(-j\kappa) + \mathbf{K}_0 - \omega^2\mathbf{M}\right]\mathbf{\Phi}(\kappa,\omega) = \mathbf{0} \tag{3.3}$$

contains a linear eigenvalue problem in frequency $\omega(\kappa)$ or a quadratic eigenvalue problem in wavenumber $\kappa(\omega)$, where $\mathbf{\Phi}$ are the eigenvectors corresponding to each eigenvalue. Solving the linear eigenvalue problem by prescribing the wavenumber κ comes at a lower numerical cost, since the necessary linearisation of the quadratic eigenvalue problem leads to double the number of solutions and quadrupling of matrix sizes.

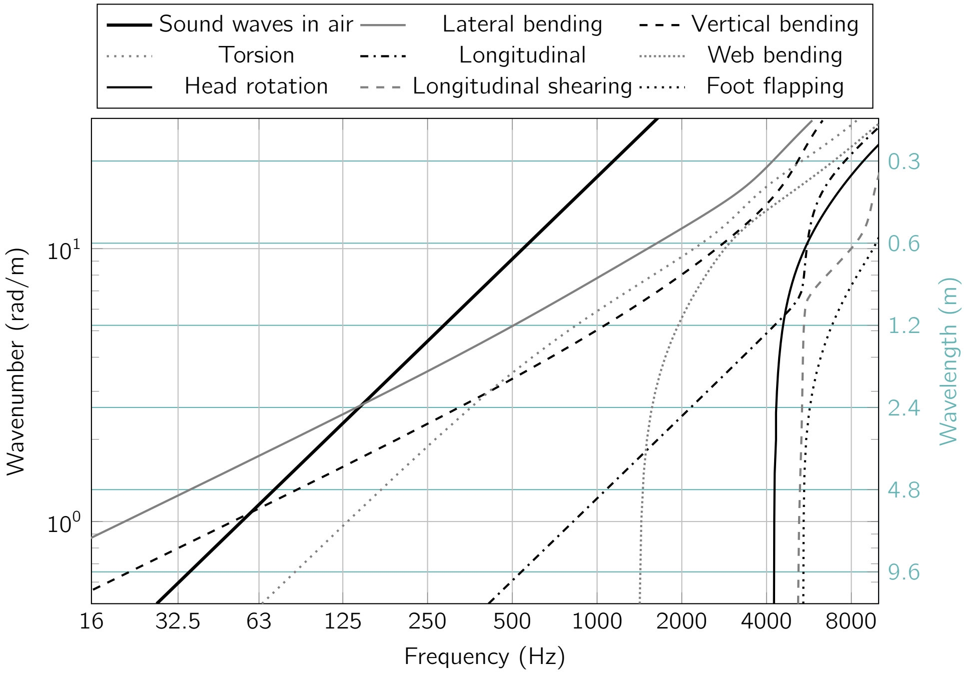

Figure 3.4: Dispersion relation of the waves in a free UIC60 rail. The corresponding wavelengths are indicated on the right.

Solving the linear eigenvalue problem allows studying the dispersion relation by calculating the eigenfrequencies and corresponding cross-sectional deflection at each wavenumber. Examples of different cross-sectional deflections are shown in Figure 3.3, where the arrows indicate the direction and relative magnitude of the motion. The shapes shown here correspond to wavenumber 1 rad/m; shapes at higher wavenumbers are not as distinct. This is in part due to that dispersion curves of related wave types do not cross, but instead an effect similar to modal veering occurs [148, 160]. Exceptions are wave types with uncoupled motions; for example the longitudinal wave is uncoupled from waves with only cross-sectional deflection. Figure 3.4 presents the relationship between the frequency and wavenumber for each wave type, even including the sound waves in air for later reference. Further, the corresponding wavelength $\lambda = 2\pi/\kappa = c_p/f$ is shown, where c_p is the phase speed of each wave. The interaction of these waves with a support is for example observed at the pinned-pinned resonance, which occurs where the bending wavelength fits in between two sleeper bays, or just above 1000 Hz for a 0.6 m sleeper spacing.

The phase speed of each wave is shown in Figure 3.5. For this free rail, lateral and vertical bending wave, the torsional wave and the longitudinal wave exist as rigid body motion at 0 Hz. Some waves 'cut in' at higher frequencies, which means that they do not exist below a certain frequency and then, at their cut-on frequency, exist with an infinite wavelength

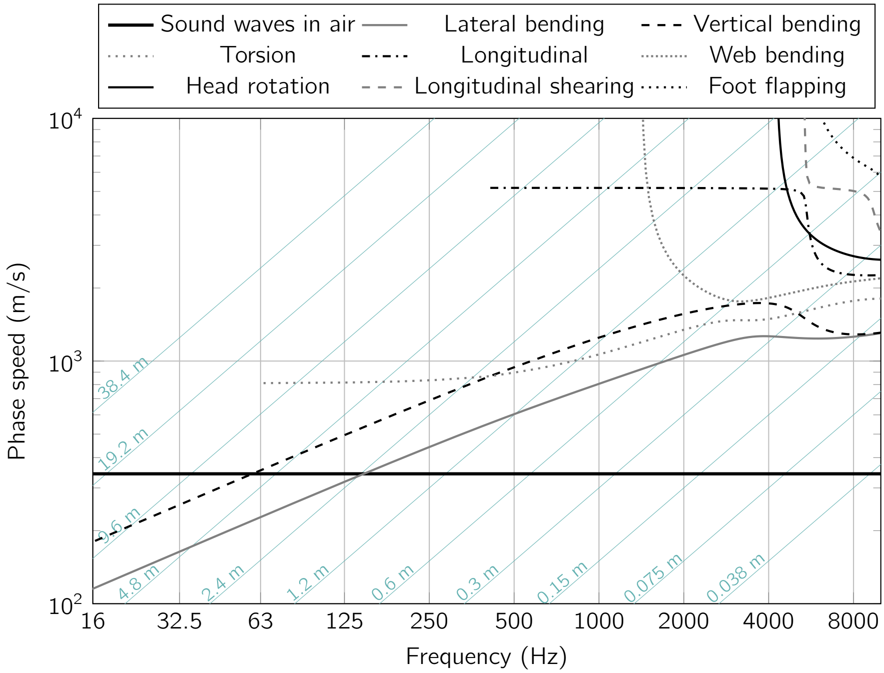

Figure 3.5: Frequency dependent phase speed of the waves in a free UIC60 rail. The diagonals lines indicate corresponding wavelengths.

and phase speed[5]. The point where the speed of sound in air is equal to the phase speed of the waves in the structure is called the critical frequency, at which sound radiation is very efficient. Only the lateral and vertical bending wave cross this point, while the phase speed of the other waves is always larger.

Often, the quadratic eigenvalue problem of (3.3) needs to be solved, since the frequency ω is assumed to be real and its range is known. Furthermore, real wavenumbers correspond to undamped waves [140], which are unphysical. Therefore, in the following, a frequency ω is prescribed and the quadratic eigenvalue problem is solved, generating complex conjugate pairs of eigenvalues corresponding to the wavenumbers κ_i. These represent propagating, decaying waves. The corresponding left and right eigenvectors $\mathbf{\Phi}_{iL}$ and $\mathbf{\Phi}_{iR}$ are obtained that describe the cross-sectional motion at each wavenumber κ_i.

The structural response to an external force $\mathbf{F}(\kappa,\omega) = \mathbf{F}_0(\kappa,\omega)$ in (3.1) can be computed for a grid of combinations of κ and ω. An inverse Fourier transform can recover the response in the spatial domain,

$$\mathbf{u}(x,\omega) = \frac{1}{2\pi}\int_{-\infty}^{\infty} \mathbf{u}(\kappa,\omega)\mathrm{e}^{-i\kappa x}\mathrm{d}\kappa \ . \tag{3.4}$$

However, the waves in the unsupported rail are highly undamped, which means they are

[5] No energy or information is transported, so this does not violate special relativity [161].

decaying slowly in spatial domain. In the wavenumber domain, these waves create narrow peaks that require a high wavenumber resolution.

Instead of the integral expression (3.4), a contour integral can be used [162, 42]. For $x >= 0$, the sum of residues of the poles in the lower half plane solves the integral expression,

$$\mathbf{u}(x,\omega) = \sum_i A_i \mathbf{\Phi}_{iR} \mathrm{e}^{-j\kappa_i x} \text{ for } x \geq 0 \tag{3.5}$$

with the scaling factor

$$A_i = \frac{j\mathbf{\Phi}_{nL}\mathbf{F}_0(\kappa,\omega)}{\mathbf{\Phi}_{nL}\mathbf{D}(\kappa_i)\mathbf{\Phi}_{iR}} \tag{3.6}$$

and

$$\mathbf{D}(\kappa_i) = -2\kappa_i \mathbf{K}_2 - j\mathbf{K}_1. \tag{3.7}$$

In the wavenumber domain, the forced response of the structure can be calculated as a superposition of the individual waves,

$$\mathbf{u}(\kappa,\omega) = \sum_i A_i \mathbf{\Phi}_{iR} \left(\frac{-1}{Im(\kappa_i) - j(\kappa + Re(\kappa_i))} + \frac{-1}{Im(\kappa_i) + j(\kappa - Re(\kappa_i))} \right) \tag{3.8}$$

with where the force vector $\mathbf{F}_0(\kappa,\omega)$ contains the nodal excitation forces over the length of the rail expressed in the wavenumber domain. $Re(\kappa_n)$ and $Im(\kappa_n)$ correspond to the real and imaginary parts of κ_n. An added benefit of calculating the forced response by (3.5) and (3.8) instead of using the direct solution (3.1) is that the main computational load lies in solving the quadratic eigenvalue problem. Once solved, input and transfer receptances of the structure can be generated at comparatively low cost, which is especially relevant in the context of the discrete support in the following section.

3.1.2 Coupling between the rail and its support

The rail can be modelled to be coupled, either discretely or continuously, to different support layers. The setups relevant to this thesis are presented in Figure 3.6. Continuous elastic elements (included in setup c to g) are conveniently realised by including them in the WFE formulation. Discrete supports (included in setup a to d) are realised by adopting an approach developed by Maria Heckl [88]. It makes use of the superposition principle in linear systems, and was also used by Thompson [23] in combination with an analytical beam model for the rail and Zhang et al. [99] with a WFE-based rail model. The idea is to model the effect of the rail supports in terms of their reaction forces. In this way, a continuous and infinite structure, such as the WFE-based rail used here, can be coupled to a finite number of rail supports. In the following, the WFE method is used to calculate the transfer receptances necessary to describe both the dynamic response of the rail and a continuous support. At each rail seat, the rail can be coupled to the support in multiple nodes, for example, nodes 4 to 8 in Figure 3.2.

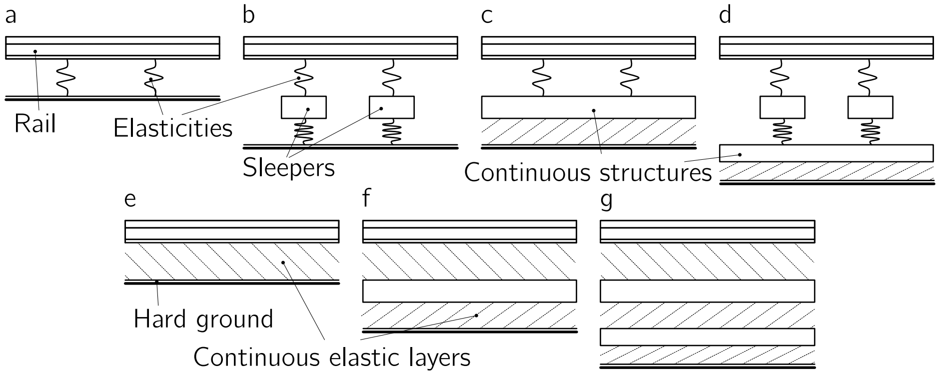

Figure 3.6: Rail support configurations a to g. The shaded areas represent continuous supports.

Given the vector of reaction forces in the spatial domain $\mathbf{F}(x, \omega)$, their effect on the rail can be expressed as a wavenumber spectrum at the origin x_0,

$$\mathbf{F}_0(k, \omega) = \sum_{i=1}^{N} \mathbf{F}_i(\omega) \mathrm{e}^{jkx_i} \tag{3.9}$$

which can then be introduced in (3.5) or (3.8) to calculate the surface displacements of the WFE model. Normalising these surface displacements with the excitation force produces dynamic transfer functions H_d.

Figure 3.6 shows abstractions of existing tracks into basic mechanical components. The methods to calculate reaction forces for the four discrete rail support configurations shown in Figure 3.6 a to d are introduced in the following four subsections. The configuration a represents a rail on a discrete support that is placed on a hard ground. Configuration b includes the sleeper as a rigid mass and the ballast as an additional elasticity below the sleeper. In configuration c, a continuous foundation is introduced under the rail pads. Finally, configuration d includes an additional rigid, elastically supported mass between the rail and the continuous foundation. Configurations e, f, and g symbolise modelling approaches for identical track types with continuous rail supports. The tracks considered in this work are reduced to one of these modelling approaches. The other three, due to their continuous structures, can be modelled in the WFE method directly.

Configuration a: rail on discrete springs

Figure 3.7 (left) shows the forces F, displacements u and receptances α corresponding to two rail seats i and l. The motion of the rail is a superposition of the displacement response of the free rail to an excitation force F_e and the response to the reaction forces

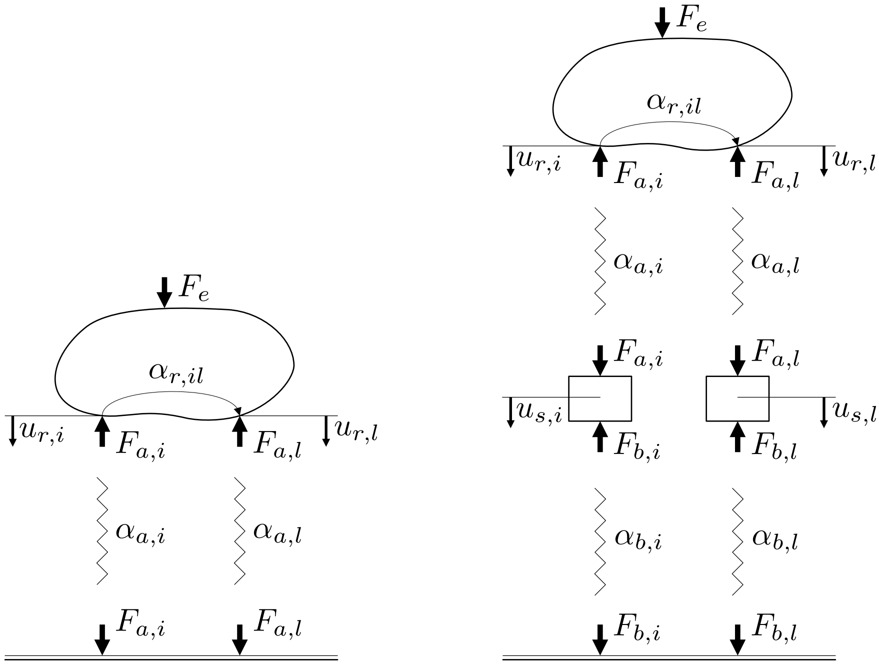

Figure 3.7: Discrete coupling in configuration a (left) and b (right).

in the rail seats $F_{a,l}$,

$$u_{r,i} = \alpha_{r,ie} F_e - \sum_{l=1}^{N} \alpha_{r,il} F_{a,l} \tag{3.10}$$

with the transfer receptance $\alpha_{r,ie}$ between the excitation point e and the position i, the reaction force $F_{a,l}$ on the rail seat l and the corresponding receptance in the free rail $\alpha_{r,il}$. The displacement $u_{r,i}$ is also the receptance of the rail seat $\alpha_{a,l}$ multiplied with the reaction force on the rail seat,

$$u_{r,i} = \alpha_{a,i} F_{a,i} \ . \tag{3.11}$$

These two equations can be formulated for each of the N connection points and arranged in matrix form,

$$\mathbf{u}_r = \boldsymbol{\alpha}_{r,e} F_e - \boldsymbol{\alpha}_r \mathbf{F}_a \tag{3.12}$$

and

$$\mathbf{u}_r = \boldsymbol{\alpha}_a \mathbf{F}_a \tag{3.13}$$

where $\boldsymbol{\alpha}_a$ is a diagonal matrix, since the supports are uncoupled. When modelling elasticity as a linear elastic spring with stiffness k, $\boldsymbol{\alpha}_a = \mathbf{I}k$ where $\mathbf{I}$ is the identity matrix. Note that this approach allows for prescribing individual frequency-dependent stiffnesses at each connection point and that the connection points do not need to be regularly spaced. Inserting (3.13) into (3.12) produces a system of equations,

$$(\boldsymbol{\alpha}_a + \boldsymbol{\alpha}_r)\,\mathbf{F}_a = \boldsymbol{\alpha}_{r,e} F_e \tag{3.14}$$

with the vector of unknown reaction forces $\mathbf{F}_a$. The system of equations is then solved for $\mathbf{F}_a$.

Configuration b: rail on sleepers and ballast

Configuration b introduces the sleepers as rigid masses, each resting on a simple elastic spring that represents the ballast. The sleepers are assumed to vibrate independently of each other. Figure 3.7 (right) shows the relevant quantities, again for two of the N discrete coupling locations. The general approach is identical to the above, starting with (3.10). However, here the reaction forces are a function of the relative displacement between the sleeper and the rail,

$$u_{r,i} - u_{s,i} = \alpha_{a,i} F_{a,i} \tag{3.15}$$

and the displacement of the sleeper is a function of $F_{a,i}$ and the combined receptance α_{c_i} of the sleeper mass and the ballast elasticity,

$$u_{s,i} = \alpha_{c,i} F_{a,i} = \frac{F_{a,i}}{k_{b,i} - m_i \omega^2} \tag{3.16}$$

with the stiffness of the ballast $k_{b,i} = \alpha_{b,i}^{-1}$ and the mass of the sleeper m_i.

Generating one equation for each connection point, these can be written in matrix form,

$$\mathbf{u}_r - \mathbf{u}_s = \boldsymbol{\alpha}_a \mathbf{F}_a \tag{3.17}$$

$$\mathbf{u}_s = \boldsymbol{\alpha}_c \mathbf{F}_a \tag{3.18}$$

which can then be inserted into (3.12), eliminating the unknown displacements. The final system of equations

$$(\boldsymbol{\alpha}_a + \boldsymbol{\alpha}_r + \boldsymbol{\alpha}_c)\,\mathbf{F}_a = \boldsymbol{\alpha}_{r,e} F_e \tag{3.19}$$

is then solved for the unknown reaction forces $\mathbf{F}_a$. The displacements of the sleepers and the reaction forces $\mathbf{F}_b$ are found in a second step by (3.18) and (3.17).

Configuration c: rail on a continuous elastic foundation

The introduction of a continuous waveguide instead of independent sleepers can be achieved by following the approach in configuration b, but altering the receptance α_c so that cross-coupling between different connection points is taken into account. The response at a connection point on the foundation surface is a consequence of suspension forces,

$$u_{f,i} = \sum_{l=1}^{N} \alpha_{f,il} F_{a,l} \ . \tag{3.20}$$

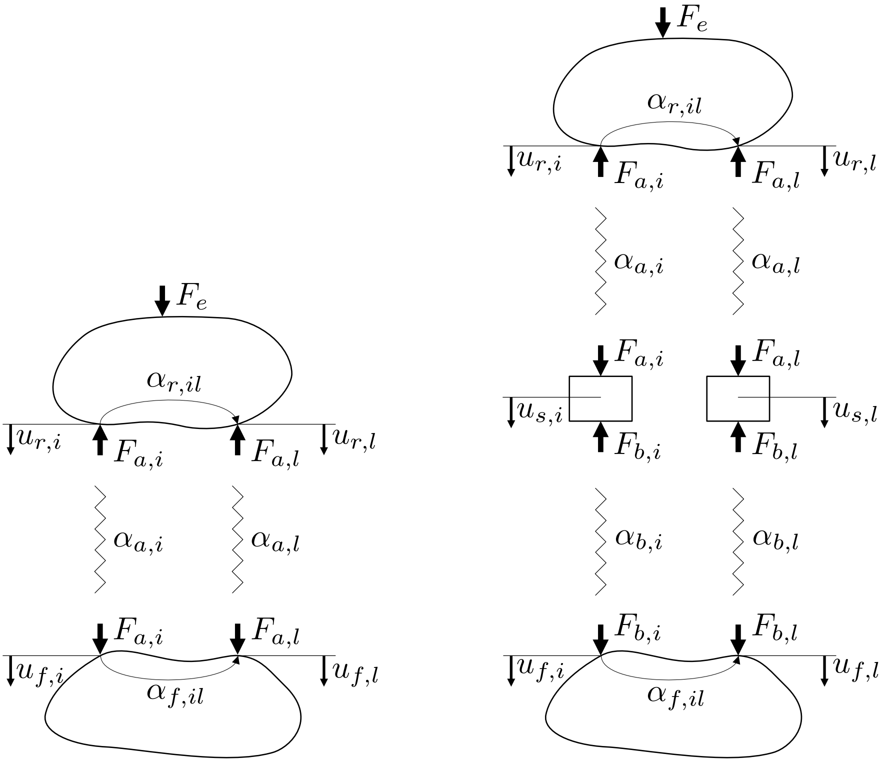

Figure 3.8: Discrete coupling in configuration c (left) and d (right).

In this case, the transfer functions $\alpha_{f,il}$ are calculated using a WFE model, which can include several layers of different materials and appropriate boundary conditions. The final system of equations, following the convention introduced in Figure 3.8, is

$$(\boldsymbol{\alpha}_a + \boldsymbol{\alpha}_r + \boldsymbol{\alpha}_f)\,\mathbf{F}_a = \boldsymbol{\alpha}_{r,e} F_e \tag{3.21}$$

where the matrix $\boldsymbol{\alpha}_f$ is possibly fully populated.

Configuration d: rail on an elastically supported sleeper on a continuous elastic foundation

The last configuration d introduces an elastically supported sleeper on top of the continuous foundation surface. Figure 3.8 introduces the relevant quantities. Following the same approach as above, the displacement of the rail is given by (3.10). The displacement u_f on the foundation is given by (3.20), but the acting force is now $F_{b,l}$,

$$u_{f,i} = \sum_{l=1}^{N} \alpha_{f,il} F_{b,l} \ . \tag{3.22}$$

The force equilibrium on the mass m_i reads $m_i \ddot{u}_{s,i} = F_{a,i} - F_{b,i}$, where $\ddot{u}_{s,i}$ describes the acceleration of the mass. Its displacement is, assuming harmonic motion at frequency ω,

$$u_{s,i} = \frac{F_{a,i} - F_{b,i}}{-\omega^2 m} = \alpha_{s,i}(F_{a,i} - F_{b,i}), \text{ with } \alpha_{s,i} = \frac{1}{-\omega^2 m_i} \tag{3.23}$$

with the forces $F_{b,l}$ acting below the mass.

The relative motion between the rail and the mass, and the mass and the foundation can be expressed by subtracting (3.23) from (3.10) and (3.22) from (3.23),

$$u_{r,i} - u_{s,i} = -\sum_{l=1}^{N} \alpha_{r,il} F_{a,l} - \alpha_{s,i}(F_{a,i} - F_{b,i}) + \alpha_{r,ie} F_e \tag{3.24}$$

$$u_{s,i} - u_{f,i} = -\sum_{l=1}^{N} \alpha_{f,il} F_{b,l} + \alpha_{s,i}(F_{a,i} - F_{b,i}) \; . \tag{3.25}$$

The differences are also functions of the forces and receptances at the respective coupling positions,

$$u_{r,i} - u_{s,i} = \alpha_{a,i} F_{a,i} \tag{3.26}$$

$$u_{s,i} - u_{f,i} = \alpha_{b,i} F_{b,i} \tag{3.27}$$

Substituting (3.26) and (3.27) into (3.24) and (3.25) forms two equations with only the unknown forces $F_{a,l}$ and $F_{b,l}$. As each connection introduces two equations and two unknowns, the problem can be formulated as a system of $2N$ equations. Receptances α_r and α_f can be assembled into symmetric matrices of size N^2. Since the mass and the springs only react locally, that is, $\alpha_{s,il} = 0$ for $i \neq l$, assembling them into matrices of the same shape produces diagonal matrices. The assembled system of equations can be written as

$$\begin{bmatrix} \boldsymbol{\alpha}_r + \boldsymbol{\alpha}_a + \boldsymbol{\alpha}_s & -\boldsymbol{\alpha}_s \\ -\boldsymbol{\alpha}_s & \boldsymbol{\alpha}_f + \boldsymbol{\alpha}_b + \boldsymbol{\alpha}_s \end{bmatrix} \begin{bmatrix} \mathbf{F_a} \\ \mathbf{F_b} \end{bmatrix} = \begin{bmatrix} \boldsymbol{\alpha}_{r,e} F_e \\ \mathbf{0} \end{bmatrix} \tag{3.28}$$

and solved for the unknown vector $[\mathbf{F_a} \mathbf{F_b}]^T$.

3.2 Radiation from track vibration

This section first briefly introduces the Wavenumber domain Boundary Element (WBE) method and then describes two ways to increasing the numerical efficiency of this method under certain conditions.

3.2.1 The Wavenumber domain Boundary Element method

Comparable to the WFE method, the Wavenumber domain Boundary Element (WBE) method makes use of the assumption of a constant geometry along one dimension. In a

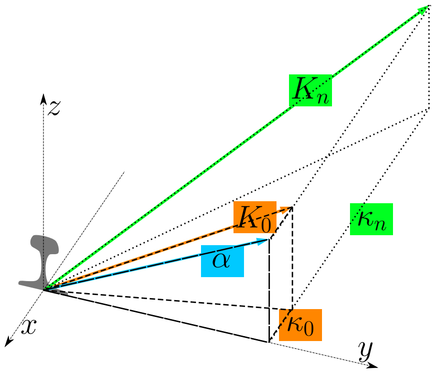

Figure 3.9: Relation between K, κ, and α, corresponding to the wavenumbers in air, along the track, and in the (y,z)-plane, respectively.

similar way, the 3D description of the wave field is reduced to 2D descriptions at different wavenumbers along this dimension. This section presents a brief summary of the method; see [42] for further details.

Figure 3.9 shows the cross section of a rail located in the (y,z)-plane. The geometric relation between two wavenumbers in the air $K = \omega/c$, their projections in the (y,z)-plane and their components in the x direction are presented in Figure 3.9. The variable c describes the speed of sound waves in air. It follows that

$$K^2 = \left(\frac{2\pi f}{c}\right)^2 = \kappa^2 + \alpha^2 \tag{3.29}$$

and $\alpha = \sqrt{K^2 - \kappa^2}$. Each combination of frequency (and therefore K) and wavenumber κ leads to one 2D BE problem with the wavenumber α in the plane to be solved.

The two-dimensional Helmholtz integral equation for an unbounded exterior problem is

$$C(\mathbf{x})\, p(\mathbf{x}) = -\int_\Gamma \left(j\omega\rho v_n \Psi + p\frac{\partial \Psi}{\partial n}\right) \mathrm{d}\Gamma \tag{3.30}$$

in which the integral is evaluated over the boundary Γ, with the density in air ρ, the normal velocity of the surface v_n, the pressure of the surface p and the angular frequency $\omega = 2\pi f$. The variable Ψ represents the fundamental solution to the 2D Helmholtz equation at the point $\mathbf{x}$, with

$$\Psi = -\frac{1}{4}\mathrm{H}_0^{(2)}(\alpha r) \tag{3.31}$$

and its derivative in the surface normal direction n,

$$\frac{\partial \Psi}{\partial n} = -\frac{j\alpha}{4}\mathrm{H}_1^{(2)}(\alpha r)\frac{\partial r}{\partial n} \tag{3.32}$$

where $\mathrm{H}_0^{(2)}$ and $\mathrm{H}_1^{(2)}$ are Hankel functions of the second kind and orders zero and one, respectively. The coefficient $C(\mathbf{x})$ is equal to 1 for $\mathbf{x}$ in the acoustic domain and 1/2 on a smooth boundary. The integral equation is solved on an element-by-element basis by discretization and collocation. Detailed derivation and implementation strategies are presented, for example, by Wu [163].

The two terms in the Helmholtz integral equation, evaluated on an element-by-element basis, eventually form two matrices **H** and **G** with one column per element and one row per collocation point. These form the global system of equations,

$$\mathbf{Cp} + \mathbf{Hp} = \mathbf{Gv}_n \tag{3.33}$$

which is sorted according to the known and unknown boundary conditions and solved using a least-square solver if CHIEF points are present. CHIEF points can be used to reduce resonances outside the acoustic domain [163]. The vectors **p** and **v** collect the pressures and normal velocities in each element.

3.2.2 Methods to increase the numerical efficiency

Especially at high frequencies and for large geometries, the WBE approach is numerically superior to a 3D BE approach due to the significantly lower number of degrees of freedom. However, a consequence of the required discrete Fourier domain representation is that the sound field consists of periodically repeating sections, of which only one section is physically meaningful. The resolution and the number of required wavenumbers increase with the desired length and spatial discretization of this section. When a high spatial and temporal resolution of the predicted sound field is sought, the number of required 2D solutions becomes unfeasibly large. This section investigates methods to further increase the numerical efficiency by using the geometric relation described above and then precalculating the acoustic transfer functions. These methods were newly developed as part of the thesis, however, a method taking advantage of the same physical relationship between wavenumbers as presented in the following has been presented by Li et al. [137] for low-frequency sound radiation from bridge modes.

3D sound field from 2D calculation

For each combination of κ and the wavenumber in the air K there is exactly one α in the 2D plane. However, a given α can be the result of infinitely many combinations of κ and K. This relationship is used here to establish a method in which only one reference frequency spectrum needs to be calculated and solutions at other wavenumbers can be interpolated from this reference spectrum. Two criteria need to be fulfilled to allow replacing one 2D BE solution with a solution from a reference spectrum: the phase and the magnitude relationship between all BE elements need to be identical.

Figure 3.9 shows two combinations of κ and K (κ_0, K_0 and κ_n, K_n) which share the same α. This is the case if

$$K_0^2 - \kappa_0^2 = K_n^2 - \kappa_n^2 \tag{3.34}$$

or, using (3.29) and rearranging for f_0,

$$f_0 = \sqrt{f_n^2 - \frac{\left(\kappa_n^2 - \kappa_0^2\right) c^2}{\left(2\pi\right)^2}}. \tag{3.35}$$

Figure 3.10 visualises the relationship between f_n and f_0 for whole wavenumbers from 0 rad/m to 10 rad/m in the frequency range 0 Hz to 1000 Hz.

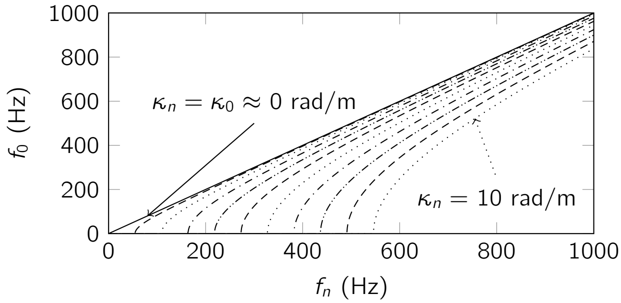

Figure 3.10: Mapping between f_n and f_0 for selected whole wavenumbers k_n 0 rad/m to 10 rad/m.

A reference solution is calculated by evaluating (3.33) for a dense frequency spectrum and a small wavenumber κ_0. For a higher wavenumber κ_n, (3.35) maps any frequency f_n to a frequency f_0 in the reference spectrum with an identical α. An identical α means that the phase relations in the 2D BE problem are identical.

Reusing the 2D BE solution at a different frequency also involves a magnitude scaling in the two-dimensional Helmholtz integral equation (3.30), since the first term of the integral contains the factor $j\omega$ and the normal velocity v_n. A scaling of the boundary element equation (3.33) is proposed;

$$\mathbf{Cp} + \mathbf{Hp} = \mathbf{G}^* \mathbf{v}_n^* = \frac{\mathbf{G}}{j\omega} \mathbf{v}_n j\omega \tag{3.36}$$

such that the frequency dependency is included in the normal velocity instead.

Here, the normal velocity serves as the input to the BE problem, so the scaling of $\mathbf{v}_n^*$ can be introduced there. Any frequency-independent boundary condition can be used with this scaling; however, for boundary conditions other than the Neumann boundary condition (prescribing the velocity), the elements in the result vector corresponding to a normal velocity need to be scaled accordingly.

An interpolation is necessary when the original frequency spectrum does not contain f_0. A standard implementation of complex quadratic interpolation is used, interpolating the real and imaginary parts separately (see, for example, `interp1` in MATLAB or `interp` in Numpy). To avoid extrapolation, any query point at which to evaluate the interpolation needs to lie between the limits of the original spectrum. This requirement is fulfilled by the method itself: From (3.35) follows that for $\kappa_n > \kappa_0$, the frequency f_0 is strictly lower than the frequency f_n with the same α in the 2D plane. Therefore, a frequency spectrum at any higher wavenumber maps to smaller frequency lines, and thus the upper bound is fulfilled. The lower bound is limited by the physical properties of sound radiation. Figure 3.10 shows that for increasing wavenumbers, increasing frequencies get mapped to 0 Hz in the f_0 spectrum, and there are no solutions for smaller f_n. Mathematically, this is because the radicant in (3.35) is negative for $K_n^2 < (\kappa_n^2 - \kappa_0^2)$. Physically, this means that the wavenumber in the air is smaller than the wavenumber along the track, so no projection on the 2D plane is possible and only radiation into the near field occurs. Since no sound power is radiated, these wavenumbers are excluded from further calculations.

In summary, this first approach makes it possible to solve the 2D BE problem for only one wavenumber at every frequency in a dense frequency spectrum, and then generates solutions at higher wavenumbers by interpolation and frequency- dependent magnitude scaling of the result.

Pre-calculation of acoustic transfer functions

If there is no backcoupling between air and structure (the radiation impedance in air has a negligible effect on structural vibration), the surface normal velocity can be calculated independently of the BE problem. The decoupled calculation also allows for precalculating the BE problem for a unit excitation and scaling the results with the normal velocity of the surface, which is presented below. This is beneficial when calculating multiple excitation cases with varying surface vibrations that share the same acoustic geometry. The following discussion is limited to changing the Neumann boundary condition.

Acoustic transfer functions can be precalculated taking advantage of the integral nature of the BE formulation. The linear equation system (3.36) becomes

$$\mathbf{A}\mathbf{p} = \mathbf{G}^*\mathbf{v}_n^* \tag{3.37}$$

when combining the $\mathbf{C}$ and $\mathbf{H}$ matrices into the $\mathbf{A}$ matrix. In this discretised problem formulation, the sound pressure at any receiver position is the sum of the contributions of each source element. Here, these contributions are evaluated separately. Three boundary elements are outlined in Figure 3.11a with respective normal velocities v_n. Acoustic transfer functions H_a are evaluated for each element by setting the surface normal velocity to 1 m/s and 0 m/s otherwise in $\mathbf{v}_n^*$. Predicting the total pressure produced by the surface velocities of the element v_n is achieved by scaling and adding these transfer functions

$$p = \sum_i v_{n,i} H_{a,i} \tag{3.38}$$

where p and $H_{a,i}$ can be vectors if the pressure is evaluated at multiple receiver points.

A complete solution requires solving the large, potentially overdetermined, and dense matrix system once for every source element, which is a significant initial computational effort. Especially when investigating radiation from a railway track, the total number of

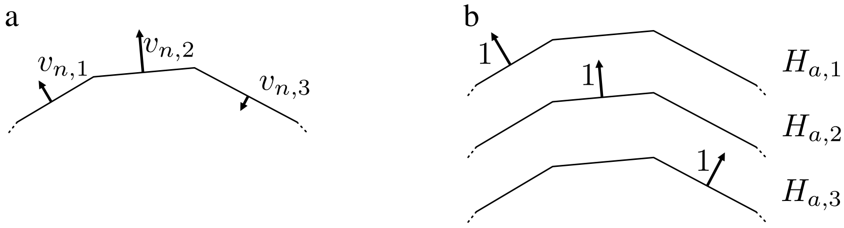

Figure 3.11: Visualisation of the precalculation of the acoustic transfer functions H_a.

elements can be large when including a train or noise barriers in the geometry. On the other hand, often only a small part of the geometry is relevant for the radiation in the calculation, such as the rail and parts of the track surface. These are described by just a fraction of the total number of boundary nodes, so the precalculation can be limited to these areas. Examples for which acoustic transfer functions have been evaluated are described in Section 5.5.

3.3 Adapted inverse Fourier transforms for calculating the spatial sound pressure field

The previous sections describe efficient ways to calculate the frequency-wavenumber spectrum of the vibration field in the structures and the complex sound pressure in a point. Figure 3.12 shows an example of the vertical surface velocity of the rail head in the frequency-wavenumber domain for a UIC60 rail model based on the WFE method (see 3.2). The rail is discretely coupled to 119 regularly spaced sleepers resting on a ballast layer. The support is modelled as an analytical spring-mass-spring system, and the rail is excited with a harmonic unit force centrally on the rail head, mid-span. The distance between two sleepers is 0.6 m. The support parameters and a more extensive analysis of the produced sound field is given in Section 5.6.

The waves in the rail appear as narrow peaks in the wavenumber spectrum. By choosing wavenumbers close to these waves and using an adapted Fourier integral, the numerical accuracy and efficiency can be increased, for both the radiation from rail and sleepers, as shown below.

3.3.1 The sound field around a vibrating rail

The pressure in a point in space needs can be retrieved from the wavenumber spectrum by an inverse Fourier transform,

$$p(x, \omega) = \frac{1}{2\pi} \int_{-\infty}^{\infty} p(\kappa, \omega) \mathrm{e}^{-j\kappa x} \mathrm{d}\kappa \tag{3.39}$$

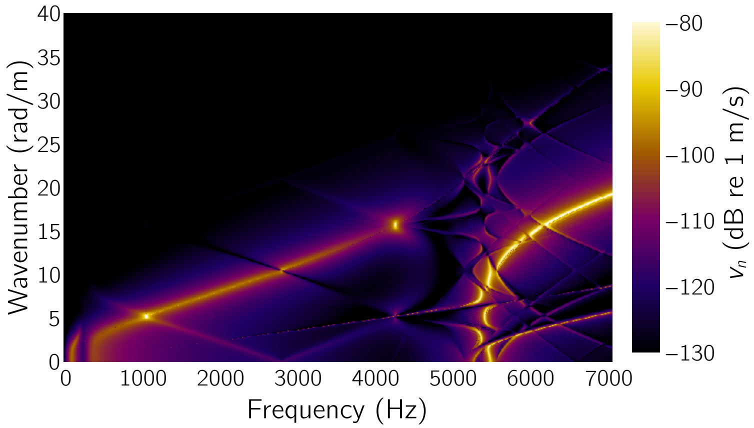

Figure 3.12: Normal velocity magnitude on top of the rail head over frequency and wavenumber for a discretely coupled rail.

which could be solved numerically via the Fast Fourier Transform (FFT). Yet, a semi-analytical approach is used here to solve this integral, for three reasons: First, the waves in the rail typically produce sharp peaks in the wavenumber spectrum due to the low material damping of the rail. Creating an irregular wavenumber spectrum where the wavenumbers are more closely spaced close to these peaks allows for a coarser spacing otherwise, resulting in a faster calculation and a more accurate result [42]. Second, the Fourier transform algorithm inherently assumes a periodic signal. The signal period is proportional to the inverse of the spacing of the bins in the Fourier domain. Using an inverse Fourier transform to calculate the spatial response produces mirror sources at each period length, which, due to the high wave speed in the rail, can interfere with the desired result. Solving the integral semi-analytically and spacing the sampling points closely to the peaks avoids these mirror sources. Third, the total radiated sound power is typically calculated as a double integral of the intensity on a set of receiver points that surround the geometry in the 2D plane and on the total length of the structure [42]. An integral of the squared pressure over a regularly discretised wavenumber domain corresponds to only including the finite section of one signal period in the integral, so the total sound power is possibly underestimated.

When solving (3.39) using a standard Riemann sum, the integrand $p(\kappa,\omega)\mathrm{e}^{-j\kappa x}$ is assumed to be piecewise constant in the Ξ intervals,

$$p(x,\omega) = \frac{1}{2\pi}\sum_{\xi=1}^{\Xi}\left(p_\xi(\kappa,\omega)\mathrm{e}^{-j\kappa_\xi x}\Delta\kappa_\xi\right) \tag{3.40}$$

where $p_\xi(\kappa,\omega)$ is the value of $p(\kappa,\omega)$ in the centre of the interval ξ and $\Delta\kappa_\xi$ is the width of this interval. This formulation converges for small $\Delta\kappa_\xi$, however, the term $\mathrm{e}^{-j\kappa_\xi x}$ is highly oscillatory for large x, and with the irregular spacing of integration points, this approximation produces weak estimates of the original integral. An alternative solution is proposed in which only the pressure $p(\kappa, \omega)$ is assumed piecewise constant and thus excluded from the integral;

$$p(x,\omega) = \frac{1}{2\pi} \sum_{\xi=1}^{\Xi} \left(p_\xi(\kappa,\omega) \int_{\kappa_\xi - \Delta\kappa_\xi/2}^{\kappa_\xi + \Delta\kappa_\xi/2} \mathrm{e}^{-j\kappa x} \mathrm{d}\kappa \right) \tag{3.41}$$

so the oscillatory term can be solved analytically,

$$p(x,\omega) = \frac{1}{2\pi} \sum_{\xi=1}^{\Xi} \left(p_\xi(\kappa,\omega) \frac{2}{x} \, \mathrm{e}^{-j\kappa_\xi x} \sin\left(\frac{\Delta\kappa_\xi}{2} x \right) \right). \tag{3.42}$$

Often, $p(\kappa, \omega)$ is symmetric with respect to κ, corresponding to propagating waves in both directions along the waveguide in both the rail vibration model and the BE model for air radiation ($p_\xi(-\kappa) = p_\xi(\kappa)$). Integration over the negative half of the wavenumber spectrum can thus be included directly as

$$p(x,\omega) = \frac{1}{2\pi} \sum_{\xi=\Xi/2}^{\Xi} \left(p_\xi(\kappa,\omega) \frac{4}{x} \cos(\kappa_\xi x) \sin\left(\frac{\Delta\kappa_\xi}{2} x \right) \right) \tag{3.43}$$

and, for $x = 0$,

$$p(x,\omega) = \frac{1}{2\pi} \sum_{\xi=\Xi/2}^{\Xi} \left(2 p_\xi(\kappa,\omega) \Delta\kappa_\xi \right) \ . \tag{3.44}$$

Equations (3.42) to (3.44) allow an exact solution for the second term in the integrand in each interval. The first term of the integrand, $p_\xi(\kappa, \omega)$, is highly dependent on the velocity of the rail surface. An optimisation of the integration points is carried out in the Appendix A.1. The sound field produced by the discretely supported rail described in the beginning of this Section 3.3 is presented in Section 5.6.2

3.3.2 The sound field produced by a vibrating sleepers

For predicting the radiation from sleepers with the method presented above, their surface velocity is described in the wavenumber domain. For this, the track surface is assumed to be flat, i.e. the sleepers are assumed to be embedded by the surrounding stationary material. The limitation of this assumption is investigated in Appendix A.3. Based on a dynamic model and the force acting on each sleeper as shown in Section 3.1, the surface velocity $v^*_{n,i}(\omega)$ of each sleeper is determined. This surface velocity can vary laterally across the track if the sleeper is flexible. The surface velocities of all sleepers are expressed as a velocity profile for several parallel lines along the track, as presented in Figure 3.13. This section presents a numerically advantageous way to transform these velocity profiles into the wavenumber domain to include the sound radiation from sleepers in the method presented above. The lateral and longitudinal motion of the sleepers is neglected. The normal velocity in between the sleepers is assumed to be zero. One such slice is visualised in Figure 3.14. With a total of N sleepers, where N is odd, the 0^{th} sleeper is centred at

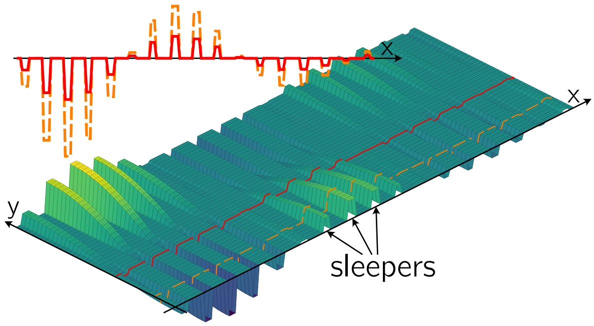

Figure 3.13: Example velocity profile along the length of the track, assuming monoblock sleepers. Each slice along the track produces a different profile, which can be expressed as a wavenumber spectrum.

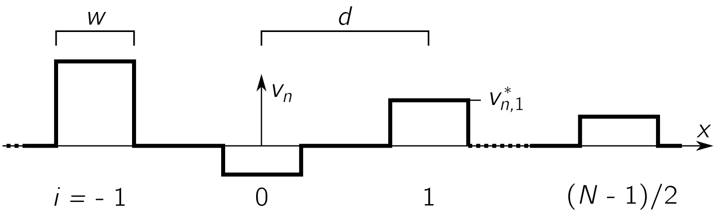

Figure 3.14: Normal velocity slice v_n over the length of the considered track section due to the vertical velocity at each sleeper.

the origin at $x = 0$. In this example, the sleepers are distributed evenly on both sides of the 0^{th} sleeper; however, this is not a requirement of the method.

Assuming a sleeper width w, the spatial velocity distribution (now without $*$) of the i^{th} sleeper is

$$v_{n,i}(x,\omega) = v^*_{n,i}(\omega)\left(\mathrm{H}\left(x - id + \frac{w}{2}\right) - \mathrm{H}\left(x - id - \frac{w}{2}\right)\right) \tag{3.45}$$

with the Heaviside step function H and the sleeper spacing d. This expression can be described as one frequency-independent, normalised, rectangular component,

$$\beta(x) = \mathrm{H}\left(x + \frac{w}{2}\right) - \mathrm{H}\left(x - \frac{w}{2}\right) \tag{3.46}$$

which is then shifted in space by id and scaled with the normal sleeper velocity $v^*_{n,i}(\omega)$, so that

$$v_{n,i}(x,\omega) = v^*_{n,i}(\omega)\beta(x - id). \tag{3.47}$$

The velocity contributions of all sleepers can be added,

$$v_n(x,\omega) = \sum_{i=1}^{N} v_{n,i}(x,\omega) \tag{3.48}$$

to describe the total velocity distribution in space. A sleeper velocity profile evaluated for the track described in the introduction to this section 3.3 is shown in Figure 3.15. For

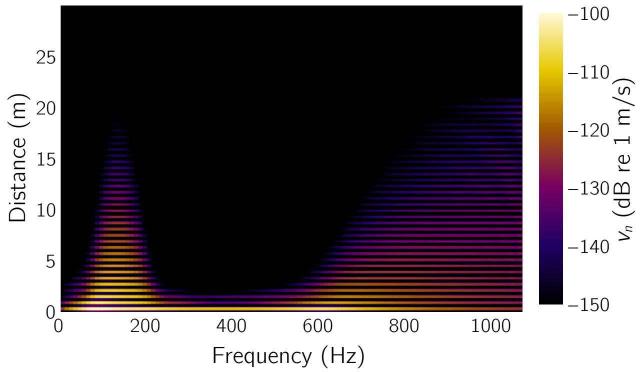

Figure 3.15: Sleeper velocity profile over space and frequency, for a unit force harmonic excitation at $x = 0$ m. Only half the considered track section is shown.

most of the frequency range, only the first one to two sleepers (or two to four, counting both directions) next to the excitation have a significant velocity, especially considering the large dynamic range included in the figure, which is similar to the findings in [129]. This velocity spectrum must be evaluated for each boundary node on the track surface.

To describe this function in the wavenumber domain, it is possible to discretise the function in space and solve the inverse Fourier transform numerically. However, all components in (3.47) (rectangle, shift, and scaling) have simple Fourier domain counterparts. The analytical expression for the velocity spectrum in the wavenumber domain for the i^{th} sleeper is

$$v_{n,i}(k, \omega) = v_{n,i}^*(\omega)\ w\ \mathrm{sinc}(\kappa w)\ \mathrm{e}^{-j\kappa i d} \tag{3.49}$$

with

$$\mathrm{sinc}(\kappa w) = \frac{\sin(\kappa w)}{\kappa w}. \tag{3.50}$$

Due to linearity, the components can be summed

$$v_n(\kappa, \omega) = \sum_{i=1}^{N} v_{n,i}(\kappa, \omega) \tag{3.51}$$

comparable to (3.48) to produce a wavenumber spectrum that incorporates the effect of all sleepers. Interestingly, this means that the sound field produced by all sleepers, for one combination of frequency and wavenumber, can be expressed by one representative sleeper of the same geometrical dimensions, whose vibration magnitude and location in space are given by the amplitude and phase of $v_n(k, \omega)$. Therefore, the computational effort to solve the radiation from the track is independent of the number of sleepers included in the calculation.

Figure 3.16 shows the velocity profile in the wavenumber domain for the track described above. The repeating pattern along the wavenumber domain is a consequence of the regular spacing of the sleepers and is created by the properties of the sinc function. The period length of the pattern corresponds to the sleeper spacing, $\frac{2\pi}{0.6\ \mathrm{m}} \approx 10.5\frac{\mathrm{rad}}{\mathrm{m}}$. Two support resonances are visible as frequency regions with high vertical velocity, the first one corresponding to the rail and sleeper resonance at about 100 Hz and the second one to the vertical cut-on frequency of the rail at about 460 Hz (see also Figure 3.17). Above the second resonance, the sleeper vertical vibration is mainly excited by the vertical bending wave of the rail. The pattern follows the dispersion curve for this wave shown in Figure 3.12. With the spectrum as the input and the approach described above, a sound

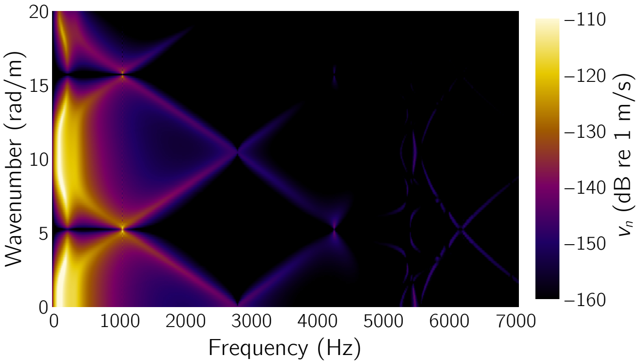

Figure 3.16: Vertical normal velocity profile of the track in the wavenumber-frequency domain.

pressure spectrum can be calculated in the wavenumber-frequency domain. The sound pressure in spatial domain then requires an inverse Fourier transform, yet, comparable to the radiation from the rail, knowledge about the vibration spectrum can increase numerical precision and efficiency.

First, the sound power is only radiated when the wavenumber in the structure is smaller than or equal to the wavenumber in the air. The red diagonal line in Figure 3.17 marks the wavenumber in air. In the frequency range in which the radiation from the sleepers is relevant, the wavenumber in the air is not larger than about 20 rad/m. This truncation of the wavenumber spectrum of the velocity profile at the wavenumber in air means removing the information of the velocity irrelevant to the sound radiation from sleepers. Figure 3.18 shows this truncated velocity profile in space (compare to Figure 3.15 for the original profile). It is visible that, for low frequencies, several sleepers are expected to radiate together. The shape of individual sleepers is not relevant. With increasing frequency, the profile of individual sleepers becomes increasingly defined. This means that the sound pressure along the track is increasingly dependent on the sound radiated by individual sleepers. For this track, individual sleepers are identifiable only from about 400 Hz. Furthermore, it is visible that the decay of the surface velocity is high and that the surface velocity is reduced by 20 dB or more in 6 m distance.

Second, a semi-analytical approach to solving the inverse Fourier transform using the Riemann sum is developed to approximate the semi-analytical solution to the inverse

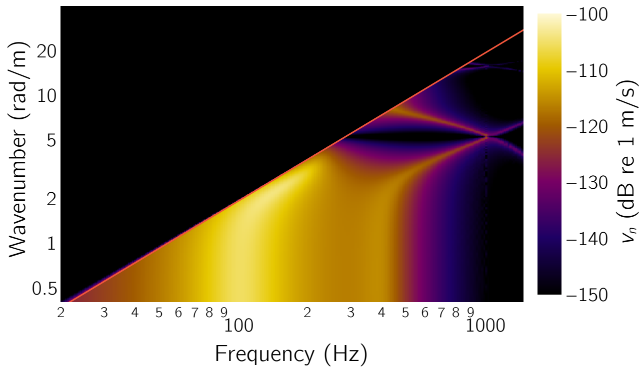

Figure 3.17: Velocity profile in frequency-wavenumber domain, including only wavenumbers relevant for sound radiation. The red line indicates the wavenumber in air. Note the logarithmic frequency axis.

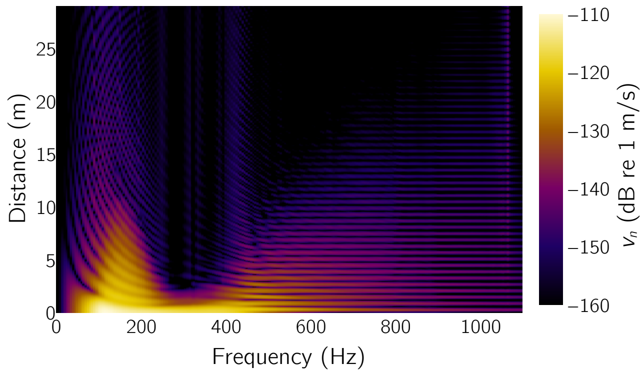

Figure 3.18: Sleeper velocity profile, neglecting wavenumbers that do not contribute to sound radiation.

Fourier transform. The integral could be solved by discretising $v_n(\kappa, \omega)$ to Ξ piecewise constant intervals, transforming the expression into a sum, and solving the exponential term analytically comparable to Section 2.3.2. However, in this case, even $v_{n,i}(\kappa, \omega)$ is oscillatory considering the exponential term in Equation (3.49). The exponentials can be combined by inserting (3.49) into the inverse Fourier transform of $v_n(\kappa, \omega)$,

$$v_n(x, \omega) = \frac{1}{2\pi} \int_{-\infty}^{\infty} \sum_{i=1}^{N} \left(v_{n,i}^*(\omega) \; w \; \mathrm{sinc}(\kappa w) \; \mathrm{e}^{-j\kappa i d} \mathrm{e}^{-j\kappa x} \right) \mathrm{d}\kappa \tag{3.52}$$

and considering that the integral of the sum of a number of functions is the same as the sum of their integrals,

$$v_n(x, \omega) = \frac{w}{2\pi} \sum_{i=1}^{N} v_{n,i}^*(\omega) \; \int_{-\infty}^{\infty} \mathrm{sinc}(\kappa w) \; \mathrm{e}^{-j\kappa(id+x)} \mathrm{d}\kappa \; . \tag{3.53}$$

This can be solved analytically (leading to (3.48)) or as a Riemann sum analogously to (3.43). The oscillation of the sinc function has a rather long, frequency-independent period length of $2\pi w$ and can thus be approximated as being piecewise constant,

$$v_n(x,\omega) = \frac{w}{2\pi} \sum_{i=1}^{N} \left(v_{n,i}^*(\kappa,\omega) \sum_{\xi=\Xi/2}^{\Xi} \mathrm{sinc}_\xi \ \chi_\xi \right) \tag{3.54}$$

with

$$\chi_\xi = \frac{4}{x} \cos(\kappa_\xi(id+x)) \sin\left(\frac{\Delta\kappa_\xi(id+x)}{2}\right) \tag{3.55}$$

and

$$\mathrm{sinc}_\xi = \frac{1}{2} \left(\mathrm{sinc}(\kappa_\xi - \Delta\kappa_\xi/2) + \mathrm{sinc}(\kappa_\xi + \Delta\kappa_\xi/2)\right) \tag{3.56}$$

The sound pressure $p_s(x,\omega)$ produced by one slice along the track is then calculated as

$$p_s(x,\omega) = \frac{w}{2\pi} \sum_{i=1}^{N} \left(v_{n,i,s}^*(\kappa,\omega) \sum_{\xi=\Xi/2}^{\Xi} H_{a,\xi}(\omega) \ \mathrm{sinc}_\xi \chi_\xi(x) \right) \tag{3.57}$$

where $H_{a,\xi}(\omega)$ is the average value of the acoustic transfer function in the wavenumber interval ξ.

Note that the sound pressure radiated by the sleepers is thus linearly proportional to the width of the sleeper. The pressure radiated by the whole track width is a sum over all slices,

$$p(x,\omega) = \sum_s p_s(x,\omega). \tag{3.58}$$

This way of iteratively summing over each wavenumber, sleeper, and lateral position on the track is computationally not cheap; however, it is still small compared to solving a 3D BE problem providing a comparable resolution in frequency and space. Limiting the number of sleepers included further reduces computational cost. An example of the sound field radiated by a series of sleepers connected by a rail is presented in 5.6.3.

In the presented approach, the surface between the sleepers is modelled as acoustically reflective, which lends itself well for, e.g., ballastless tracks with booted sleepers. Including the acoustic absorption of the railway ballast is not straightforward and needs to be considered in a future study.

In summary, this section 3.3 provides efficient approaches to calculate the spatial sound field around a railway track, based on the type of dynamic excitation. Evaluating the pressures $p(x,\omega)$, produced by Equations (3.43) and (3.58), for a unit excitation of the track produces transfer functions H_{ad} which include the dynamic and the acoustic response of the structure. The next section makes use of these transfer functions to calculate the sound during a pass-by.

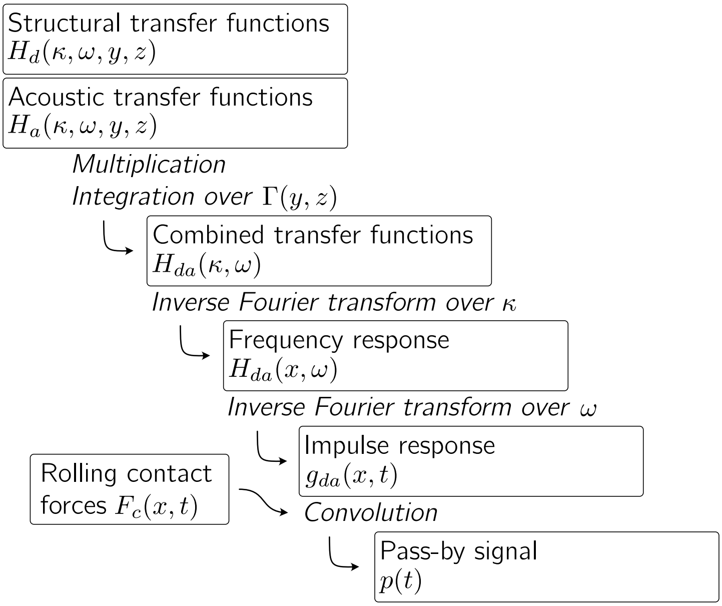

Figure 3.19: Process steps to calculate the pass-by signals given the transfer functions as described in the sections above.

3.4 Sound of a passing force on a rail

Section 3.1 introduced methods to evaluate structural vibrations on different types of tracks in terms of dynamic transfer functions $H_d(\kappa, \omega)$. The following section 3.2 then presented efficient ways to calculate the acoustic transfer functions $H_a(\kappa, \omega)$ independent of the vibration of the track. Finally, Section 3.3 introduced ways to efficiently couple the two, producing transfer functions $H_{da}(\kappa, \omega)$ that can describe the pressure at a trackside point with high resolution in the wavenumber frequency domain.

Given H_{da} and a series of rolling contact forces $F_c(x, t)$, the sound pressure signals during the pass-by of a force can be efficiently calculated, as shown in Figure 3.19. The pressure signals are predicted using moving Green's functions. To obtain the moving Green's functions, the pressure transfer function to a receiver position (x_r, y_r, z_r) is evaluated for a force excitation pulse at K linearly spaced positions on the rail, with spacing $\mathrm{d}x = v\mathrm{d}t = v/f_s$, vehicle speed v and the desired sampling frequency f_s. Impulse responses are collected in the Green's function matrix $\mathbf{g}_{da}(x, t)$. If the support of the rail is continuous, only the absolute distance between the excitation and the receiver is relevant, making it computationally more efficient to excite at the position x_0 and evaluate the acoustic impulse responses at linearly spaced locations along the rail. For a discretely supported track, the excitation position relative to the sleepers is relevant, and so the computational effort is somewhat increased. For such tracks, impulse responses are

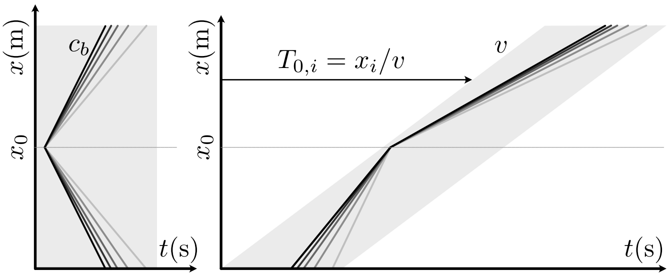

Figure 3.20: Aligning impulse responses to the velocity of a passing force to compute the pass-by pressure signal. Left: Impulse response matrix g_{da}, where diagonal lines symbolise the arrival of wave fronts at x_0 for an excitation at x. Right: Aligning the impulse responses with the location of the moving excitation force in space and time.

generated for eight excitation positions in a sleeper bay and interpolated for positions in between.

Figure 3.20 visualises the principal for computing the pass-by sound pressure given the Green's function matrix $\mathbf{g}_{da}(t, x)$, the vehicle speed v, and the rolling contact force defined in space and time $F_c(x, t) = F_c(t)\delta(x - vt)$. The diagonal curves represent peaks in the calculated impulse responses, which are caused by the arrival of different wave fronts. The slope of these curves in the figure on the left indicates the phase speed c_b of the waves in the rail. At each time step, the rail is excited at a new position. Aligning the Green's function matrix with the corresponding force location results corresponds to a "shearing" of the Green's function matrix as seen in the right figure. The total sound pressure at location x_0 and time step t_n is then calculated as

$$p(t_n) = \sum_{i=0}^{K} \mathbf{g}_{da} \left(i\Delta x, t_n - \frac{i\Delta x}{v} \right) F_c \delta(i\Delta x) \Delta x \tag{3.59}$$

with

$$\mathbf{g}_{da}(x, t \leq 0) \stackrel{\text{def}}{=} 0. \tag{3.60}$$

Notice that this formulation includes the Doppler effect, not due to the relative motion between source and observer (the rail and the receiver are stationary) but instead because of a compression or elongation of the waves in the rail due to the time-dependent excitation.

A different way to obtain pressure signals is to transform the force $F_c(x, t)$ to the wavenumber-frequency domain, multiplying by the transfer functions $H_{da}(\kappa, \omega)$, and use a 2D inverse Fourier transform. However, this approach has two disadvantages: First, the wavenumber-frequency representation of $F_c(x, t)$ is a large square matrix with one row and one column for each time step during the pass-by. Multiplication requires evaluating transfer functions H_{da} with identical wavenumber and frequency resolution. However, impulse responses g_{da} typically decay quickly, in the order ≤ 0.1 s compared to the typical duration of a pass-by. This means that the required transfer function matrix H_{da} would need to be evaluated with unnecessarily high frequency resolution. In the approach followed here, convolution in the time domain allows one to appropriately adjust the lengths of impulse responses. The second disadvantage of this approach is the assumed periodicity in the Fourier transform. The frequency-wavenumber representation of the impulse forces creates excitation forces in periodic distances, which, due to the high wave speed in the rail, can interfere with neighbouring sections if the sections are spatially too close together. However, increasing the spatial distance using this method also increases the total simulation time, giving the waves more time to travel along the rail, again increasing the necessary block size in the spatial domain. The only solution is to increase the size of the block such that the waves in the rail decay sufficiently within one block. The corresponding frequency and wavenumber resolution produce unfeasibly large matrices.

However, this periodicity can be an advantage, for example to predict the waves in tyres and wheels. With waves propagating around the wheel, the periodicity is physically meaningful [164, 45]. This is exploited in the following section.

4 Modelling wheel vibration and radiation

In three sections, this chapter introduces modelling approaches to calculate the structural modes of a railway wheel (4.1), the radiation from the wheel (4.2), and the sound of a passing wheel in the time domain (4.3). Some application results are presented in Sections 5.8, 5.9, and 5.10.

4.1 Vibration modelling of the wheel

The WFE formulation used for track components in the previous section can be adapted to axisymmetric structures. In this case the "long" dimension is around the axis of symmetry and wave propagation is assumed around this central axis. The cross-sectional geometry and material properties are constant in the circumferential direction. The motion in this dimension is then described by a set of propagating waves that meet the periodicity condition $\mathbf{u}(\theta, \omega) = \mathbf{u}(\theta \pm 2\pi, \omega)$, where θ is the circumferential angle introduced in Figure 4.1. The method is common in the context of modelling wheel vibrations and is presented in detail in other publications [140, 141, 142, 157, 45]. This section comprises a short summary of the method.

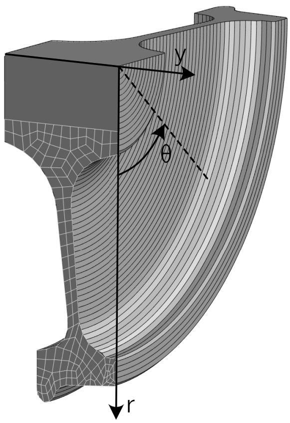

Figure 4.1: The curved waveguide model of the wheel. The cross-section is located in the (y,r)-plane.

The cross-section is discretised into finite elements. The derivation of the system of equations is analogous to the straight waveguide, where the strain vector and the stiffness matrix are adjusted to the axisymmetric formulation (cf. [141]). This produces a system of equations of identical form as (3.1). Periodicity requires an integer number of oscillations around the axis, so only specific wavenumbers κ can occur (opposed to the straight case, where a dense wavenumber spectrum exists). This means it is beneficial to consider the linear eigenvalue problem of (3.3) by prescribing the wavenumber κ and solving for eigenfrequencies ω,

$$\left[\mathbf{K}_2(-j\kappa)^2 + \mathbf{K}_1(-j\kappa) + \mathbf{K}_0 - \omega^2\mathbf{M}\right]\boldsymbol{\Phi}(\kappa,\omega) = \mathbf{0} \tag{4.1}$$

which produces pairs of eigenfrequencies ω_l and cross-sectional mode shapes $\boldsymbol{\Phi}_l$ for each wavenumber κ. The cross-sectional mode shapes propagate in the circumferential direction with the wavenumber κ, such that $\boldsymbol{\Phi}_l(\theta,\omega) = \boldsymbol{\Phi}_l(\omega)\mathrm{e}^{-j\kappa\theta}$. The total velocity field on the wheel $\mathbf{v}(\theta,\omega)$ is obtained by superposition of all modal contributions,

$$\mathbf{v}(\theta,\omega) = \sum_l A_l(\omega)\boldsymbol{\Phi}_l(\theta,\omega) \tag{4.2}$$

where $A_l(\omega)$ are the modal amplitudes and l iterates over all relevant wavenumbers and cross-sectional mode shapes. Often, modes with eigenfrequencies far above the considered frequency range can be neglected. Modal amplitudes are calculated as

$$A_l(\omega) = j\omega b_l(\omega)\mathbf{F}_e(\omega)\boldsymbol{\Phi}_l(\mathbf{x}_0) \tag{4.3}$$

where the excitation force vector $\mathbf{F}_e(\omega) = [F_\theta(\omega),\ F_y(\omega),\ F_r(\omega)]^{\mathrm{T}}$ is considered a point force acting in position $\mathbf{x}_0 = [\theta_0, y_0, r_0]^{\mathrm{T}}$. The term b_l describes the structural response independent of excitation position,

$$b_l(\omega) = \frac{1}{\Lambda_l(\omega_l^2 - \omega^2 + j2\omega\omega_l\zeta_l)} , \tag{4.4}$$

where ω_l are the eigenfrequencies and ω is the angular frequency. The variable ζ_l represents the damping ratio for the mode l. The modal mass Λ_l is calculated using the orthogonality relation

$$\Lambda_l = \boldsymbol{\Phi}_l^{\mathrm{H}}\mathbf{M}\boldsymbol{\Phi}_l . \tag{4.5}$$

If the damping is not considered in (4.1), $\mathbf{K}_0$, $\mathbf{K}_1$, $\mathbf{K}_2$, and $\mathbf{M}$ are real and symmetric or skew-symmetric. This means that waves travelling in positive ($\kappa > 0$) and negative ($\kappa < 0$) circumferential directions are symmetric, which can reduce computational cost, as (4.1) only needs to be solved for $\kappa \geq 0$ [141, 45].

An analysis of the eigenfrequencies of a railway wheel, the corresponding mode shapes, and the derived mobilities is presented in Section 5.8. The projection of the surface displacements on the surface normal and the multiplication by $j\omega$ produce velocities that serve as input to the boundary element method.

4.2 Radiation from wheel vibration

The sound field produced by wheel vibrations is calculated numerically using the boundary element method. An approach to predicting sound radiation from a vibrating wheel in free space in cylindrical coordinates is introduced in the following section. This approach is then extended by introducing half-space Green's functions to model an infinite perfectly reflecting boundary.

4.2.1 Radiation from a wheel in free space

The axisymmetry of the wheel allows expressing all variables in cylindrical coordinates, for example, the pressure p at location $\mathbf{x}$ is $p(\mathbf{x}) = p(\theta_x, y_x, r_x)$ as introduced in Figure 4.1. A detailed derivation of the Fourier series BEM (FBEM) can be found in [165, 166, 43], and only a summary is given here. An advantage of describing the sound field in cylindrical coordinates is straightforward integration with the curved WFE method.

The approach is based on the three-dimensional Helmholtz integral

$$c(\mathbf{x})p(\mathbf{x}) = \int_S \left(p(\mathbf{y}) \frac{\partial G(\mathbf{x}, \mathbf{y})}{\partial \mathbf{n}} + j\omega\rho\ v_n(\mathbf{y}) G(\mathbf{x}, \mathbf{y}) \right) \mathrm{d}S \tag{4.6}$$

where $\mathbf{x}$ and $\mathbf{y}$ are coordinates of points in the surrounding medium and on the surface, respectively, $G(\mathbf{x}, \mathbf{y})$ is the three-dimensional free-space Green's function

$$G(\mathbf{x}, \mathbf{y}) = \frac{\mathrm{e}^{-jKR(\mathbf{x},\mathbf{y})}}{4\pi R(\mathbf{x}, \mathbf{y})} \tag{4.7}$$

and $R(\mathbf{x}, \mathbf{y})$ is the radius between the points $\mathbf{x}$ and $\mathbf{y}$. The sound field variables can be expanded in a Fourier series; for example,

$$p(\mathbf{x}) = \sum_{i=-\infty}^{\infty} p_i(y, r) \mathrm{e}^{-ji\theta_y} \tag{4.8}$$

where

$$p_i(y, r) = \frac{1}{2\pi} \int_0^{2\pi} p(\mathbf{x}) \mathrm{e}^{ji\theta_y} \mathrm{d}\theta \tag{4.9}$$

and similar for the other quantities. A modified Kirchhoff-Helmholtz equation based on the sum of the Fourier coefficients is derived;

$$c(\mathbf{x})p(\mathbf{x}) = -\int_\Gamma \sum_{i=-\infty}^{\infty} (j\omega\rho\ v_{n,i}(\mathbf{y}) H_i + p_i(\mathbf{y}) H_i') r_y \mathrm{d}\Gamma \tag{4.10}$$

where the integral is now over the 2D boundary Γ and H_i and H_i' are integrals of the Green's function

$$H_i = \int_0^{2\pi} G(\mathbf{x}, \mathbf{y}) \mathrm{e}^{ji\Theta} \mathrm{d}\theta \tag{4.11}$$

$$H_i' = \int_0^{2\pi} \frac{\partial G(\mathbf{x}, \mathbf{y})}{\partial \mathbf{n}} \mathrm{e}^{ji\Theta} \mathrm{d}\theta \tag{4.12}$$

with $\Theta = \theta_y - \theta_x$. The evaluation of H_i and H_i' is carried out efficiently in a one-dimensional Fourier transform [43]. This expression provides a relation between the pressures in two points. By discretising the boundary and using a collocation scheme, a system of equations can be produced of the form

$$\mathbf{Cp} + \mathbf{Hp} = \mathbf{Gv}_n \tag{4.13}$$

where surface velocities or pressures are known boundary conditions.

4.2.2 Radiation from a wheel above a reflective plane

A perfectly reflective plane is introduced by using a half-space Green's function

$$G_{hs}(\mathbf{x},\mathbf{y}) = \frac{\mathrm{e}^{-jKR(\mathbf{x},\mathbf{y})}}{4\pi R(\mathbf{x},\mathbf{y})} + R_p \frac{\mathrm{e}^{-jKR'(\mathbf{x},\mathbf{y})}}{4\pi R'(\mathbf{x},\mathbf{y})} = G(\mathbf{x},\mathbf{y}) + G_r(\mathbf{x},\mathbf{y}) \tag{4.14}$$

where R_p is the normal impedance at the boundary of the half-space, which in this simple model takes the value 1, and $R'(\mathbf{x},\mathbf{y})$ is the shortest distance between $\mathbf{x}$ and $\mathbf{y}$ via the reflective plane. The reflected field cannot be directly expanded into Fourier coefficients, since the field is not cylindrical and is centred at the origin of the coordinate system. Instead, a 2D Fourier transform has to be applied on $G_r(\mathbf{x},\mathbf{y})$,

$$G_r(\mathbf{x},\mathbf{y}) = \frac{1}{2\pi} \sum_{i=-\infty}^{\infty} \sum_{l=-\infty}^{\infty} H_{r,il} \mathrm{e}^{-j(i\theta_x - l\theta_y)} \tag{4.15}$$

where

$$H_{r,il} = \frac{1}{(2\pi)^2} \int_0^{2\pi} \int_0^{2\pi} 2\pi G_r(\mathbf{x},\mathbf{y}) \mathrm{e}^{j(i\theta_x - l\theta_y)} \mathrm{d}\theta_x \mathrm{d}\theta_y \tag{4.16}$$

and analogously for $\frac{\partial G_r(\mathbf{x},\mathbf{y})}{\partial \mathbf{n}}$ and $H'_{r,il}$. The modified Helmholtz integral expression then becomes

$$c(\mathbf{x})p(\mathbf{x}) = -\int_\Gamma \sum_{i=-\infty}^{\infty} \Bigg((j\omega\rho\ v_{n,i}(\mathbf{y}) H_i + p_i H'_i) \mathrm{e}^{-ji\theta_x} + \sum_{l=-\infty}^{\infty} (j\omega\rho\ v_{n,i}(\mathbf{y}) H_{r,il} + p_i H'_{r,il}) \mathrm{e}^{-jl\theta_x} \Bigg) r_y \mathrm{d}\Gamma\ . \tag{4.17}$$

Expressing the radiation of each Fourier order of the reflected field theoretically requires summing an infinite number of Fourier coefficients. Therefore, it is fundamental for this method to determine the required number of Fourier coefficients n_{fft} and efficiently calculate the coefficients H_i, H'_i, $H_{r,il}$, and $H'_{r,il}$. Kuijpers [43] developed an approach to find n_{fft} based on the relative position of $\mathbf{x}$ and $\mathbf{y}$. In *Paper F*, a description to find n_{fft} is presented for this 2D case.

Discretisation of the boundary, collocation, and assembly of the BE matrices as above leads to the expression

$$\mathbf{p}_i(\mathbf{y}) = \mathbf{G}_i(\mathbf{y})(\mathbf{v}_{n,i}) - \mathbf{H}_i(\mathbf{y})\mathbf{p}_i + \sum_l \big(\mathbf{G}_{r,il}(\mathbf{y})(\mathbf{v}_{n,l}) - \mathbf{H}_{r,il}(\mathbf{y})\mathbf{p}_l\big) \tag{4.18}$$

which is then solved for the unknown pressures. The coupling of the Fourier orders makes it necessary to include higher orders in the BE calculation than in the FE calculation. Section 5.9 presents a comparison between the half-space model and the free field model for the sound radiation regarding their radiation efficiency and directivity.

4.3 Sound of a passing wheel

Calculating the sound radiated by a passing railway wheel becomes computationally demanding when a high temporal and spatial resolution is required. Furthermore, the cylindrical coordinate system used for the FE and BE calculations previously is not convenient in a context where the wheel moves along the rail in a straight line.

The approach taken in *Paper G* to overcome these difficulties is summarised in this section. It uses a BE calculation to predict radiation patterns from the dynamic modes of the wheel, which are then expressed via equivalent sources in a spherical harmonics (SH) decomposition. The SH representation allows an efficient calculation of impulse responses of the modal radiation patterns for changing the source and receiver positions. The source signals, which describe the modal excitation amplitudes over time, are then convolved with the radiation impulse responses to predict the contribution of each mode to the sound pressure at a stationary receiver. Summing these complex pressures produces the total sound pressure during pass-by of the wheel. The following sections summarise each step in the calculation.

4.3.1 Sound radiation from wheel modes

Calculating the sound of each individual mode shape instead of the actual vibrations of the wheel has several advantages:

- The wheel typically has low material damping and its dynamic response is dominated by strong modes. This leads to long decay times in the sound radiation, requiring a high frequency resolution in the BE calculation. However, the acoustic transfer functions for each mode typically decay rather quickly. Separation of the dynamic and acoustic response allows for a lower frequency resolution in the BE calculation.
- Having calculated the radiation from each mode individually enables the efficient sound prediction for varying contact positions.
- A sensitivity analysis of the modal contributions to the sound pressure becomes possible.

The velocity field on the wheel in (4.2) is calculated as the sum of each mode shape $\Phi_l(\theta, \omega)$ scaled with the corresponding modal amplitude A_l given in (4.3). Analogously, the sound field around the wheel is calculated as the sum of the sound radiated from each mode shape $\mathbf{\Phi}_l$ scaled with A_l,

$$p(\mathbf{x}_\mathrm{r}, \omega) = \sum_l A_l(\omega) H_l(\mathbf{x}_\mathrm{r}, \omega). \tag{4.19}$$

The modal acoustic transfer functions H_l are obtained with a BE model where $A_0\mathbf{\Phi}_l$ is used as input velocity, where $A_0 = 1$ m/s. The complex pressure at a receiver position $\mathbf{x}_\mathrm{r}$ is then calculated for each mode l.

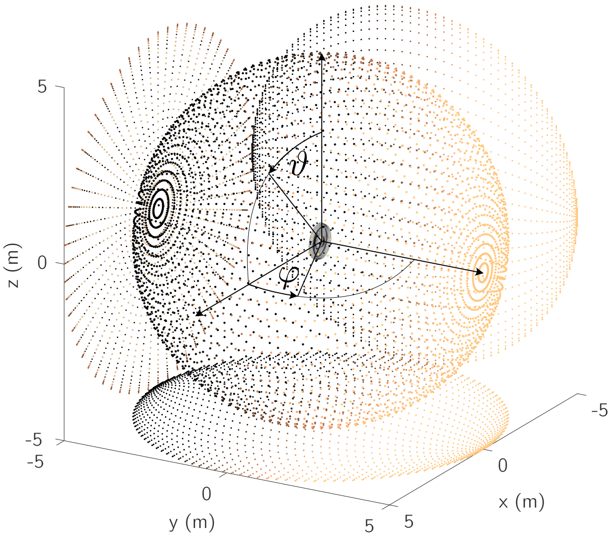

Figure 4.2: Position of the wheel and the receiver points on the reference surface in the FBEM calculation. Projections of the receiver points are included for orientation.

Each modal pattern produces a different frequency-dependent pattern H_l, due to the different relation between the wavelength in the surrounding fluid and the modal pattern on the wheel. When this frequency-dependent variation is rather smooth, a sparse frequency resolution can be sufficient.

4.3.2 Spherical harmonics decomposition of wheel radiation

While the method of calculating the pressure at arbitrary receiver points introduced above is sufficient to predict pass-by pressure signals, it is desirable to increase computational efficiency by introducing equivalent sources. A spherical harmonics representation of the sound field is used here because the orthogonality of the sources leads to a convergence of the reproduced field to the original field with increasing SH-order.

For each mode, the complex sound pressure is calculated in 3600 receiver positions in an equiangular spherical grid at 5 m radius around the wheel using the axisymmetric BE formulation introduced above. This spherical surface shown in Figure 4.2 acts as the reference surface. Each sound field is then described by a set of SH expansion coefficients. The SHs $Y_n^m(\varphi, \vartheta)$ of order n and degree m are a complete set of orthogonal functions on the sphere [167, Ch. 6.3.3], which depend on the azimuth angle φ and the zenith angle ϑ. The SH expansion is a multipole expansion; for example, the zeroth order SH $Y_0^0(\varphi, \vartheta)$ is a monopole and the first order SHs $Y_1^{\{-1,0,1\}}(\varphi, \vartheta)$ are dipoles that are aligned with the Cartesian axes. The SH expansion is implemented using an open-source Matlab library [168].

The pressure field $p(\varphi, \vartheta, \omega)$ calculated in the BEM can be expanded as a weighted sum of the SHs

$$p(\varphi, \vartheta, \omega) = \sum_{n=0}^{\infty} \sum_{m=-n}^{n} a_n^m(\omega)\ Y_n^m(\varphi, \vartheta) \tag{4.20}$$

where a_n^m are complex weights, also called expansion coefficients, of the SHs. Due to the orthogonality of the SHs, the expansion coefficients can be obtained by integration over the spherical surface S

$$a_n^m(\omega) = \int_S Y_n^m(\varphi, \vartheta)^*\ p(\varphi, \vartheta, \omega)\ \mathrm{d}S \tag{4.21}$$

where $(\cdot)^*$ denotes complex conjugation.

In this case, the sound pressure is only known at 3600 discrete observation positions. Expansion coefficients can be determined by limiting the SH order to a finite maximum order N. Equation (4.20) is then written as a matrix system

$$\mathbf{p}(\omega) = \mathbf{Y}_N \mathbf{a}_N(\omega)\ , \tag{4.22}$$

where the vector $\mathbf{p}(\omega)$ contains the $M = 3600$ sound pressures, and the matrix Y_N

$$\mathbf{Y}_N = \begin{bmatrix} Y_0^0(\varphi_1, \vartheta_1) & \dots & Y_N^N(\varphi_1, \vartheta_1) \\ \vdots & \ddots & \vdots \\ Y_0^0(\varphi_M, \vartheta_M) & \dots & Y_N^N(\varphi_M, \vartheta_M) \end{bmatrix} \tag{4.23}$$

is an $M \times (N+1)^2$ matrix that contains the SHs up to order N for the M observation positions. The expansion coefficients are obtained in a least squares solution as the length-$(N+1)^2$ vector

$$\mathbf{a}_N(\omega) = (\mathbf{Y}_N^{\mathrm{H}} \mathbf{Y}_N)^{-1} \mathbf{Y}_N^{\mathrm{H}}\ \mathbf{p}(\omega)\ , \tag{4.24}$$

where $(\cdot)^{\mathrm{H}}$ denotes the Hermitian transpose. Limiting the expansion order N to a finite number introduces an error, which is further investigated in *Paper G*.

4.3.3 Prediction of pass-by signals

The wheel is assumed to move with constant translational speed v along a straight line as shown in Figure 4.3. Therefore, the position of the wheel $(x_{\mathrm{S}}, 0, 0)$ changes with time t as $x_{\mathrm{S}} = vt$. The sound pressure at an observer point $(0, y_o, z_o)$ is calculated by, for each wheel mode, scaling the propagation functions between the source and observer position with a source signal and integrating over all source positions,

$$p_l(0, y_0, z_0, t) = \int_{-\infty}^{\infty} q'_{\mathrm{S},l}(x_{\mathrm{L}}, x_{\mathrm{S}}/v) h_l(x_{\mathrm{S}}, t - x_{\mathrm{S}}/v) \mathrm{d}x_{\mathrm{S}}\ , \tag{4.25}$$

where $h_l(x_{\mathrm{S}}, t)$ is the propagation function for mode l and $q'_{S,l}$ is the source strength per unit length. Finally, the contributions from all modes are added.

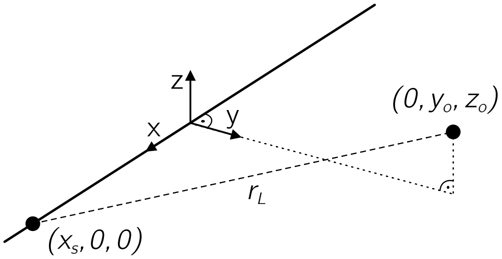

Figure 4.3: Axis definition and position of the wheel and stationary microphone. The solid line indicates the trajectory of the wheel.

The propagation function $h_l(x_\mathrm{S}, t)$ describes the acoustic transfer from the mode shape to the observer position and is computed as follows. The sound pressure radiated by the mode shape $\mathbf{\Phi}_l$ is calculated at 3600 points in the BEM as described in 4.3.1 and spherical harmonics expansion coefficients are derived as described in 4.3.2. The expansion coefficients of the pressure field on the reference surface with radius r_0, which encloses the wheel, allow calculating the pressure field on any larger sphere with radius $r > r_0$ by using spherical Hankel functions $\mathrm{h}_n(Kr)$ [167, Eq. 6.94],

$$H_l(r_\mathrm{S}, \varphi_\mathrm{S}, \vartheta_\mathrm{S}, \omega) = \sum_{n=0}^{\infty} \frac{\mathrm{h}_n(Kr_\mathrm{L})}{\mathrm{h}_n(Kr_0)} \sum_{m=-n}^{n} a_n^m(\omega)\ Y_n^m(\varphi_\mathrm{S}, \vartheta_\mathrm{S}) \ , \tag{4.26}$$

with

$$\begin{aligned} r_L &= \sqrt{(x_\mathrm{S}^2 + y_o^2 + z_o^2)} \ , \\ \varphi_\mathrm{S} &= \pi - \arctan\left(\frac{z_o}{\sqrt{x_S^2 + y_o^2}}\right) \ , \text{ and} \\ \vartheta_\mathrm{S} &= \arctan\left(\frac{y_o}{x_S}\right) \ . \end{aligned} \tag{4.27}$$

The modal acoustic propagation function $h_l(x_\mathrm{S}, t)$ is then obtained by an inverse Fourier transform of $H_l(r_\mathrm{S}, \varphi_\mathrm{S}, \vartheta_\mathrm{S}, \omega)$.

The source signal is given by the modal amplitude $A_l(x_\mathrm{S}, \omega)$ of the wheel as defined in (4.3). The modal amplitude is divided into two terms $A_l(x_\mathrm{S}, \omega) = F_{\mathrm{A},l}(\omega) b_l(\omega)$, where $F_{\mathrm{A},l}(x_\mathrm{S}, \omega)$ represents the excitation

$$F_{\mathrm{A},l}(x_\mathrm{S}, \omega) = j\omega \mathbf{F}_\mathrm{e}(x_\mathrm{S}, \omega) \mathbf{\Phi}_l(\mathbf{x_0}) \ , \tag{4.28}$$

and $b_l(\omega)$ is given in (4.4).

In the time domain, $F_{\mathrm{A},l}(x_\mathrm{S}, t)$ is the time derivative of the contact force scaled with $\mathbf{\Phi}_l$. An analytical expression of $b_l(\omega)$ in the time domain can be derived as $b_l(\omega)$ describes the frequency response of a simple oscillator whose inverse Fourier transform is

$$b_l(t) = \frac{e^{-2\omega_l \zeta_l t}}{\Lambda_l \omega_l'} \sin(\omega_l' t) \mathrm{H}(t) \ , \tag{4.29}$$

with $\omega_l' = \sqrt{\omega_l^2 - \omega_l^2 \zeta_l^2}$ and the Heaviside step function $\mathrm{H}(t)$. The source signal $q_{\mathrm{S},l}'$ is finally obtained by convolution of the two parts

$$q_{\mathrm{S},l}'(x_\mathrm{S}, x_\mathrm{S}/v) = \int_{-\infty}^{x_\mathrm{S}/v} F_{\mathrm{A},l}(x_\mathrm{S}, \tau) b_l(x_\mathrm{S}/v - \tau) \, \mathrm{d}\tau \; , \tag{4.30}$$

where the upper limit of the integral is set due to causality requirements, that is, future contact forces should not influence the results at the current time $t = x_\mathrm{S}/v$.

The source signal $q_{S,l}(x_\mathrm{S}, t)$ of each mode is multiplied with the propagation function $h_l(x_\mathrm{S}, t)$ to obtain the pressure at the microphone. In discrete time and space, (4.25) is a sum of the modes and source positions included,

$$p(0, y_o, z_o, t) = \sum_l \sum_{-N_\mathrm{S}}^{N_\mathrm{S}} q_{\mathrm{S},l}(x_\mathrm{S}, x_\mathrm{S}/v) \; h_l(x_\mathrm{S}, t - x_\mathrm{S}/v) \; , \tag{4.31}$$

The amplitude $q(x_\mathrm{S}, x_\mathrm{S}/v)$ to scale the propagation function is

$$q_{\mathrm{S},l}(x_\mathrm{S}, x_\mathrm{S}/v) = \int_{x_\mathrm{S}/v - \Delta t/2}^{x_\mathrm{S}/v + \Delta t/2} q_{\mathrm{S},l}'(x_\mathrm{S}, t) \mathrm{d}t \; , \tag{4.32}$$

where Δt is the time resolution of the numerical simulations when calculating the contact forces. Application examples are presented in Section 5.10.

5 Applications of the model

This chapter presents applications of the models developed in the previous chapters. Sections 5.1 to 5.7 cover applications and results related to the track. Sections 5.8 to 5.10 present results related to wheel vibrations and sound radiation.

To verify that the dynamic model for the discretely supported ballasted track produces reliable predictions, comparisons with measured input and transfer receptances are shown in Section 5.1. This modelling approach is then extended to simulate the dynamic response of a slab track system in Section 5.2, where it is validated by first tuning the model with a selection of measurements and then comparing it with other measurements. This section is a summary of the results in *Paper A*. This approach to simulate vibrations of the slab track surface, coupled to a WBE model for sound radiation, is used in Section 5.3 to investigate the effect of the stiffness of the rail pad on sound radiation from the slab surface and the rail, which are the results of *Paper B*. The topic of noise mitigation at the source using existing track components is continued in Section 5.4, where a parametrised two-stage elastic support is introduced between the rail and the slab. The goal is to optimise the track parameters to reduce both ground borne vibrations and air borne noise. This section presents the results of *Paper E*. This paper also uses an efficient method to predict the sound field around a vibrating railway track by precalculating acoustic transfer functions, which is described in *Paper C*. These transfer functions are presented and analysed in Section 5.5. Coupling these transfer functions to a vibrating rail or sleepers allows the description of the sound field surrounding a railway track, which is described in Section 3.3. Examples of sound fields created by harmonic excitation of a simple ballasted track are presented in Section 5.6. It of course matters which model is used to calculate the track vibrations in the first place. *Paper D* quantifies some of the effects of the dynamic track model on the radiated sound field, and a selection of the findings is presented in Section 5.7.

The model for wheel vibrations described in Section 4.1 is used to investigate one railway wheel in Section 5.8. Its modal behaviour, dispersion relation, and mobility at the contact point are analysed. The hard surface of slab tracks introduces ground reflections of the sound radiated from the wheel. The effect of the presence of a reflective plane is investigated in *Paper F*. Section 5.9 summarises the results of this analysis. In *Paper G*, the directivity of the wheel modes and their contribution to the pass-by sound pressure level is investigated. Section 5.10 summarises the findings of this analysis.

5.1 Modelling the dynamic response of a ballasted track

To validate the modelling approach of the discretely supported track presented in Section 3.1, comparisons to impulse hammer measurements are presented in the following. These impulse measurements were carried out on the German rail network on a ballasted

Table 5.1: Modelling parameters to match the measured input receptance.

Vertical pad stiffness (kN/mm)	115
Vertical pad loss factor (-)	0.25
Lateral pad stiffness (kN/mm)	14.4
Lateral pad loss factor (-)	0.2
Vertical ballast stiffness (kN/mm)	58
Vertical ballast loss factor (-)	1
Lateral ballast stiffness (kN/mm)	0.5
Lateral ballast loss factor (-)	0.7
Sleeper mass	140

track in the context of the Roll2Rail project (see [169]). In each measurement, the rail is excited at a certain distance from an accelerometer placed in the centre of a sleeper bay. Transfer functions, measured according to the EN 15461 standard [170], were used to determine the decay rate of the investigated track. For each excitation position, two measurements were made in each direction, one with a hard hammer tip and one with a soft hammer tip. The hard tip has a shorter contact time with the rail which excites high frequencies effectively. The soft tip, on the other hand, has a longer contact time, exciting low frequencies more efficiently, increasing the measurement quality in this frequency range.

5.1.1 Model setup and parameters

The model consists of a WFE-based rail that is discretely supported by spring-mass-spring systems, representing the rail pad, the sleeper, and the ballast. In each rail support, the spring-mass-spring systems act independently in the vertical and horizontal directions. In the support, the vertical and horizontal directions are uncoupled. Nevertheless, a coupling between these directions exists via the 3D model of the rail. The rail pad is represented by six springs, three across the width of the rail, and two in the length direction, all of which have identical stiffnesses. The sleeper spacing is 0.6 m. 109 sleepers are included in the calculation.

The numerical model is tuned using the input receptance, and then compared to the transfer receptances to positions further away from the excitation position. The modelling parameters were tuned by iteratively adjusting the parameters and comparing the predicted input receptance with the measurement. A list of model parameters is given in Table 5.1. Thompson et al. [169] adapted a Timoshenko beam model on a dual layer foundation [23] to these measurements and found a pad stiffness of 105 kN/mm in vertical and 14 kN/mm in lateral direction, which is similar to the parameters found here.

5.1.2 Comparison to measured receptances

Figures 5.1 and 5.2 show comparisons between the predicted and measured vertical and lateral receptances. The top left subfigures show each input receptance used for tuning the model parameters. The distance between the excitation and the vibration sensor in the sleeper bay is indicated in the top right of each subfigure. In general, a good alignment between the prediction and the measurements is found.

For the vertical receptance, the resonance of the sleepers on the ground at around 100 Hz, the cut-on frequency of the vertical bending waves in the rail at about 300 Hz and the pinned-pinned resonances are clearly visible. With increasing distance, the sleeper resonance becomes less pronounced. Since the sleepers are only excited indirectly via the rail and the rail only has a decaying near-field below the cut-on frequency of the bending wave, the sleepers do not vibrate significantly at larger distances and low frequencies. The high vibration levels measured at low frequencies are probably due to background noise in the measurement. Above the cut-on frequency, vibrational energy is transferred over larger distances, which is successfully predicted in the model. At very high frequencies, the wavelengths of the waves in the rail get closer to the dimension of the rail pad, which in turn become more efficient at absorbing the vibrational energy. As a consequence, the transfer functions have a lower magnitude at high frequencies and larger distances.

Similar observations can be made for the lateral direction in Figure 5.2. The lateral bending wave cut-on frequency is found at about 80 Hz. Several peaks and dips related to the pinned-pinned frequency of lateral bending waves are observed and aligned between the measurement and the simulation. The impact of the lateral hammer on the rail head also excites other wave types (such as torsional waves), which themselves create pinned-pinned resonances. These resonances are not as pronounced in the lateral direction due to the softer stiffness of the rail pad. It was observed that the length-wise spacing of these springs the rail has a large influence on the damping of the pinned-pinned resonance.

In general, a satisfactory match was found between the predicted and measured transfer functions, even over long distances, especially considering that the model was adjusted only on the basis of the transfer function at the closest position.

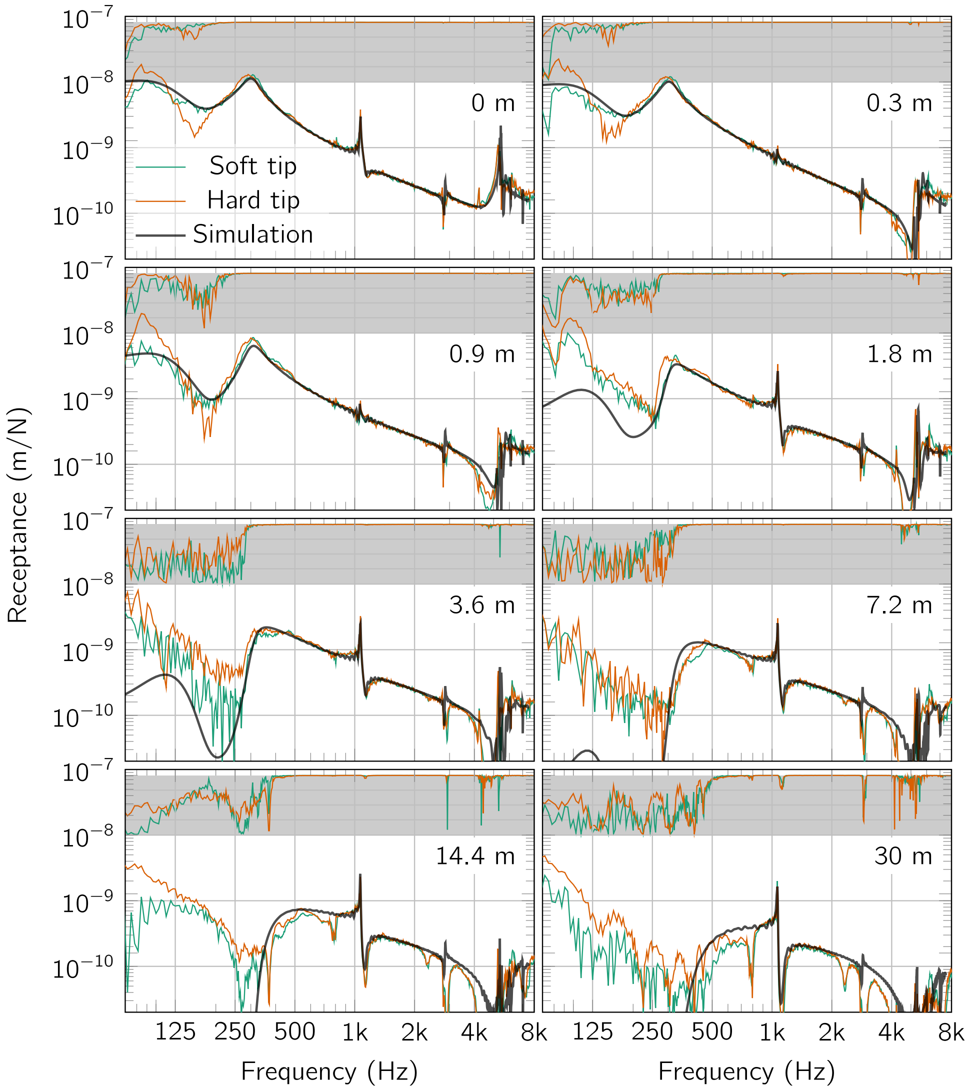

Figure 5.1: Measured and simulated vertical transfer functions of the ballasted track. 'Hard tip' and 'soft tip' refer to the impact hammer measurements with the corresponding hammer tip being used. The coherence of the respective measurement is indicated in the shaded rectangle at the top of each plot. The coherence takes values between zero and one, with one located at the top of the rectangle.

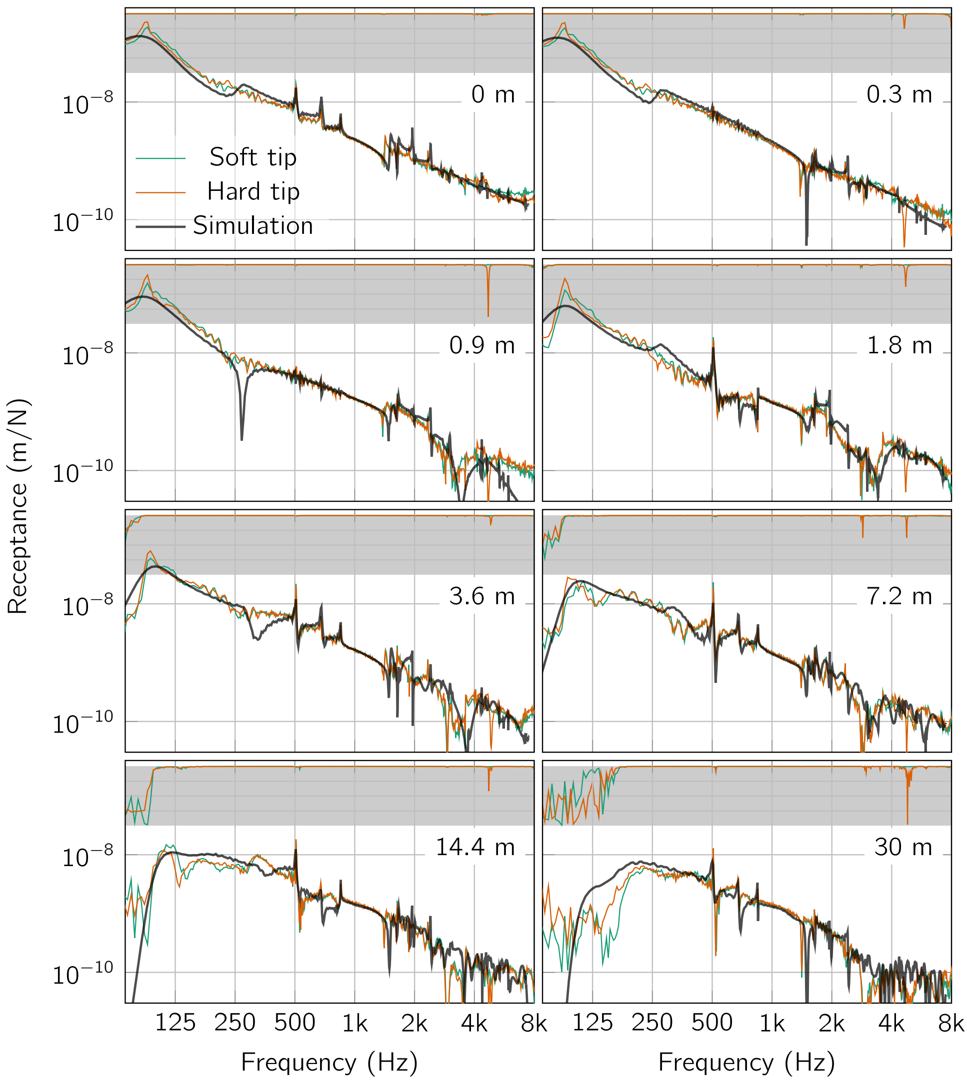

Figure 5.2: Measured and simulated lateral transfer functions of the ballasted track. 'Hard tip' and 'soft tip' refer to the impact hammer measurements with the corresponding hammer tip being used. The coherence of the respective measurement is indicated in the shaded rectangle at the top of each plot. The coherence takes values between zero and one, with one located at the top of the rectangle.

5.2 Modelling and calibrating the dynamic response of a slab track

The section above proves that a WFE model of the rail with a simple discrete support can produce plausible transfer functions between points on the rail surface. This section focusses on transfer functions for an excitation on the rail to vibration on a slab track surface. As in the case above, impulse-hammer measurements are used to adapt and validate the model.

Measurements are carried out on a full-scale slab test rig at the State Key Laboratory of Traction Power of Southwest Jiaotong University in Chengdu, China. Zhai et al. describe the full testing platform in more detail [171]. The test track comprises multiple track sections common in the Chinese railway network, of which one, the CRTS-III, is investigated here. The cross section of the track is shown in Figure 5.3. The top layer is a pre-fabricated concrete slab. It rests on a layer of self-compacting concrete (SCC), used for adjusting the position of the pre-fabricated slabs during the construction of the track. The SCC, in turn, is laid on a thick concrete support layer that then rests on the soil. Wang et al. [172] present material data to each of the layers.

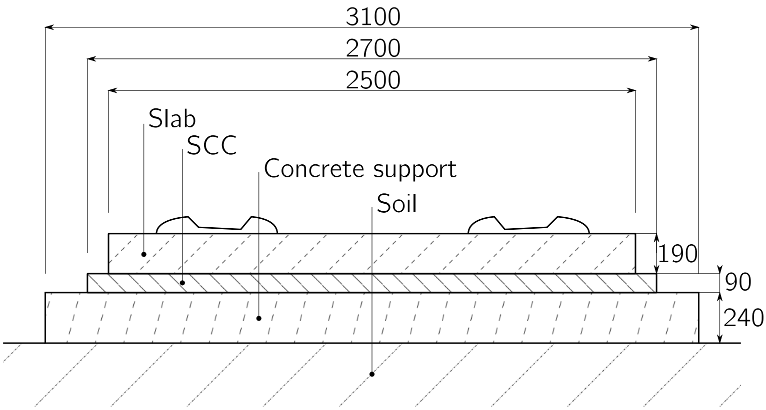

Figure 5.3: Cross-section of the CRTS-III track. Dimensions in mm.

5.2.1 Measurement setup

The CRTS-III track section comprises three slabs of about 5.5 m length. Each slab has eight rail seats per rail, with a spacing of about 0.68 m between the rail seats. During the measurements, the central of the three slabs was equipped with 5 accelerometers, numbered 1 to 5 in Figure 5.4. Sensors 1 and 5 were uniaxial sensors, measuring only the vertical direction. Sensors 2, 3, and 4 measured vertical and lateral accelerations. The structure was excited at six positions, three on each rail, by iterative hits with a large impact hammer. At each position, the rail was hit vertically and laterally. These positions are indicated in Figure 5.4, labelled with Roman numerals and with the index 'c' for 'close rail' and 'f' for 'far rail'. This produces a total of 96 combinations of excitation position and acceleration. The impulse responses were transformed to frequency domain for further processing.

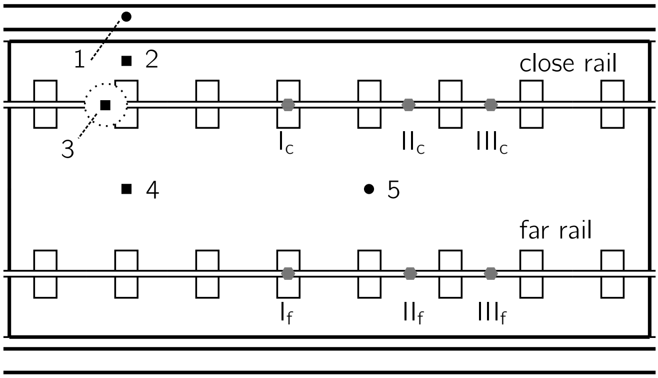

Figure 5.4: Locations of accelerometers and excitations in the measurement.

5.2.2 Model and tuning of modelling parameters

The model consists of two WFE models, one for the rail and one for the supporting concrete and soil layers, which are discretely coupled at the positions of the rail seats. The discretised cross-section of each of the WFE models is presented in Figure 5.5. The soil layer has a fixed boundary condition at the bottom nodes. Three nodes across the rail foot are connected to the slab track surface via linear elastic springs representing the rail pad. Damping in the rail pad is introduced with a complex loss factor.

The model was calibrated using four of the excitation positions, position I and III on each rail. While some modelling parameters could be directly adapted from [172], others could be adjusted such that a better match between the measurement and the simulation was achieved. Calibrating the model included two steps, a parametric study, and a genetic algorithm. The calibration process, as well as the final set of parameters, is described in detail in *Paper A*.

5.2.3 Comparison between measurements and the calibrated model

The large number of measured and predicted transfer functions is efficiently compared by employing a 2D visualisation. The average difference in dB between the measured and simulated receptance is evaluated per third-octave band. Then these third-octave differences for each sensor are arranged in a grid as shown in Figure 5.6.

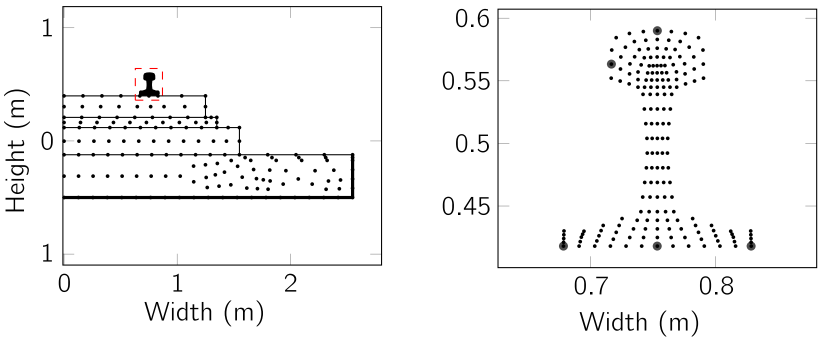

Figure 5.5: FE nodes of the cross-section of the slab track model. The thick nodes on the rail head mark excitation positions, and the ones on the rail foot mark the nodes at which the rail was connected to the slab via the rail pad stiffness. Only half of the symmetric slab track is shown.

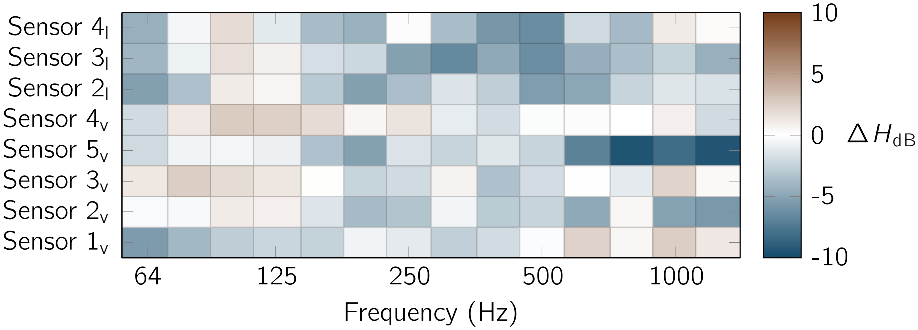

Figure 5.6: Difference between the predicted and measured transfer functions from a vertical excitation at $\mathrm{II_c}$ to all sensors.

Positive differences (brown colour) indicate that the model over-estimates the response. The figure shows these differences for the vertical excitations at position II_c. The transfer functions corresponding to this excitation position were not included in the model calibration. The three upper rows represent lateral responses. Below 50 Hz, the model generally underestimates the response. Between 64 Hz and 125 Hz, the model tends to slightly overestimate the response for both lateral and vertical channels. Above that, the model tends to slightly underestimate the response. Yet, a good agreement is observable between the prediction and the measurement.

An analogous evaluation is carried out for the lateral excitation at the same position, shown in Figure 5.7. Larger differences are observed in this case. The lateral transfer functions tend to be slightly overestimated by the model, especially in the frequency range 80 Hz to 125 Hz. Vertical displacements are underestimated to varying degrees by the model, especially above 500 Hz. *Paper A* additionally presents the transfer functions that were included in the calibration, with results comparable to the two figures presented.

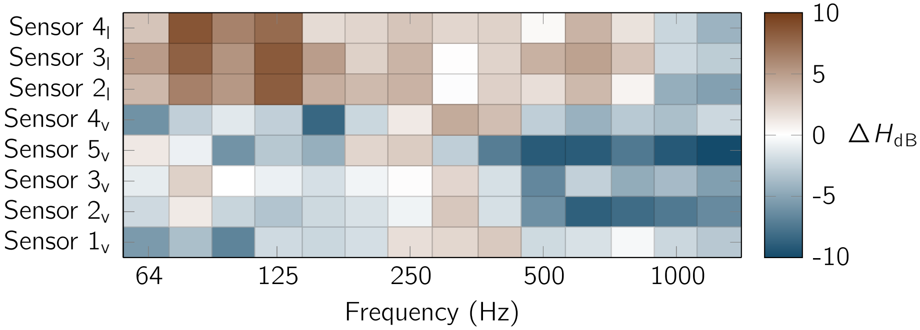

Figure 5.7: Difference between the predicted and measured transfer functions from a lateral excitation at II_c to all sensors.

Deviations between simulation and measurement can have several reasons. Inaccuracies in the measurement can be introduced by non-ideal excitation of the rail, especially with respect to the exact excitation position and -direction. The model assumes an infinitely long rail and track support, whereas the real rail is cut on both sides of the CRTS-III track section. The consequence of the finite rail is investigated in more detail in *Paper A*. Another aspect is that the model for the rail pads does not take into account a coupling between the vertical and lateral directions, which might introduce further uncertainties.

In general, a satisfactory agreement is found between the measured and calculated transfer functions, both for those transfer functions included in the calibration and for the others. This means that the approach is suited to represent the dynamic properties of the test rig.

5.3 The sound power radiated by a slab track with varying rail pad stiffnesses and rail supports

The model for the structural response of the rail and the slab track surface is now extended with a numerical approach to calculate the sound radiation from surface vibrations. A parameter study is conducted to examine the effect that (1) the stiffness of the rail pad, (2) the thickness of the slab, and (3) the discrete or continuous support of the rail have on the sound power radiated from the involved structures.

5.3.1 Description of the model

The model presented in Sections 3.1 and 3.2 is utilised to predict sound power. For this, the dynamic model for the slab and its support layers is simplified compared to the track model developed in *Paper A* and consists only of a ground and a concrete layer. Details are described in *Paper B*. The rail is a standard UIC60 profile. In the parameter study, the vertical rail pad stiffness is set to 10, 20, 40, 80, 160 or 320 kN/mm. Slab thicknesses of 10 cm and 20 cm are investigated. A sketch of the setup is shown in Figure 5.8, in which also the different types of support are indicated. Note that the solution strategy

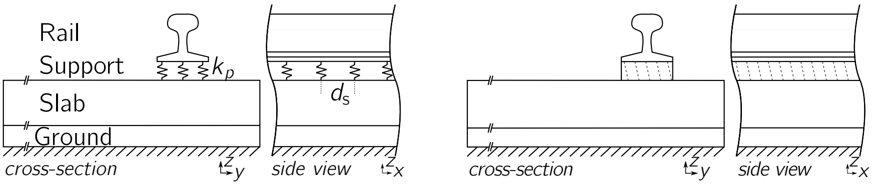

Figure 5.8: Model setup for the discretely (left) and continuously (right) supported rail. The lateral springs are not shown in the left image.

is slightly different for the different supports. For the discrete support, the slab and the ground are one WFE model, and the rail is a separate WFE model, which are then coupled via linear elastic springs in a finite number of positions. The positions are each 0.65 cm apart. For the continuous support, all four components are included in one WFE model. The Young's modulus of the continuous rail pad is adjusted so that the stiffness per unit length matches the desired rail pad stiffness. The alignment between both models is shown by comparing the vertical and lateral receptance on the rail.

The WFE models of the track components produce transfer functions from the excitation force to the surface displacement in the frequency-wavenumber domain. This surface displacement serves as an input to a Wavenumber domain Boundary Element model (WFE) to calculate the radiated sound field around the structure. The sound power is evaluated by integrating the sound intensity over the surface of the structure. Nilsson et al. describe this in detail [42].

5.3.2 Sound power produced by rail and slab surface

The sound power levels produced by rail and slab vibrations are presented in Figure 5.9. The results for the vertically excited, discretely supported rail on the left show a relatively broad peak at the resonance of the vertical bending waves, between 80 Hz and 250 Hz, depending on the stiffness of the rail pad. In general, the radiated sound power increases with increasing frequency. Analogous to ballasted tracks, the total radiated sound power is lower for tracks with a higher rail pad stiffness. The effect is not as significant when the rail is excited laterally.

The sound power radiated from the continuously supported rail and the slab track is shown on the right in Figure 5.9. Compared to the discretely supported track, it is notable that (a) the radiation at low frequencies is significantly increased, especially in the case of low rail support stiffness, and (b) the sound radiation is significantly decreased at high frequencies. In this case, the L_W is almost constant over frequency above the resonance of the vertical rail bending wave. The increased radiation at low frequencies is likely due to the higher radiation efficiency of the continuously supported rail compared to the discretely supported rail [42]. Continuous support further increases the damping of waves travelling on the rail, which decreases the radiation at high frequencies.

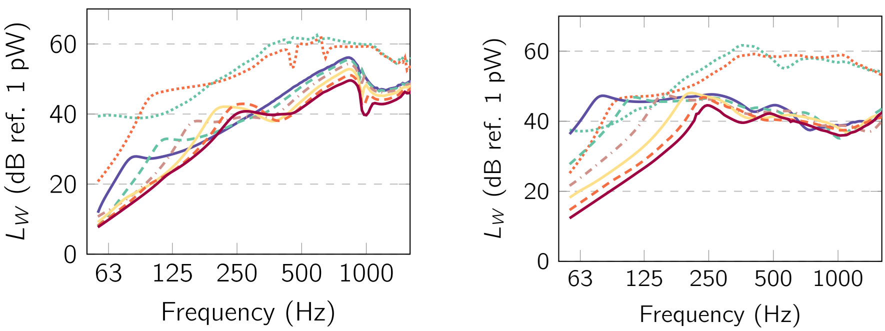

Figure 5.9: Radiation from a 20 cm slab at vertical excitation on the rail for different rail pad stiffnesses k_s: 10 kN/mm (—), 20 kN/mm (- - -), 40 kN/mm (-·-), 80 kN/mm (—), 160 kN/mm (- - -) and 320 kN/mm (—). Lateral excitation included for 20 kN/mm (·····) and 160 kN/mm (·····). Left: Discrete support, Right: Continuous Support.

The individual contributions of rail and slab to the total radiated sound power are investigated in Figure 5.10. It is visible that the with a low standard rail pad stiffness of 20 kN/mm, the slab surface does not contribute significantly to the radiated noise above 63 Hz. At 80 kN/mm rail pad stiffness, the slab surface dominates the sound radiation up to 125 Hz.

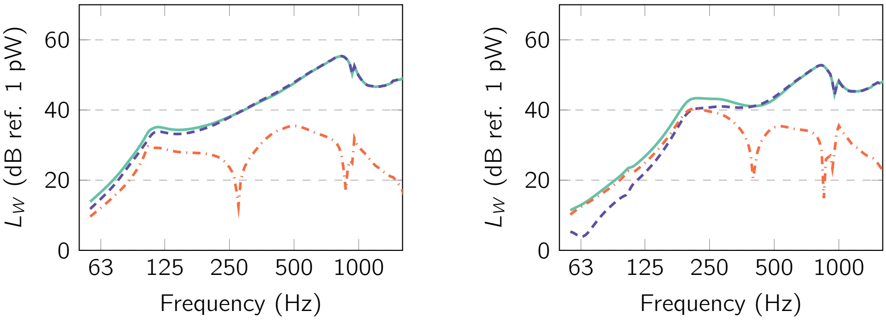

Figure 5.10: Contribution of rail (- - -) and slab (-·-) to the total radiated sound power (—) in case of a discretely supported rail on a 20 cm thick slab. Left: $k_p = 20$ kN/mm, Right: $k_p = 80$ kN/mm.

5.4 Addressing slab track vibration and noise performance with a two-stage elastic support

Ballastless tracks produce higher noise levels than ballasted tracks for two main reasons: First, the stiffness of the rail seat is typically lower, so a longer section of the rail vibrates and radiates noise. Second, the ballast between the sleepers absorbs some of the noise. While increasing the rail pad stiffness can potentially mitigate some of the radiated noise, it also increases the transfer of vibrational energy into the supporting structures and the ground. However, typically air borne noise and ground borne vibration are problems in different frequency ranges, where ground borne noise is significant up to about 250 Hz, and the sound radiation from the rail dominates between 500 Hz and 4 kHz. Rail support systems that feature a two-stage elastic support (i.e., bottom to top: a lower spring, the sleeper mass, an upper spring, the rail), such as systems with booted sleepers, produce a frequency-dependent stiffness. This stiffness can be tuned by adjusting the stiffnesses and masses involved. Here, this filtering effect is explored by conducting a parameter study in which the three mentioned parameters are adjusted. The goal of the study is to investigate the effect of the parametrised rail support on a) the sound radiation from the rail, the sleeper, and the slab surface, b) the contact forces, and c) the forces acting on the elastic components.

5.4.1 Model description and study parameters

The simulation setup consists of three main components: firstly a model of the dynamic response of track and wheel, secondly an interaction model for calculating the rolling contact forces, and thirdly the calculation of the pass-by quantities such as the sound power. Radiation of the wheel is neglected here.

The dynamic track model consists of two discretely coupled WFE models, one of which

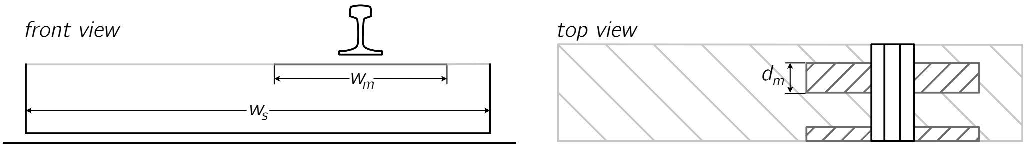

Figure 5.11: Sketch of the radiating surfaces, including a rail and an approximation of a track superstructure on which normal velocities are specified. An acoustically hard surface is included via half-space Green's functions.

represents the rail and the other representing the concrete slab and its support layers. These two components are discretely coupled in 99 positions by analytical spring-mass-spring systems that represent the lower elastic layer, the sleeper, and the rail pad. The number of sleepers is odd as one sleeper is placed at $x = 0\ m$ and it was empirically found that including more than about 100 sleepers does not affect the predicted receptance significantly (see also [99]). The methodology necessary to model two-stage discrete elastic rail supports is developed in *Paper E*. The parameters for the mass m and the two stiffnesses k_a and k_b (a and b for "above" and "below" the mass) are presented in Table 5.2. There are a total of 60 combinations of parameters.

Table 5.2: Study parameters

Vertical stiffness above the mass k_a (kN/mm)	25, 50, 100, 200, 400, 800
Weight of the mass m (kg)	8, 16, 32, 64, 128
Vertical stiffness below the mass k_b (kN/mm)	20, 40

The dynamic interaction between the wheel and the rail is simulated in the time domain using the in-house software WERAN. Calculations assume a preload of 55 kN, a vehicle speed of 100 km/h, and only take into account vertical interaction. A 50 m long, straight track section is considered. For each calculation, the wheel and track roughness are identical and based on measurements presented in [169, 173].

The radiation from the track is computed using the WBE method. The rail, the sleepers, and the slab contribute to the predicted sound field. A sketch of the included radiating surfaces is presented in Figure 5.11. The surface vibration of the rail and slab is evaluated in the wavenumber-frequency domain and serves directly as the input to the WBE method. The vertical vibration of the sleepers is calculated based on the forces acting on each sleeper. This spatial information is transformed into a wavenumber spectrum, again serving as the input to the WBEM model for the radiation. The total radiated sound power is evaluated by integrating the sound intensity on an infinitely long half-cylinder with 5 m radius around the track. For increased calculation efficiency, the acoustic transfer functions from each surface point on the vibrating structures to each receiver point on the cylinder are precalculated. Assuming that the surface area of each sleeper depends on its weight, its widths w_m and depths d_m were roughly adjusted by linear interpolation between dimension ($w_m \cdot d_m$) 15 cm·10 cm to 70 cm·30 cm.

5.4.2 Parameter study results and noise mitigation potential

A time-domain calculation of the contact forces was carried out for each of the 60 combinations. From the vertical rolling contact forces, the forces in each rail seat, the sleeper vibration, and the radiated sound power are then derived. Figure 5.12 presents the effect of altering the stiffness k_a on the peak forces in the rolling contact $\hat{F}_c$ and in the two elastic components in the support ($\hat{F}_a$ and $\hat{F}_b$). The first column shows the simulated vertical peak force $\hat{F}_c$. It generally increases with increasing stiffness k_a. Towards higher stiffnesses, this increase generally flattens out and the mass becomes more influential due to its stronger coupling to the rail. The forces $\hat{F}_a$ and $\hat{F}_b$ describe the loads on the track

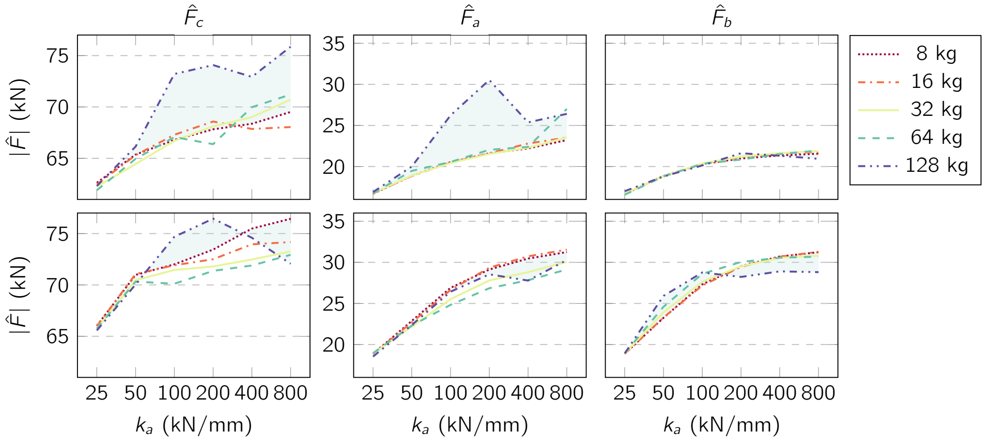

Figure 5.12: Influence of the support parameters on the peak forces $\hat{F}_c$, $\hat{F}_a$, and $\hat{F}_b$. For orientation, the area between the lightest and the heaviest mass is coloured in blue. Top: k_b = 20 kN/mm, bottom: k_b = 40 kN/mm.

components and indicate the level of ground borne vibrations. These are shown in the centre and right column in Figure 5.12. As above, it is observable that the weight of the mass becomes more influential with a stiffer k_a. Additionally, a stiffer k_b leads to a stronger dependence on k_a, that is, the flattening of the curves above 200 kN/mm is more distinct for k_b=20 kN/mm. Expectedly, lighter masses lead to more similar forces above and below the masses.

The sound power radiated from each component is presented in Figure 5.13. While the rail is the dominant noise source in all cases, the slab has a negligible influence on the A-weighted level. The sleepers become more influential with increasing stiffness k_a. The increase in surface area and the increase in sleeper mass seem to balance each other to some degree, so the sleeper contributes within a $\pm$ 3 dB range for each k_a.

A comprehensive summary of the results is found in Figure 5.14. Each mark corresponds to one simulation. The graphs show the peak forces on the horizontal axis and the total sound power level on the vertical axis. On the left, the maximum predicted rolling contact force is shown. A diagonal trend from the top left to the bottom right is visible,

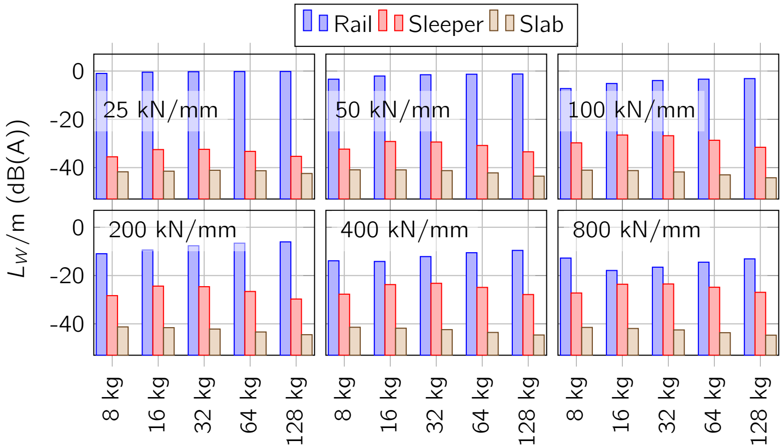

Figure 5.13: Normalised sound power radiated from the different components for different k_a as indicated in each top left corner. These are results for $k_b = 40$ kN/mm.

which indicates that track setups favouring lower noise levels also lead to higher contact forces. In many cases, the sound power is similar for both k_b, while $\hat{F}_c$ is higher for $k_b = 40$ kN/mm. This means, the L_W depends mostly on k_a, whereas the $\hat{F}_c$ depends on a combination of all parameters.

This diagonal trend is also found for $\hat{F}_a$ in the central figure, which means that a reduction in L_W is 'bought' with an increased load on the sleepers. Vertically arranged markers indicate the potential to optimise the track, since in these cases the L_W can be reduced without changing $\hat{F}_a$. Here, a reduction of the L_W by 5 dB(A) seem possible without significantly affecting $\hat{F}_a$. For $\hat{F}_b$, up to 10 dB(A) reduction in the L_W seems possible for the softer k_b. It can be concluded that for a two-stage support, a soft stiffness below the central mass has the potential to achieve both vibration isolation and reduction of the L_W. The ideal rail seat receptance for this is however dependent on the combined roughness of wheel and rail and should not be generalized from these results.

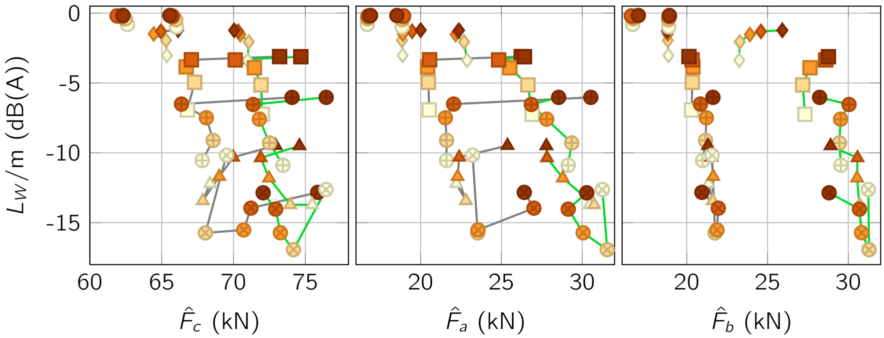

Figure 5.14: Comparison of the maximum forces in the rolling contact $\hat{F}_c$ (left), the rail seat $\hat{F}_a$ (centre), and into the slab $\hat{F}_b$ (right) to L_W. The symbols' colours indicate the mass (■■■■■ for 8 kg, 16 kg, 32 kg, 64 kg and 128 kg, respectively), and their shapes represent different rail pad stiffnesses k_a (○◇□⊕△⊗ for 25 kN/mm to 800 kN/mm, respectively). The line color indicates the stiffness k_b, (▬ ▬ for 20 kN/mm and 40 kN/mm, respectively).

5.5 Description and interpretation of precalculated acoustic transfer functions

The method to calculate the sound field produced by railway track vibrations relies on precalculated acoustic transfer functions for increasing the numerical efficiency. These describe the sound pressure produced in a set of receiver points for a unit normal velocity on the surface nodes of the structure. The transfer functions are specific to the acoustic geometry, defined by the boundaries of the included objects. The following section describes the geometries for which these transfer functions have been evaluated. Then, the transfer functions of one geometry are presented and interpreted.

5.5.1 Description of the acoustic geometries

Transfer functions have been precalculated for four geometries, sketched in Figure 5.15. The geometries are (a) a UIC 60 rail in free space, (b) the same rail 5 cm above an infinite, acoustically hard surface, (c) the same rail 5 cm above a flat structure which itself is positioned above an infinite, acoustically hard surface, and (d) the rail and track structure below the simplified hull of a passenger train. The track surface is centred laterally while the rail located at the position of the right rail for a standard gauge of 1.435 m. Figure 5.16 shows the setup used in geometry (d). The other geometries can be derived by removing the respective components. All surface nodes, field points and CHIEF points used in the calculation are marked in the figure. The surface nodes for which the transfer functions have been calculated are indicated in green. Other (passive) surface nodes are coloured blue. All surface nodes are spaced with 7.5 mm to achieve

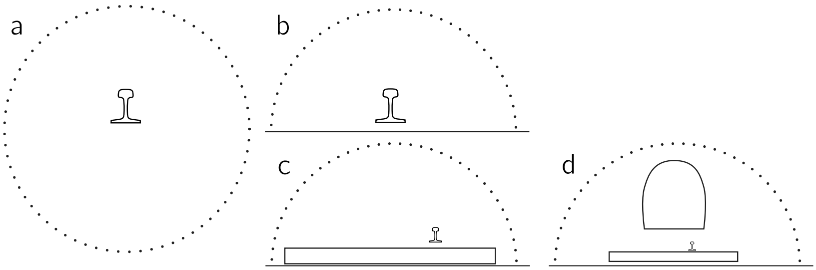

Figure 5.15: BE geometries for which the acoustic transfer-functions have been precalculated.

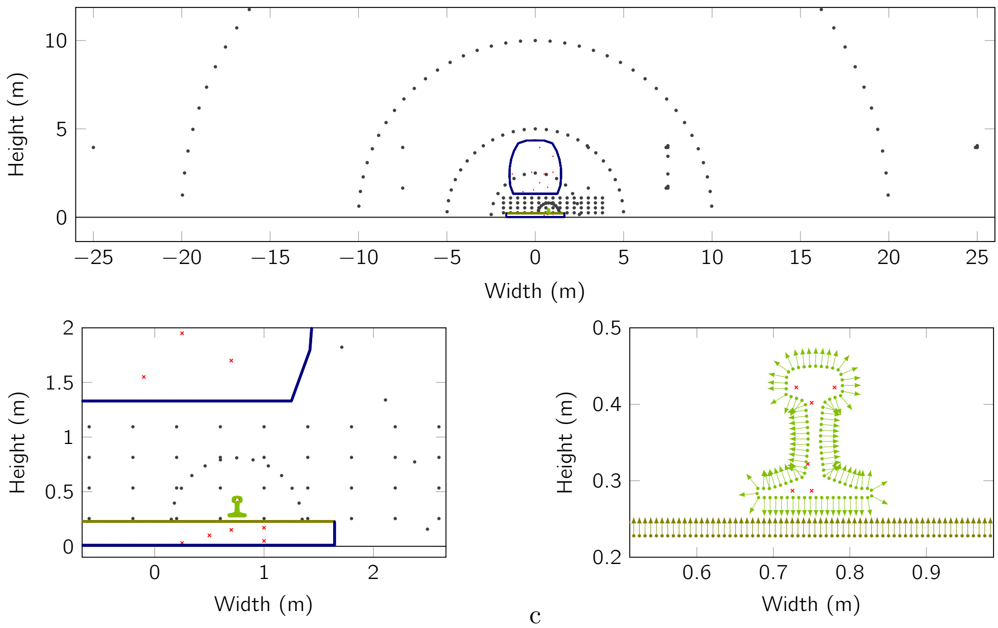

Figure 5.16: Setup (iv) for which the acoustic transfer functions were evaluated.

6 elements per wavelength up to 7.5 kHz. Figure 5.16c shows the surface normal direction for each active surface node on the rail and on the surface below.

A total of 21 CHIEF-points are distributed in the rail-, the track- and the train-cross section. Chief points are marked with a red 'X'. The black dots represent receiver positions or 'field points'. In addition to the pass-by measurement positions defined in the standard ISO 3095, four half-circles of points around the track centre with radii 2.5 m, 5 m, 10 m and 20 m and one half-circle with radius 1.2 m centred at the rail. Additional points are included depending on the geometry. More detailed information can be found in the online resources [174, 175].

5.5.2 Presentation and analysis of the acoustic transfer functions for a rail in free space

The precalculated transfer functions describe the sound pressure created by each source element on all surface and field nodes, for wavenumber $\kappa_0 = 10^{-6}$ rad/m and a frequency spectrum with 1 Hz resolution up to 7.5 kHz. As an example, the transfer functions corresponding to geometry (a) are investigated in the following, focussing specifically on the transfer functions from the 92 source nodes on the rail surface to 100 receiver points located in a circle with 20 m radius around the rail. The data is three-dimensional (92 x 100 x n_f), where n_f is the number of frequency lines in the precalculated spectrum. Figure 5.17 demonstrates how the transfer functions are visualised in the following. Each

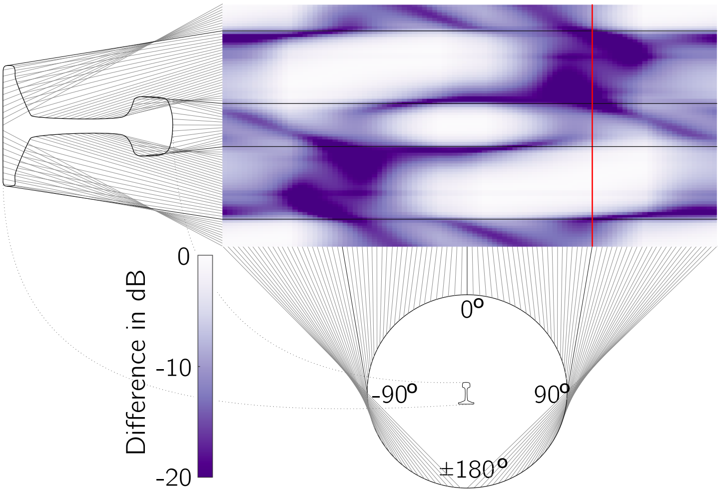

Figure 5.17: Transfer function magnitude between each source element on the rail and receiver point in a circle with 20 m radius around the the rail. The displayed transfer functions are calculated at 1100 Hz, which is typically close to the pinned-pinned frequency.

row in the surface plot describes the contribution of a unit normal velocity at one source node to all receiver points. The position of the source nodes on the rail surface is indicated by the grey lines. Analogously, the position of the receivers is indicated by the grey lines below the 2D plot. The colour range is adjusted to cover a 20 dB sound pressure level range, normalized with the largest sound pressure level at any receiver node at that frequency. In the selected example, a diagonal trend is visible, indicating that in general, a surface velocity on the left side of the rail contributes mainly to the receiver points on its left side, and so on. At the vertical line marking 90 °, the radiation is almost entirely dominated by the right side of the rail. Large parts of the rail surface, with the exception of the rail foot and the part below the rail head, contribute to the sound pressure in vertical direction.

Figure 5.18 shows identical 2D plots, using the same colour scale and dynamic range, for five other frequencies. A distinct interference pattern is visible. Note that the pattern

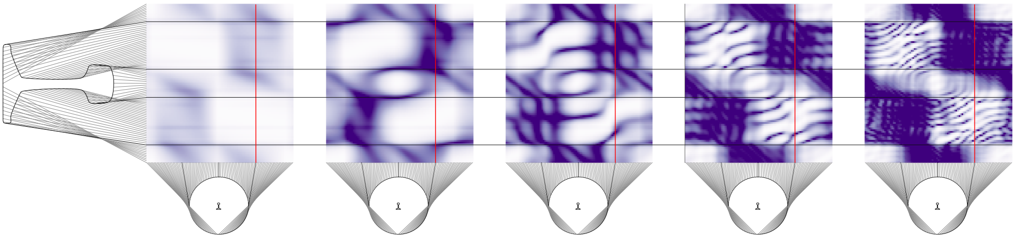

Figure 5.18: Transfer function from surface velocity on each individual node on the rail surface (y-axis) to the sound pressure in a circle around the rail (x-axis), displayed as the relative difference to the largest contribution, in dB. Left to right: 500 Hz, 1000 Hz, 2000 Hz, 4000 Hz, and 7500 Hz. The receiver angle zero degrees corresponds to a position vertically above the rail and increasing numbers indicate clockwise rotation.

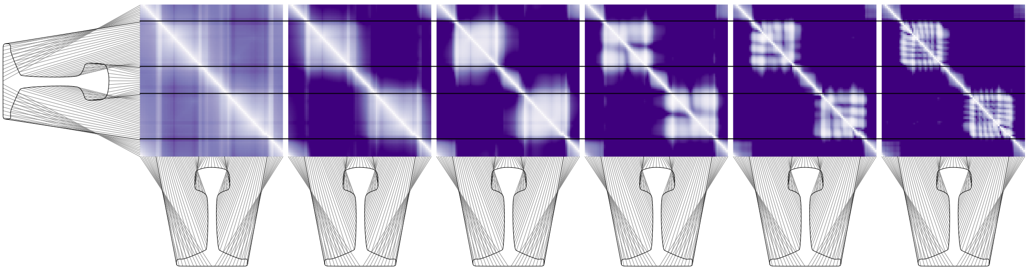

Figure 5.19: Transfer function from the velocity at each individual surface node (y-axis) to the sound pressure at each surface nodes (x-axis), displayed as the relative difference to the largest contribution, in dB. Left to right: 25 Hz, 500 Hz, 1000 Hz, 2000 Hz, 4000 Hz, and 7500 Hz.

does not arise from the interaction of several sources but instead from the wave field created by a single source and the reflections on the acoustically hard rail surface. Below 500 Hz, the wavelength in air is large compared to the dimensions of the rail. Therefore, the rail geometry does not significantly influence the radiation pattern, and the transfer function of all surface nodes to all receiver points is similar, i.e., the dynamic range of the 2D plot is low. With increasing frequency, the geometry of the rail becomes more influential and the dynamic range gets larger. Distinct squares are visible at locations corresponding to the side of the rail. This can be interpreted such that a vibration in any part of this concave rail section focusses the radiation towards lateral receiver positions. A lateral bending wave would thus produce a dipole-characteristic, in which each lobe is produced by the vibration on the corresponding side of the rail.

A comparable analysis is carried out using the rail surface nodes themselves as the receiver points. This is shown in Figure 5.19. The source node is expectedly the main contributor to the sound pressure at its position (thus the diagonal line). A surface velocity in the concave section produces comparatively high pressure at other nodes in the concave section. Again, a frequency dependent interference pattern can be observed.

5.6 3D sound field produced by a harmonic force on a ballasted track

This section presents the sound pressure radiated by a discretely supported rail under harmonic excitation. After the description of the model setup, the sound field around the track is analysed separately for the rail and the sleepers.

5.6.1 Description of the modelling parameters

A WFE-based UIC 60 rail (shown in Figure 3.2) is coupled to a slab track with booted sleepers. In total, 119 sleepers, with a spacing of 0.6 m and a surface area of 66 cm x 30 cm each, are connected to the rail. Slab vibration is neglected here. Each rail support is modelled as a simple spring-mass-spring system with a boot stiffness of 75 kN/mm, a sleeper mass of 150 kg, and a rail pad stiffness of 300 kN/mm. Laterally, the rail is connected to spring-mass-spring systems in which the spring stiffnesses are set to 10 % of the vertical stiffness. The rail is excited with a unit force at mid-span at the centre of the rail head. A small, lateral component is included to demonstrate the effect of exciting non-symmetric and lateral waves. The sound radiation is calculated using the precalculated transfer functions of setup (iii) of Section 5.5, which means that the train hull is excluded.

5.6.2 Sound radiation from a discretely supported rail

Figure 5.20 shows the deflection of the rail head, at one time instance, in black. The sound pressure level (L_p) produced at the standard position, measured along the track, is shown in green. Note that the varying scale on the vertical axis, which is necessary to account for the large dynamic range of both quantities. Here, the sound pressure level is limited to 15 dB intervals in all figures.

At low frequencies, the deflection of the rail consists only of a near field that is visible, i.e. the waves decay close to the excitation position. Consequently, the sound pressure is highest close to the excitation point. The sound pressure level is low compared to the sound radiated by the sleepers or to the rail at higher frequencies.

The vertical resonance frequency of the sleepers is located between 100 Hz and 150 Hz, which leads to a deflection of the rail over a larger distance. However, the sound radiated by the rail is still limited to the excitation position. This is the case up to the cut-on frequency for vertical bending waves at about 460 Hz. At 500 Hz, the rail deflection shows a propagating, decaying wave with a near field at the excitation position. The sound pressure is a result of both the near field, visible as a maximum at the excitation position, and the propagating bending waves, visible as maxima at about ±2.5 m. Sound radiation

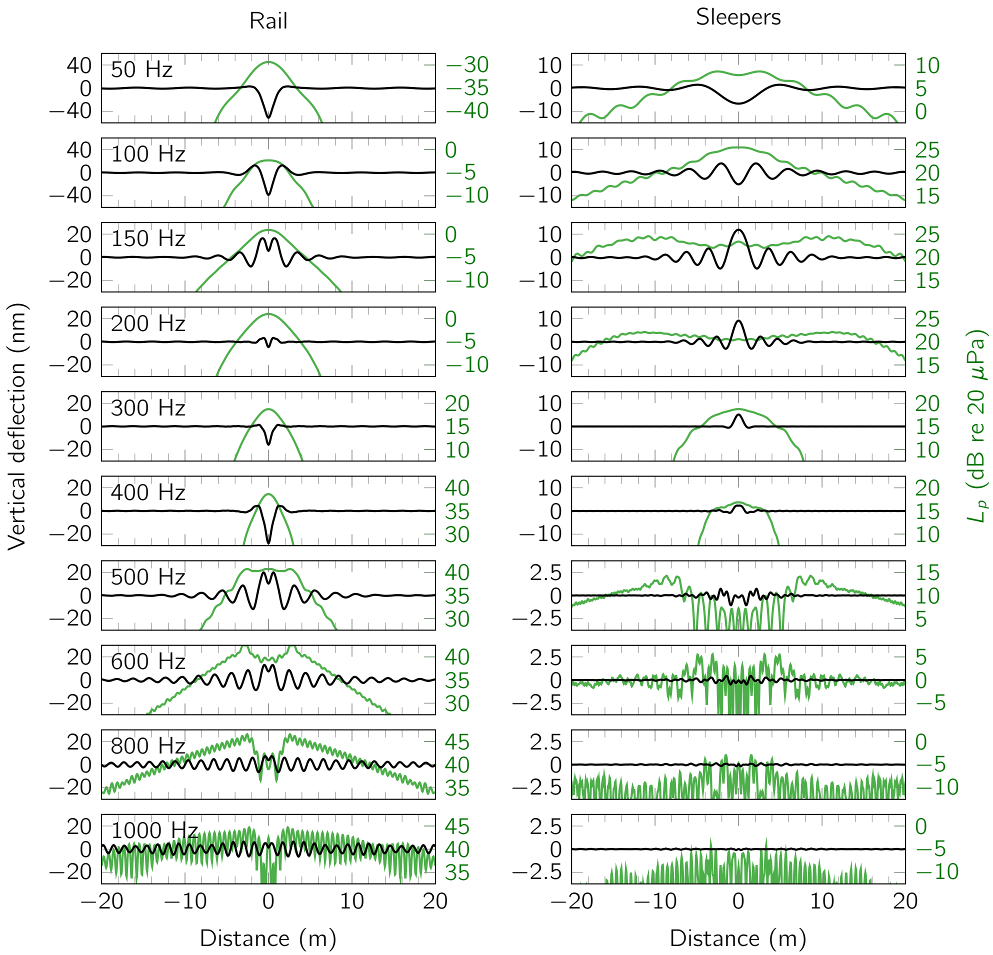

Figure 5.20: Rail and sleeper vertical deflection and sound pressure level measured in the (7.5 m, 1.2 m) standard position, along the track.

from bending waves occurs at an angle β

$$\beta = \arcsin\left(\frac{\kappa}{K}\right), \text{ for } \kappa < K \tag{5.1}$$

between the direction normal to the bending wave propagation and the waves in the air [23]. For higher frequencies, the bending waves produce the highest levels of sound pressure, observable by maxima in distance $\pm x_r$, a few metres from the excitation point. With increasing frequency, the distance of these maxima decreases. This is expected, since the dispersion relation in Figure 3.4 shows that the ratio κ/K decreases with increasing frequency. In the figures at 600 Hz and above, a variation of L_p with a relatively short wavelength is visible. This variation is independent of frequency and has a wavelength of 0.6 m, which suggests that it is the result of discrete support. This may indicate that locations close to rail seats radiate less. Close to the pinned-pinned mode at about 1060 Hz, the decay of the waves in the rail and L_p is low.

The distance x_r can be calculated by the angle β and the lateral distance from the receiver, assuming that the radiation from the bending waves is the strongest at the excitation point. Figure 5.21 shows the wavenumber spectra of the vertical receptance of the rail, where for each frequency the spectrum is normalised according to (5.1). While at 300 Hz, the wavenumber spectrum is relatively flat and, thus, sound is radiated evenly over a wide range of angles, at 750 Hz, the spectrum is dominated by one maximum corresponding to the vertical bending wave. The transition between these two is visible in the wavenumber spectra at 400 Hz and 500 Hz, just below and above the cut-on frequency for vertical bending waves. The distance x_r is indicated on top of Figure 5.21 for the standard measurement position (7.5 m, 1.2 m). In comparison to Figure 5.20, is observed that the distance x_r is, in fact, slightly larger than expected, by about 0.5 m to 1 m. Presumably, the structural near-field impacts the sound radiation close to the excitation position in such a way that the radiation from bending waves dominates only where the near-field has sufficiently decayed.

The sound pressure level in one line captures only the directivity along the track. The directivity in the cross section is explored in Figure 5.22, which shows the sound pressure on a half-cylinder surface around the track, normalised with the largest L_p. The near-field characteristic of the sound field is visible at 100 Hz, 200 Hz and 400 Hz. Especially at 100 Hz, sound is directed horizontally away from the excitation point, which has not been investigated further. At 400 Hz, the sound is predominantly directed upward.

Above the cut-on frequency for vertical bending waves, the described distance x_r is visible. Again, the sound is radiated predominantly in the vertical direction. Close to the pinned-pinned frequency at 1050 Hz, the strong variation of the sound pressure due to the standing wave is visible. For higher frequencies, the dimensions of the rail cross section are in a similar range as the sound waves in air, which means that the cross-sectional directivity is rather complex (see also Section 5.5).

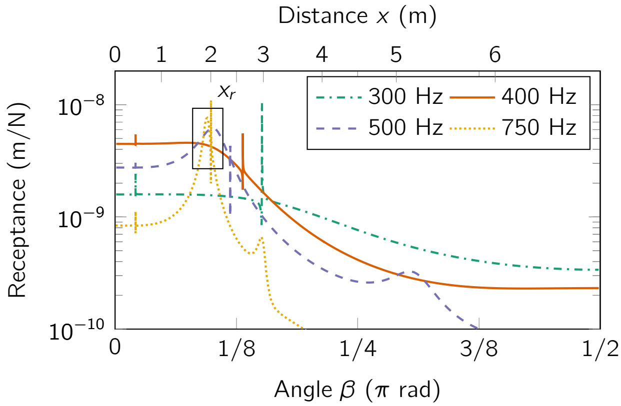

Figure 5.21: The top of rail vertical receptance in wavenumber domain, plotted over the angle β. The frequencies are chosen below, close to, and above the cut-on frequency of vertical bending waves. The sharp peaks at around $\pi/8$ radians, and the other maxima visible for 500 Hz and 750 Hz are an effect of the torsional and lateral bending wave.

5.6.3 Sound radiation from rigid, elastically supported sleepers

Analogously, the right side of Figure 5.20 shows the deflection of the sleepers and the sound pressure level produced at the same line of receiver positions. However, the deflection of the sleepers describes only the acoustically relevant deflection, that is, the deflection of all sleepers is combined in a spectrum in the wavenumber domain that only includes wavenumbers smaller than or equal to the wavenumber in air (cf. Section 3.3.2). Comparing sound pressures, the sleepers produce higher pressure levels than the rail up to about 300 Hz. Around the sleeper resonance at 150 Hz and 200 Hz, the level is fairly uniform over a long section of the track. This is due to two effects, where one is, of course, that the deflection of the sleepers decays only slowly along the rail; the second one is that the velocity profile contains wavenumbers close to the wavenumber in air (cf. Figure 3.17). This is a consequence of the choice of track parameters and dimensions of the sleeper, which leads to efficient sound radiation almost parallel to the track.

Between the sleeper resonance and the cut-on of vertical bending waves, the sound radiation from the sleepers is limited to around the excitation position. With the cut-on of vertical bending waves in the rail above 460 Hz, a wider section of the track radiates; however, the sound pressure is strongly reduced. At 500 Hz and 600 Hz, sound seems to be radiated at an angle. This is a similar effect as observed for the bending wave radiation from the rail. The maximum sound pressure is found around ± 8 m, which corresponds to a radiation angle β of about 0.8 π rad, or about 5.3 rad/m wavenumber of an equivalent bending wavenumber. In comparison to Figure 3.17, this wavenumber is present in the wavenumber spectrum. As it is close to the wavenumber in air, its radiation efficiency is likely high and, therefore, it dominates the sound radiation. At even higher frequencies, the sleepers are almost entirely decoupled from the rail and do not radiate significantly.

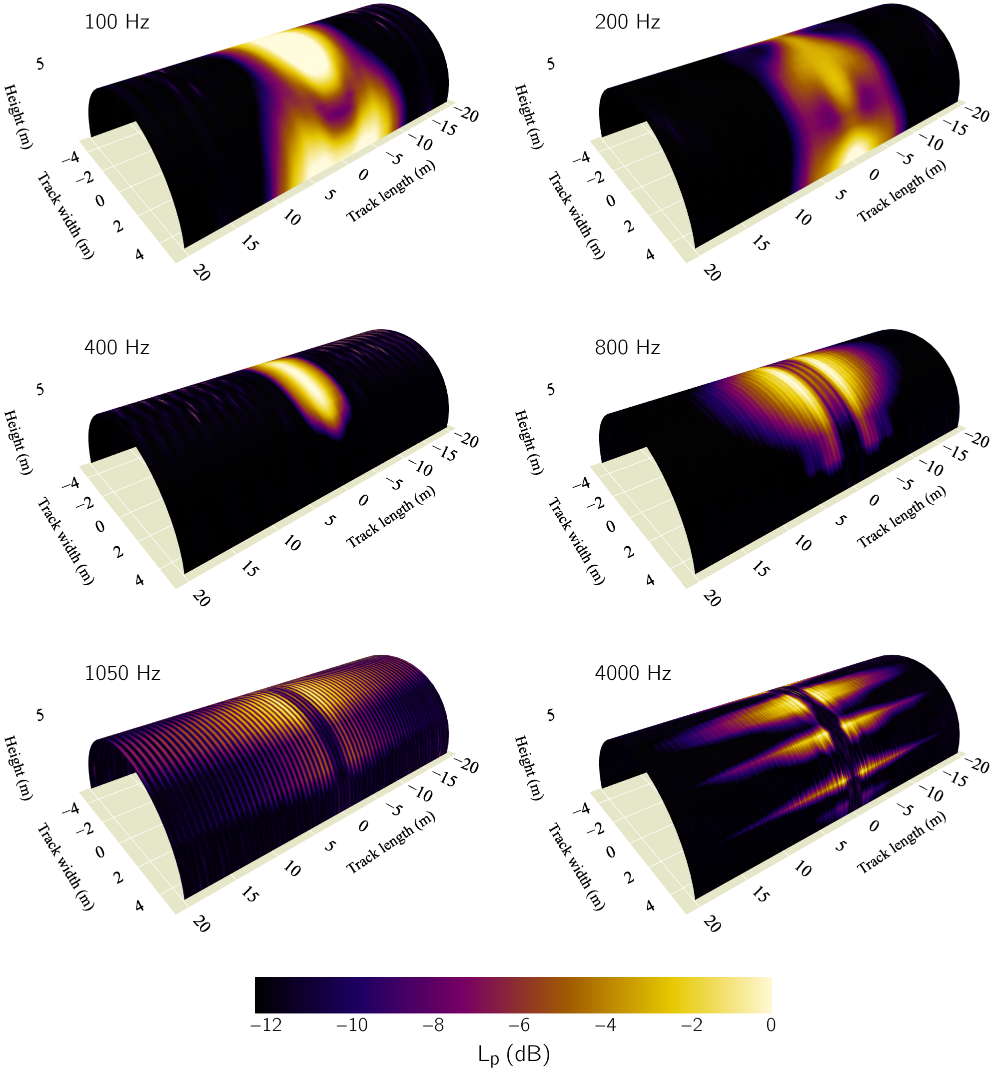

Figure 5.22: Sound pressure level on a 5 m cylinder around the track, created by the vibration of a UIC 60 rail excited with a vertical unit force, mid-span. The sound pressure level is normalized to 0 dB corresponding to the maximum L_p per frequency.

The directivity in the cross section is explored in Figure 5.23. At 100 Hz, no strong variation in directivity is visible around the track. At 150 Hz, the sound pressure is almost constant along a 20 m section of track, as seen in Figure 5.20. The sound directed vertically is focused close to the excitation position, while sound in the horizontal plane is slightly more directed along the track. This is not explored further. At 300 Hz, the sound is focused only on a small section vertically above the excitation point. The effect of individual sleepers becomes visible at 500 Hz, since here, the wavelength in air is close to the distance between the sleepers, and thus interference from individual sleepers can occur (cf. Figure 3.18). The discussed effect that sound is radiated at an angle, similar to radiation from bending waves, is clearly visible at 500 Hz.

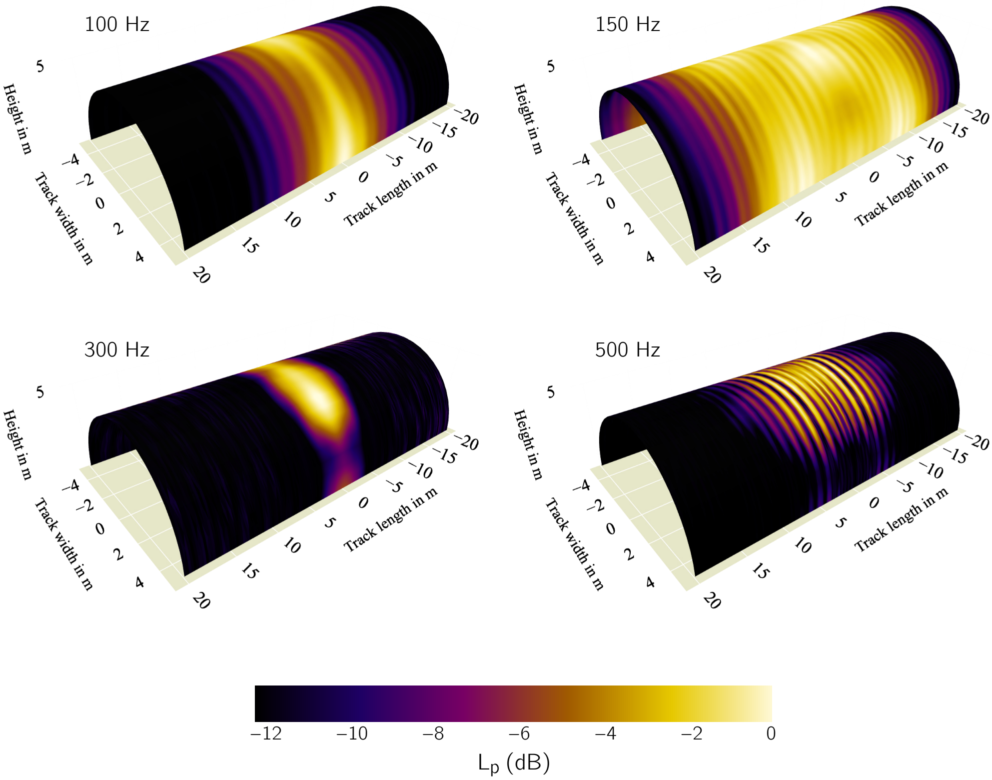

Figure 5.23: Sound pressure level on a 5 m cylinder around the track, created by the vibration of a series of 119 sleepers, coupled through a UIC 60 rail, which is excited with a vertical unit force, mid-span. The sound pressure level is normalized to 0 dB corresponding to the maximum L_p per frequency.

5.7 The influence of the dynamic track model on the predicted sound field

Section 3.2 presents an approach that allows the efficient prediction of the sound field created by railway track vibrations. The approach is based on the pre-calculation of acoustic transfer functions using the wavenumber-domain Boundary Element method (WBEM). To predict the sound pressure at a point, these acoustic transfer functions are first scaled with the vibration of the structure and then added. The vibration of the structure can in turn be predicted in different modelling approaches. The consequences of the choice of the modelling approach for the rail dynamics on the predicted sound field are investigated in the following. Investigating the limitations of different rail models is relevant when the developed approach is combined with simpler rail models.

5.7.1 Modelling approaches for the track vibration

The high frequency dynamic response of the rail can be predicted with analytical or numerical modelling approaches. Furthermore, the rail support can be modelled in different ways. Here, six different combinations of rail models and support types are compared, visualised in Figure 5.24. The track setups are labelled R1 to R6. While models R1 and R2 feature a rail model based on Euler-Bernoulli beam theory, the rail in track R3 is modelled using Timoshenko beam theory, and R4 to R6 use a numerical modelling approach, the Waveguide Finite Element Method (WFEM). The models employing beam models consider only the vertical vibration of the rail, excited by a harmonic force. There is the possibility of including a second beam for the lateral vibration and making assumptions about their relative amplitudes, but this is not considered here. The rail and support parameters are identical for each support type, as visible in *Paper D*, Table 1. As the WFEM-based approach to modelling the high frequency vibration response of the rail showed good agreement with the measurement in Section 5.1, it is used here as a reference.

The dynamic properties of each track are compared in terms of its vertical point receptance (see Paper **D** for details). It is observed that the models based on Euler-Bernoulli beam theory diverge from the numerical models around 1.5 kHz. The Timoshenko-beam model aligns with the WFE model up to just over 4 kHz. Note that the comparison is made only for a symmetric excitation of the WFE rail, meaning no lateral or torsional waves are excited.

5.7.2 Comparison of the acoustic performance of the different dynamic track models

The generated sound field of each track model have been compared with the reference model in different ways. The radiation ratio, calculated as the radiated sound power divided by the averaged squared surface velocity and the impedance of a plane wave, describes

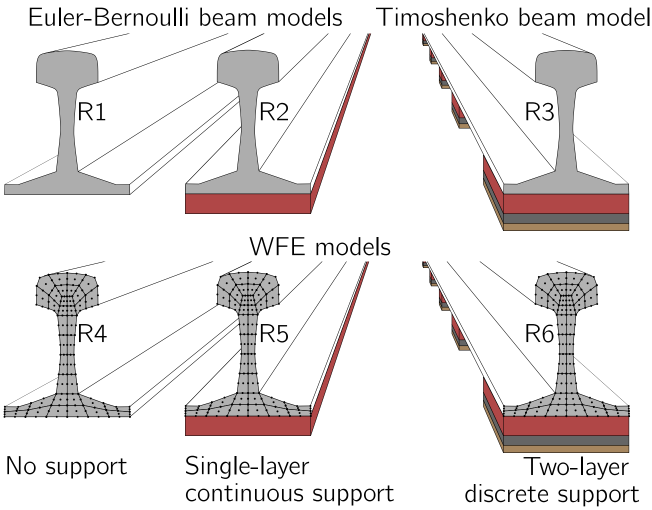

Figure 5.24: Considered track models included in the study.

the efficiency with which the structure radiates sound. This quantity is predominantly a descriptor of the acoustic geometry. As this geometry is included in the precalculated transfer functions, it is identical in all cases and the radiation ratio is very similar in all cases.

Figure 5.25 shows the difference in radiated sound power between the WFE rail to the respective beam models. A negative difference indicates that the WFE-based rail radiates more sound power. Since the excitation of the rail is rarely perfectly symmetric, a second off-centre excitation on the rail head was included in a separate calculation, exciting the rail vertically at a node about 1 cm off-centre toward the centre of the track. The grey boxes in each plot indicate a 3 dB margin.

The track R1 produces a sound power that is within 3 dB difference compared to R4 up to about 2 kHz. The excitation position does not make a large difference in this case. The track R2 produces a sound power comparable to the track R5 up to about 4 kHz for the symmetric excitation, and 3.15 kHz for the asymmetric excitation. However, there is also a significant difference below 125 Hz, which is likely due to the excitation of the lateral bending wave, which is not included in model R2. Track R3 aligns well up to 5 kHz with the track R6 when excited centrally. As above, a difference below 100 Hz is observed, likely due to the lateral bending wave.

In terms of the track-side sound pressure, simple beam models can provide similar results only up to 2.5 kHz. Euler-Bernoulli beams seem unfit for time-domain predictions of the radiated noise, as they overestimate the bending wave speed at high frequencies. The results also show that the standard track decay rate and the acoustic sound pressure decay along the track are comparable.

The directivity of a single rail in free space is evaluated by calculating the sound pressure

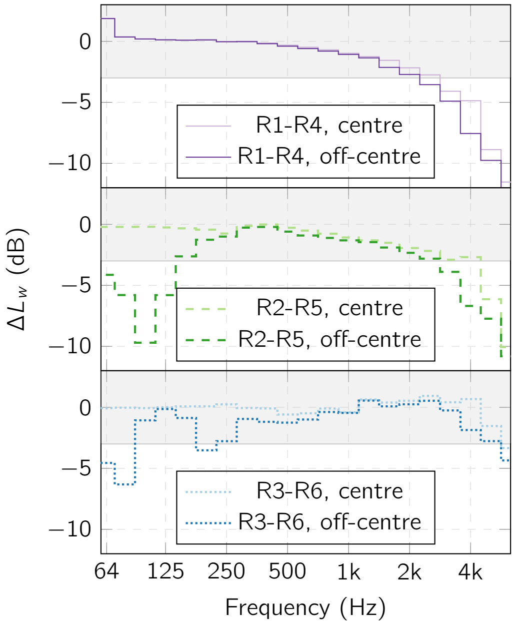

Figure 5.25: Difference between predicted radiated sound power of the beam models to the WFE model, per support type.

in a semi-circle around the rail, as shown in Figure 5.26. The receiver points in the lower half of the semicircle might be of limited use in practice but are included for demonstration. The semicircle has a radius of 20 m. Longitudinally, the sound pressure is evaluated in the same plane as the excitation.

The track models R3 and R6 are compared in Figure 5.26. As above, negative values correspond to an under-prediction of the beam model. While for a symmetric excitation on the WFE rail head the directivity is predicted with only a very small difference, the off-centre excitation position produces a significant difference, especially in the horizontal plane below 250 Hz. Towards high frequencies, both excitation positions show differences larger than 10 dB above 5 kHz. Furthermore, for the off-centre excitation position, the sound pressure is no longer well predicted in several directions above 2 kHz.

The directivity is also evaluated in the horizontal plane, in a line parallel to the track, corresponding to the standard measurement position 7.5 m from the track centre and 1.2 m above the top of the rail. Figure 5.27 shows the location of this line.

The sound pressure level produced by a harmonic excitation at x_0 is shown in Figure 5.28. The level of each 1/3 octave band is normalised to the level at x_0, to highlight the decay over distance. There is a prominent dip at 250 Hz in all figures, which corresponds to the vertical resonance of the rail on the support. Around this frequency, the support effectively absorbs the vibrations in the rail. Below this frequency, the sound pressure level is similar for the continuously supported rails on the left and the discretely supported

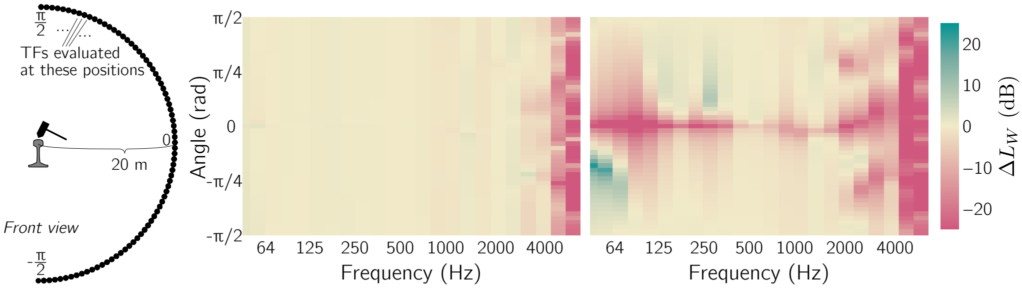

Figure 5.26: Difference of the sound pressure level at the half-circle of receiver points described on the left. Central image: central excitation on the rail head, right image: off-centre excitation.

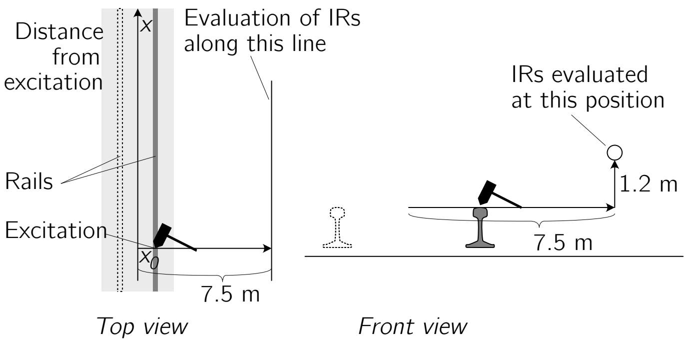

Figure 5.27: Location at which the impulse responses are evaluated.

rails on the right. Above this frequency, the largest sound pressure level is not found at the excitation position but instead at a frequency-dependent distance. This distance is due to the fact that sound radiation from bending waves occurs at an angle. This angle depends on the relationship between the bending wavelength and the wavelength in the air, which makes it frequency dependent.

This effect is only visible from 250 Hz since here, vertical bending waves start to propagate in the rail. At the high end of the considered frequency spectrum, the WFE-based models show a more complex radiation pattern compared to the beam models, indicating that the radiation from multiple wave types interferes at the receiver positions. Although the absorbing effect of the rail support is present over a wide frequency range for continuously supported tracks, discretely supported tracks do not show a large decay above about 400 Hz. As the wavelength of the bending wave decreases compared to the spacing of the rail seats, their efficiency of damping these vibrations decreases, until ultimately the wavelength matches the rail seat spacing at the pinned-pinned mode at 1070 Hz.

This effect, created by the radiation from bending waves, is even more visible when the support is not present, as for example on track R4. Figure 5.29 visualizes this frequency-distance dependency clearly above 50 Hz. While in the cases above, this effect was only

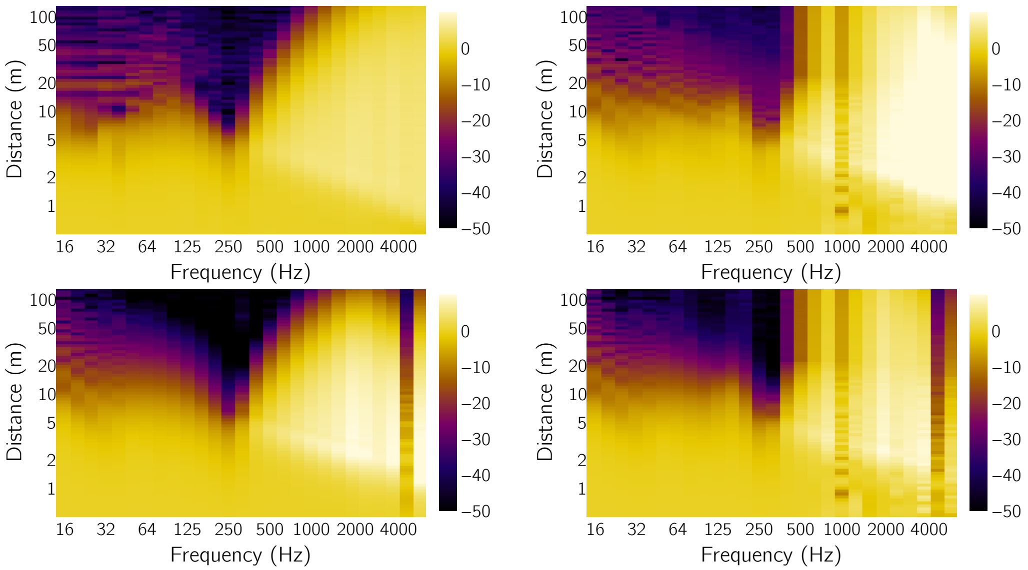

Figure 5.28: Decay of the sound pressure in a line along the track. Top: Beam models R2 and R3, bottom: WFE models R5 and R6. Each third octave band level is normalised to the level at 0 m.

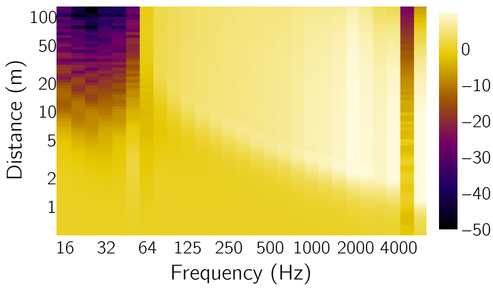

Figure 5.29: Decay of the sound pressure produced by a WFE-based rail that is acoustically free in space. Each third octave band level is normalised to the level at 0 m.

visible above 250 Hz because no bending waves existed in the structure, here the lower bound is set by the critical frequency of the bending waves. Below 50 Hz, the wavelength in the structure is shorter than wavelength in air, so the rail only radiates an acoustic near field and no sound power.

Impulse responses can be generated from these spectra by inverse Fourier transform. Figure 5.30 presents impulse responses generated at 1 m and 64 m longitudinal position along the rail and compares the analytical model with the numerical model of each type of support. Two features are noteworthy: Firstly, the decay of the numerical models is longer

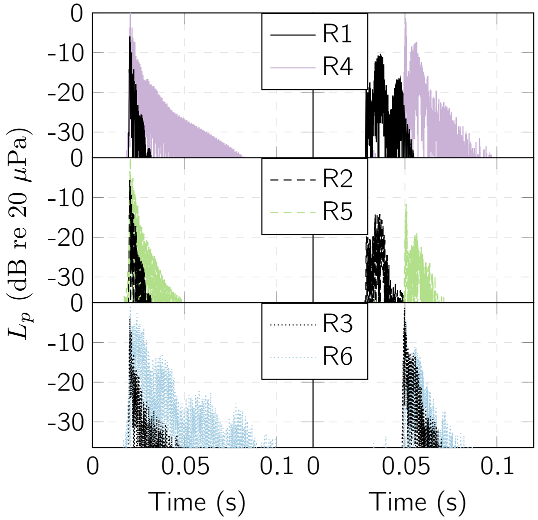

Figure 5.30: Comparison of the pressure impulse responses at 1 m and 64 m for different track models.

and contains several different slopes. This indicates the decay of different types of waves in the rail. Secondly, the impulse responses calculated at 64 m with the Euler-Bernoulli beams show that the first peak arrives earlier than those of the Timoshenko-beam and numerical models. This is likely due to the inherent approximations of the Euler-Bernoulli beam theory, leading to an overestimation of the wave speed at higher frequencies. The track support does not seem to influence the timing of the first wave front but instead shapes the decay of the impulse responses, having an uneven effect on the different wave types. Several other descriptors of the sound field, both in the frequency and in the time domain, are compared in *Paper D*.

Finally, the pass-by of a force on a the track setup R6 is simulated in time domain using the in-house software WERAN [61]. The vehicle speed is 100 km/h and the roughness profiles are based on measurements [169]. The total length of the pass-by is 3 s corresponding to about 81 m. The sound pressure in a stationary microphone position is calculated as described in Section 3.4. Figure 5.31 shows the spectrogram of the resulting sound pressure. The frequency range between about 200 Hz and 1000 Hz dominates the sound

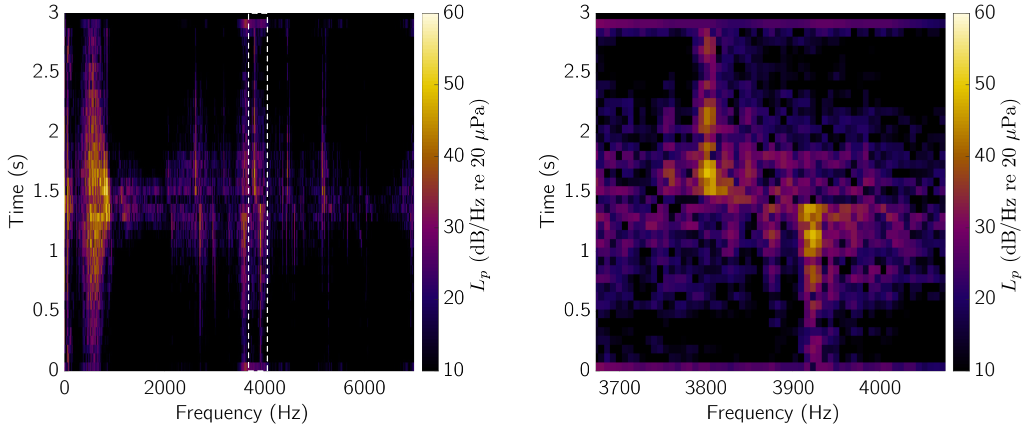

Figure 5.31: Spectrogram of the generated pressure signal at a stationary microphone during the pass-by of a moving force.

pressure, but some distinct frequency components can be found up to 5 kHz. These are likely related to dynamic resonances in the wheel or the track. Figure 22 shows one of these frequency lines and shows the effect of the Doppler shift during the pass-by. From the observed frequency shift just larger than 100 Hz and the known vehicle speed of 100 km/h, the corresponding sound speed c_p is found to be about 1750 m/s, which matches the expected phase speed of vertical bending waves in a free rail.

5.8 The structural vibrations of a railway wheel

A method for calculating the dynamic response of a railway wheel based on the curved WFEM is established in Section 4.1. This method is used here to analyse the dynamic properties of a wheel of type BA093, which is used in the noise measurement car (SMW) of DB Systemtechnik (also described in [176]). The approximate geometry of this wheel, with a medium worn profile, is shown in Figure 5.32. The flexibility of the axle is neglected and a rigid boundary condition is applied at the hub of the wheel.

An analysis of the eigenfrequencies of this wheel reveals 78 eigenfrequencies below 10 kHz with up to 13 nodal diameters. The corresponding modes are classified into axial, radial, and circumferential modes as presented in Figure 5.33. Axial modes with up to five nodal circles are found in this frequency range. The lowest eigenfrequency is found at 160 Hz belonging to the mode (1,0,a).

Its mode shape, along with five other selected mode shapes, is presented in Figure 5.34. The eigenfrequencies and classification of each mode shape is indicated with the letters **a** to **f** in Figure 5.33. Due to the asymmetry of the wheel, there is no pure radial or axial motion. For example, while the radial deflection in mode (3,0,r) (Figure d) dominates the mode shape, there is still an axial deflection observable on the wheel web. Likewise, mode

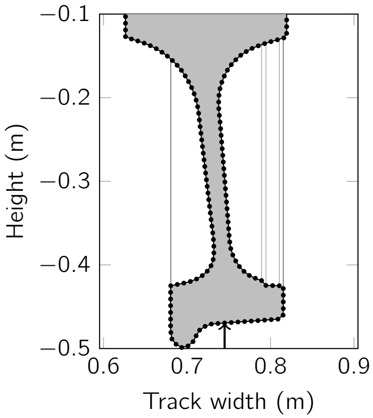

Figure 5.32: Lower part of the wheel cross-section, where the centre axis of the wheel is located at 0 m height. The arrow indicates the assumed contact location.

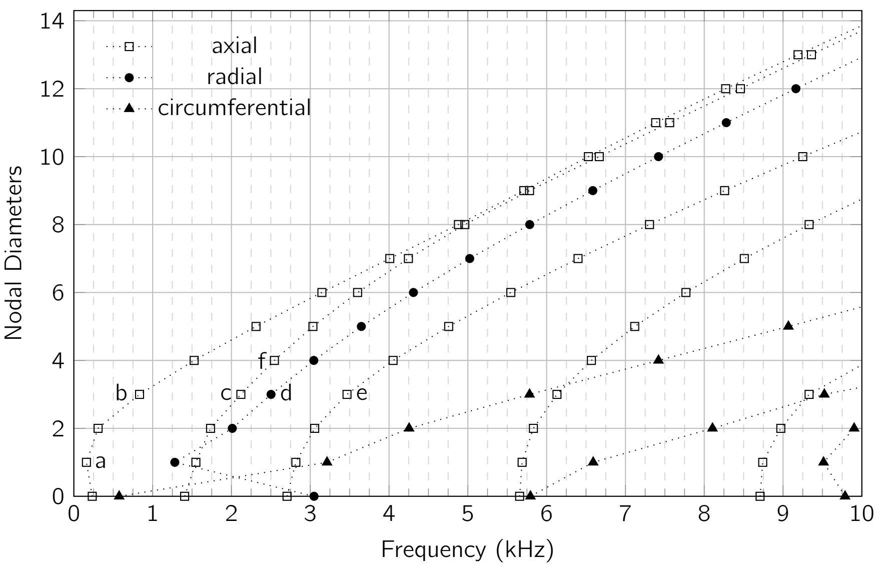

Figure 5.33: Dispersion relation of the eigenfrequencies of the wheel.

(3,1,a) (Figure c) predominantly moves in the axial direction, but a radial component is visible on the wheel web. This means that a vertical force will lead to axial motion, which efficiently radiates sound, as will be discussed in more detail in Section 5.10.

The driving point mobility at the contact point can be determined by modal superposition. Structural damping is included via a damping ratio depending on the number of nodal diameters as suggested in [23]. Figures 5.35 to 5.37 show the predicted point mobilities in the radial and axial directions, as well as cross-mobility. Figure 5.35 shows that radial

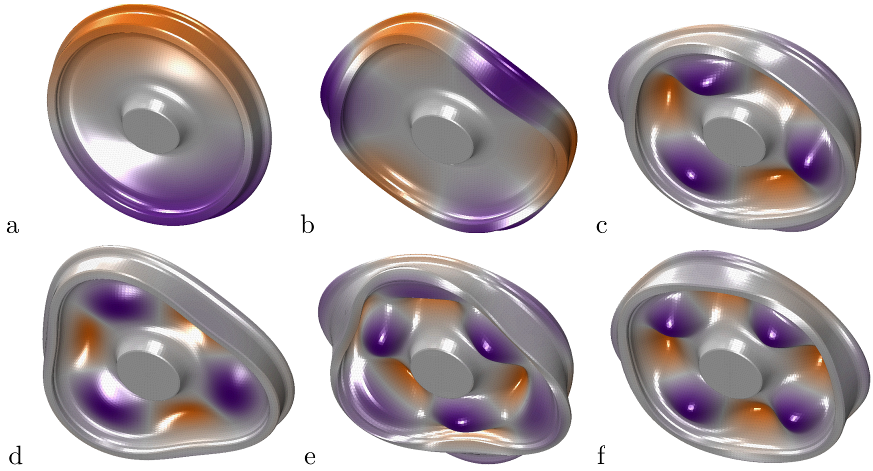

Figure 5.34: Vibrational mode shapes of the wheel. a) (1,0,a), b) (3,0,a), c) (3,1,a), d) (3,0,r), e) (3,2,a), f) (4,1,a). The colour indicates axial deflection.

mobility is mostly determined by radial modes, whose eigenfrequencies are indicated by dotted lines. However, axial modes contribute to mobility, especially at low frequencies.

The axial contact point mobility in Figure 5.36 is in large parts determined by the axial modes with zero nodal circles, up to about 5.5 kHz or 8 nodal diameters. The cross-mobility in Figure 5.37 describes the radial response to an axial excitation and vice versa. In general, there is a comparatively strong coupling between both directions at the eigenfrequencies of the radial modes. The consequences of this coupling on the sound radiation from the wheel are discussed below.

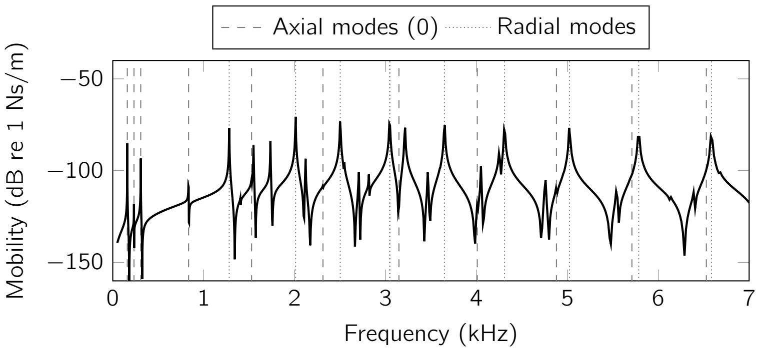

Figure 5.35: Radial input mobility of the wheel. The eigenfrequencies of radial modes and axial modes with zero nodal circles are indicated by vertical lines.

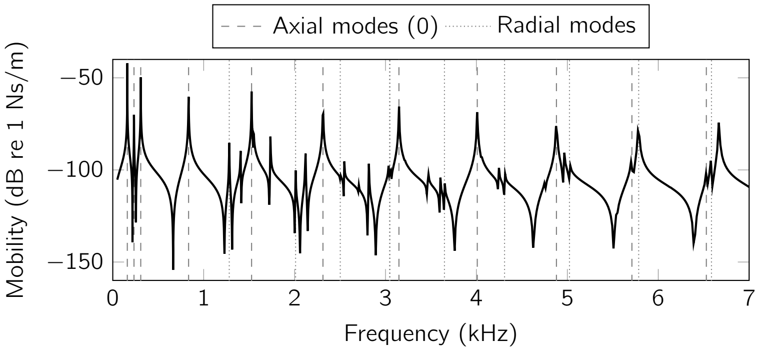

Figure 5.36: Axial input mobility of the wheel. The eigenfrequencies of radial modes and axial modes with zero nodal circles are indicated by vertical lines.

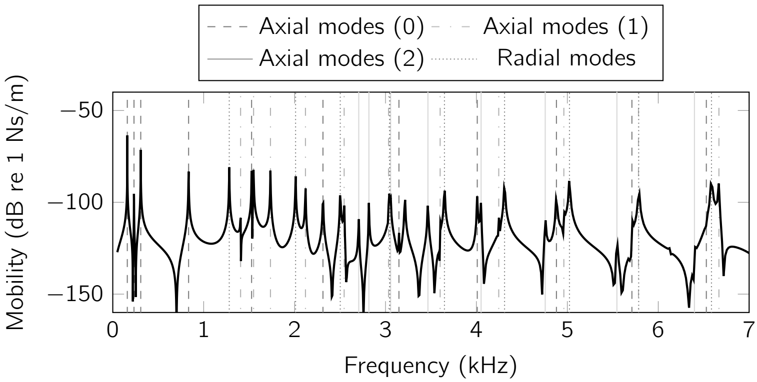

Figure 5.37: Vertical to lateral cross-mobility of the contact position. The eigenfrequencies of radial modes and axial modes with zero, one and two nodal circles are indicated by vertical lines.

5.9 Validity of a simplified half-space approximation for radiation from railway wheels

Models of sound radiation from railway wheels often assume that the wheel is placed in an acoustic free field. This approximation simplifies the calculation, since the sound field can then be expressed in a cylindrical coordinate system and an adapted Boundary Element method can be used efficiently. Further, the exact acoustic geometry around the wheel is often quite complex, including the wheel suspension, bogie, vehicle body and the possibly absorptive track surface. Here, the focus is on the effect of the track surface only. Slab tracks feature a hard concrete top layer instead of porous ballast. This acoustically reflective surface layer can impact the radiation efficiency of the wheel, which is investigated in the following.

The used wheel geometry is of type BA093, identical to the wheel in Section 5.8 above. The dynamic response of the wheel is solved using the curved WFE method, which generates a description of the cross-sectional mode shapes of the wheel for each number of nodal diameters n. The modal superposition of the mode shapes is used to calculate the dynamic response of the wheel to a harmonic force input.

The radiation ratio

$$\sigma = \frac{W_{\mathrm{rad}}}{\rho_0 c_0 S \langle \overline{v^2} \rangle} \tag{5.2}$$

measures the efficiency with which a vibrating structure radiates sound by normalising the radiated sound power W_{rad} by the plane wave impedance $\rho_0 c_0$, the radiating surface S and the temporally and spatially averaged squared surface normal velocity v. Thompson and Jones [44] show that the radiation ratio σ of the wheel modes with different numbers of nodal diameters, for low frequencies, follows the function f^{2n+2} for the radial modes and f^{2n+4} for the axial modes. Figure 5.38 shows the radiation ratio for different numbers

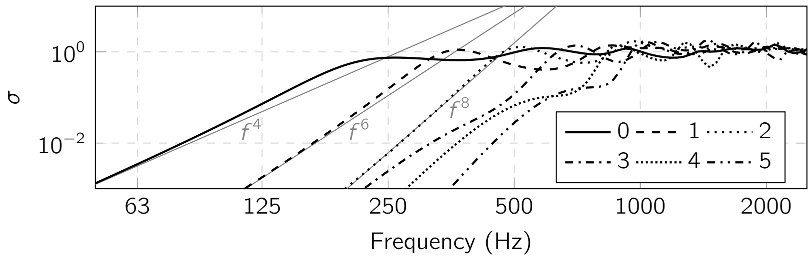

Figure 5.38: Radiation ratio σ of the wheel for different numbers of nodal diameters and radial excitation at the contact point. The slopes of the functions proportional to f^4, f^6, and f^8 are included as a reference.

of nodal diameters, for a radial excitation at the contact point. The cross-sectional modes corresponding to each number of nodal diameters have been added via modal superposition. It is visible that despite the radial excitation, the radiation ratio follows the function f^{2n+4} associated with axial modes, at least up to $n = 2$. Due to the asymmetry of the wheel profile, axial modes are excited by the radial force and dominate the radiated sound power. For higher n the slope, just before reaching $\sigma = 1$, follows the function f^{2n+2} associated with radial modes.

The effect of introducing a reflective plane is analysed in Figure 5.39 by changing the height of the wheel above the plane. Here, the radiation ratio includes all nodal diameters. A radial point force excites the wheel at the contact point. It is visible that, despite a relatively large variation in the height of the wheel above the plane, the effect on the radiation ratio is not significant above about 200 Hz. At this frequency, the radiation ratio is below 0.01 and decreases towards lower frequencies. It can be concluded that the overall effect of the reflecting plane on the radiation ratio is small.

A simplified method to include perfectly reflective boundaries is to introduce mirror sources without taking into account the influence of the reflection on the sound radiation.

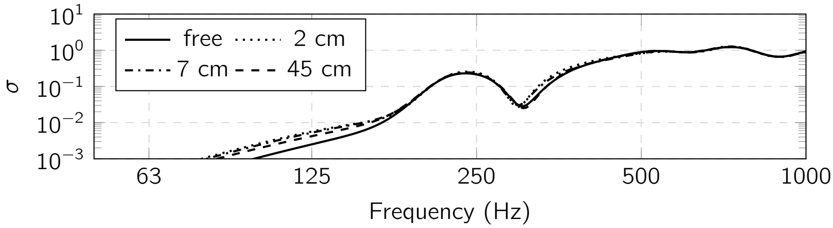

Figure 5.39: Radiation ratio σ for different heights of the reflective plane. The wheel is excited radially in the contact point.

By mirroring the free-field solution at the intended boundary and adding this mirrored field to the original sound field, an approximation of the half-space solution is produced. A benefit of this approximation is that it is comparatively simple to implement, in comparison to the exact solution. This mirror-source approximation is investigated in the following.

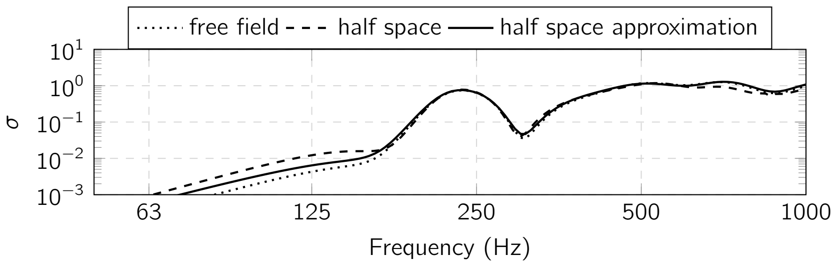

Figure 5.40: Radiation ratios for the radiation into free field and half space, comparing the fully coupled solution to the approximation via mirror sources. The excitation is axial at the contact point.

Figure 5.40 shows the radiation ratio, here for axial excitation, for the coupled half-space and the mirror-source approximation. The free-field solution is included for completeness. In the same way as above, the effect of the reflecting plane is comparatively small, especially in the frequency range in which the radiation ratio is high. Considering this, the mirror-source approximation matches both the half-space solution and the free field solution reasonably well. This means it is not necessary to include the effect of a reflecting track surface on the radiation efficiency of the wheel.

The sound power and the radiation ratio describe the sound field independent of its spatial orientation. The directivity of the wheel can be affected by the reflective plane. Figure 5.41 shows the predicted sound pressure level at three standard positions next to the track, computed for the free field solution, the coupled half-space solution, and the mirror source approximation. The interference of the original sound field with the reflected field at the boundary expectedly creates dips in the half-space solutions. In the frequency range up to 100 Hz, which is not shown in this figure, the mirror source model is an appropriate approximation. Further, it seems that at some resonance frequencies of the wheel, the mirror source model is well aligned with the coupled half-space solution. Otherwise, larger differences are observable.

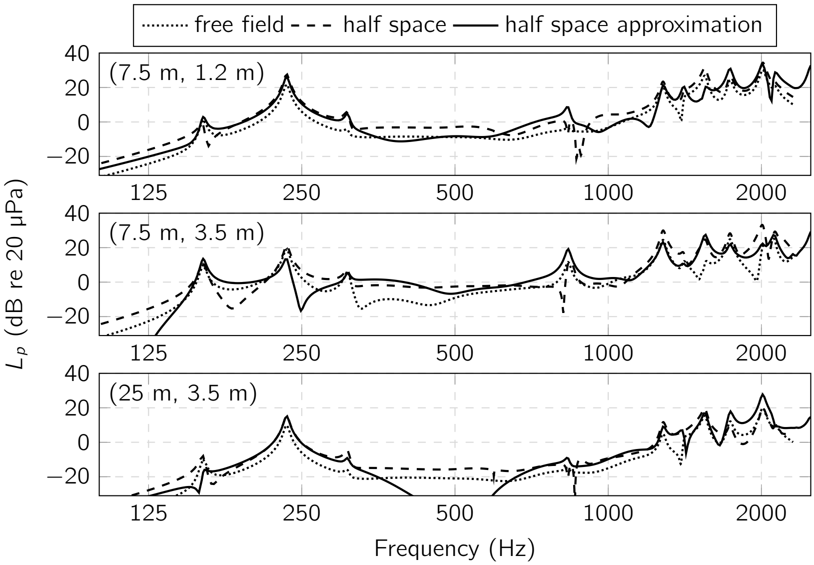

Figure 5.41: Calculated sound pressure level at three standard measurement positions for three different acoustic geometries: the wheel in free space, half-space with a perfectly reflecting boundary, and an approximation of the half-space by adding the mirrored sound field of the free wheel.

Averaging these results in third-octave bands and focussing on the difference between the coupled half-space calculation and the mirror-source approximation allows for a better quantification of the error. Figure 5.42 presents this difference. For the first and third positions, the mirror-source approximation predicts the sound pressure within a few decibels compared to the full solution. For higher frequencies differences exceeding 10 dB are observable. At low frequencies, the free-field solution expectedly produces a 6 dB lower sound pressure at the receiver.

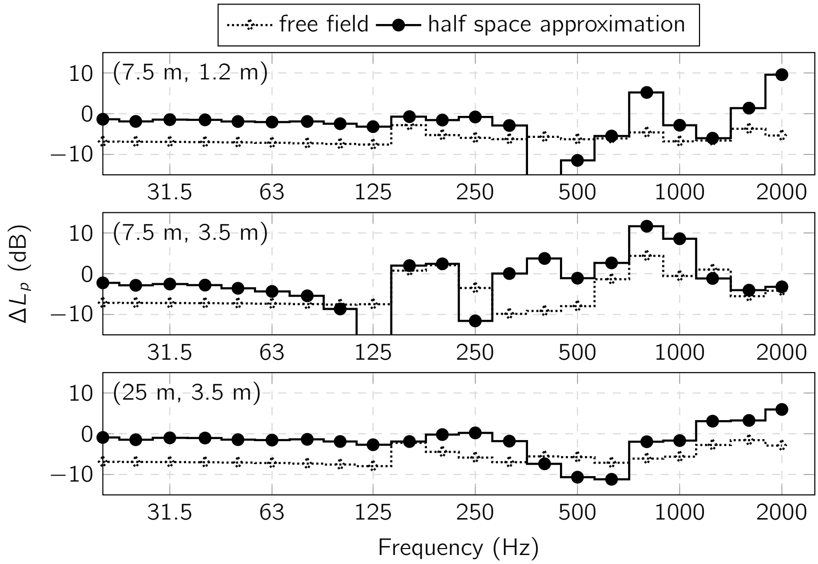

Figure 5.42: Free-field and mirror-source approximation compared to the coupled half-space solution.

5.10 The radiation directivity of wheel modes and their contributions to the pass-by sound pressure

Wheel noise typically dominates total rolling noise above 2 kHz to 4 kHz. Determining which modes dominate the total sound pressure arriving at a stationary microphone during the pass-by of a wheel can help to develop noise mitigation measures on the wheel. Several factors influence this modal contribution:

1. The frequency content in the contact forces, which is as a result of the combined roughness and the dynamic interaction between wheel and rail
2. The excitation position on the wheel tread, which determines how efficiently each mode is excited
3. The transfer function between the mode shape and the microphone position, depending the directivity of the mode and the relative position of the wheel to the microphone

Section 4.3 describes a method that allows calculating the pass-by sound pressure based on a model for the wheel-rail interaction in the time domain, the description of the wheel vibration based on its modes (see also Section 5.8), and transfer functions that describe the sound pressure at the microphone position for each mode. The transfer functions are evaluated with the help of an axisymmetric BE formulation and equivalent sources based on spherical harmonics. The total sound pressure is calculated by adding the contribution of all modes based on their relative amplitudes at each time step.

In the following, examples of the directivity of two wheel modes are analysed. Then, the contribution of each mode to the sound pressure level during a pass-by is analysed for a specific combination of wheel and track.

5.10.1 Directivity of wheel modes

Directivities of the two modes (1,0,a) and (3,1,a) are analysed in Figures 5.43 and 5.44. Their modal patterns are shown in Figures 5.34 a) and c), respectively. Four different perspectives are shown. The wheel visualises the orientation of the sound field. The coloured surface represents the directivity, where the radial distance of each point on the surface indicates the magnitude of the sound radiation in this direction. The colour indicates the relative phase. The magnitude is normalised such that the largest radial distance is one.

Figure 5.43 shows the directivity pattern created by the axial mode with one nodal diameter (1,0,a) at different frequencies. Since the radiation is calculated for a wheel in an acoustic free field, the radiation pattern also has one nodal diameter. At 63 Hz and 250 Hz, the directivity is similar with a quadrupole pattern to the sides of the wheel. The upper and lower lobes on either side of the wheel are out of phase by π rad. With increasing frequency, the radiation pattern becomes more complex, and multiple side-lobes appear. Since the mode shapes are asymmetric with respect to the vertical wheel axis, the resulting radiation pattern can also be asymmetric, which is especially visible at 250 Hz and 1000 Hz.

The directivity of mode (3,1,a) is shown in Figure 5.44. Three nodal diameters are visible. At 63 Hz and 250 Hz, this axial mode has a dominant radial directivity. A possible explanation for this is that since the main axial motion occurs on the wheel hub, areas of large positive and negative axial displacement are close together compared to the wavelength in air. This means that only a near field is radiated in this direction. At higher frequencies, the wavelength becomes smaller than the distance between the areas of large axial displacement, and a clear axial directivity pattern emerges. Again, at high frequencies the geometrical features of the wheel lead to additional side lobes.

5.10.2 Modal contribution to pass-by sound pressure

As an example of how different wheel modes can contribute to the sound pressure level at a stationary microphone position, a simulation of a pass-by of a single wheel is presented below. The roughness of the wheel and rail and their dynamic properties are described in *Paper G*. The method developed in Section 4.3 allows calculating the contribution of each individual wheel mode. These contributions are presented in Figure 5.45.

It is visible that some modes, for example all axial modes with no zero circles, are

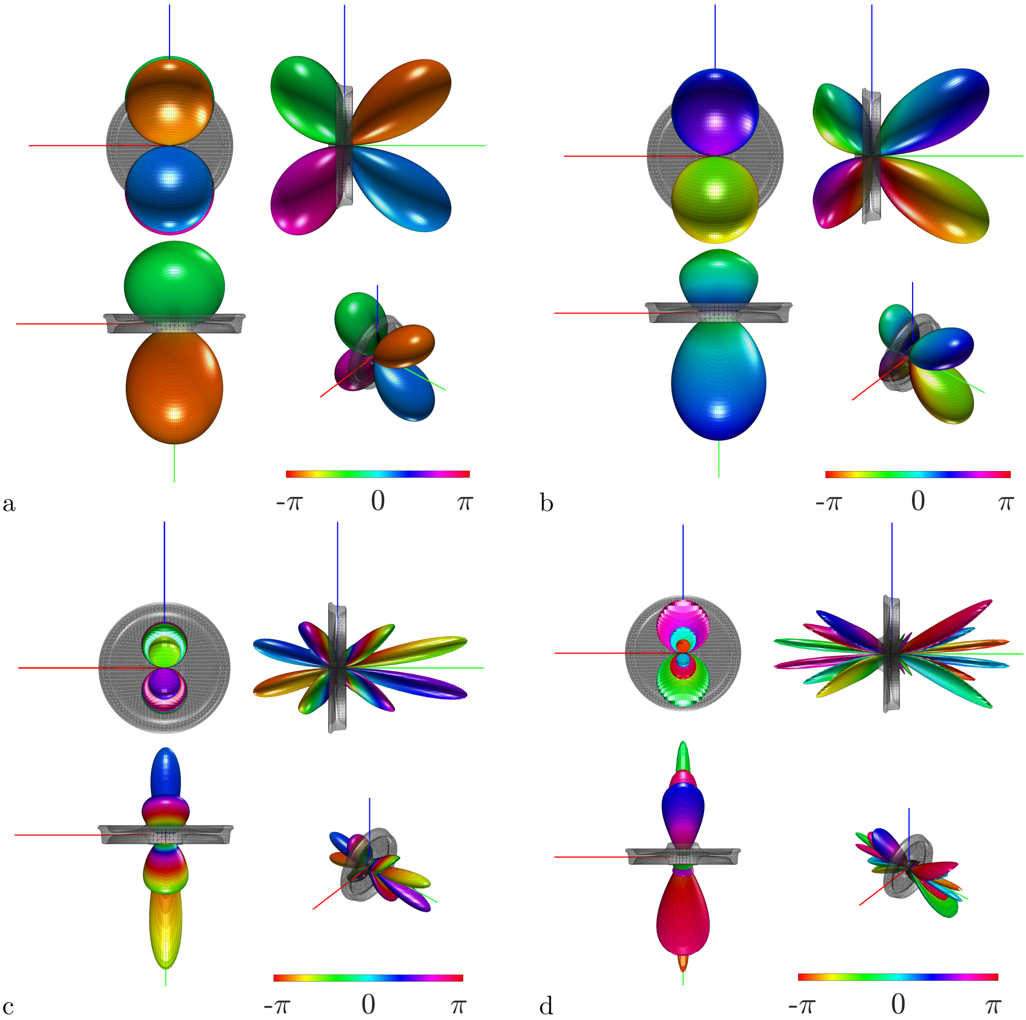

Figure 5.43: Directivity of the axial mode (1,0,a) for (a) 63 Hz, (b) 250 Hz, (c) 1000 Hz, and (d) 4000 Hz.

not relevant to the pass-by signals in this simulation. These could be neglected when predicting total sound pressure. It is clear that some of the modes, because of their directivity, dominate when the wheel is not located directly in front of the microphone (see for example mode (4,1,a)).

In an attempt to quantify and compare the contribution of each mode to the pass-by pressure, an equivalent sound pressure during a 1 s time interval ($L_{\mathrm{p,eq,1s}}$) is calculated. This time interval corresponds to approximately 28 m travelling distance. The wheel passes the microphone in the middle of the interval.

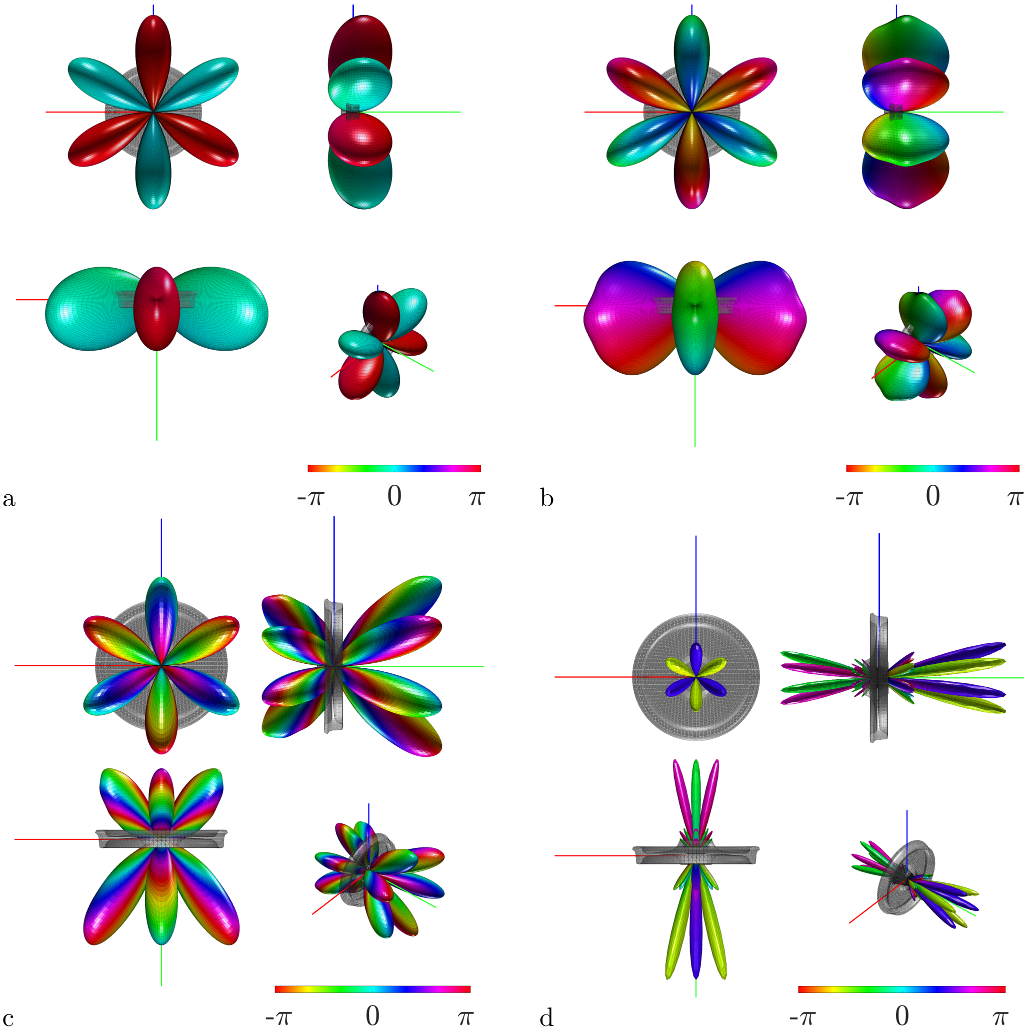

Figure 5.44: Directivity of the axial mode (3,1,a) for (a) 63 Hz, (b) 250 Hz, (c) 1000 Hz, and (d) 4000 Hz.

In Figure 5.46, the $L_{\mathrm{p,eq,1s}}$ of each mode is marked at the location of the mode in the dispersion diagram (cf. Figure 5.33). The colour of the markers indicates their equivalent pressure levels. In particular, there are only a few modes with a high $L_{\mathrm{p,eq,1s}}$ that dominate the sound pressure level. Dominant are axial modes with one or two nodal circles, radial modes, and even some circumferential modes. Above 5 kHz,the different modes types have a similar influence on $L_{\mathrm{p,eq,1s}}$.

The analysis above assumes that the radiated sound power from each mode is independent from the radiation of all other modes. This is not necessarily true as the modes are not

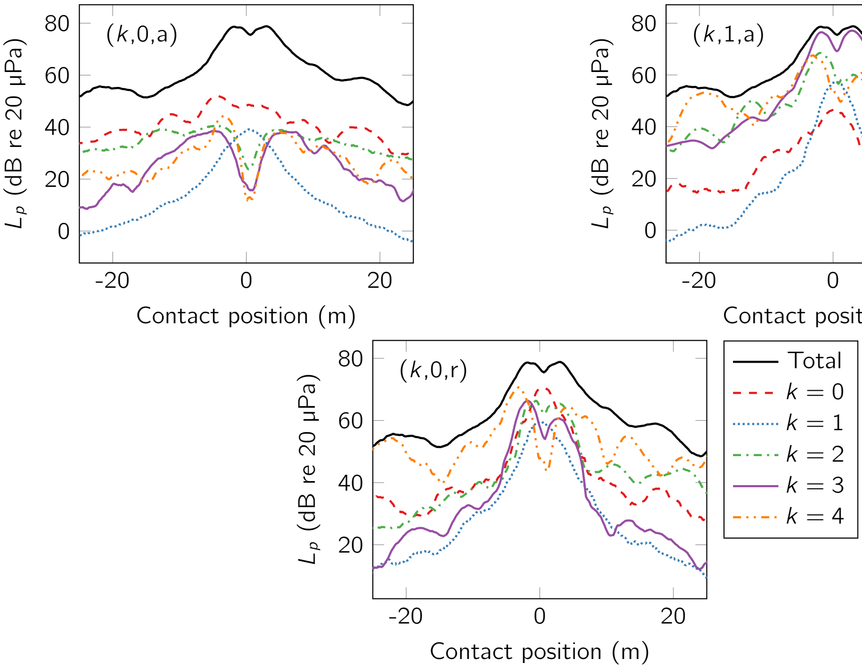

Figure 5.45: Contribution of each individual mode to the pressure during the pass-by of the wheel. The upper figures show axial modes with varying numbers of nodal diameters k, for zero and one nodal circles. The lower figure presents the first few radial modes.

orthogonal with respect to their radiation. To quantify each modes influence on the total sound pressure, a sensitivity analysis is therefore carried out. In this sensitivity analysis, the significance of each mode is quantified by removing its contribution from the total sound pressure. Note that each mode is removed only in the calculation of the acoustic radiation, but remains in the calculation of the dynamic wheel response. Figure 5.47 presents the effect of not including the mode indicated on the vertical axis when calculating the third-octave band pressure level. For clarity, most of the modes with an insignificant effect were not included in the Figure. The results can be divided into three frequency ranges. Below 1 kHz, the two axial modes (0,0,a) and (2,0,a) determine the pressure pressure level. Up to 2 kHz, each third-octave band is dominated by the influence of one single mode ((1,0,r), (2,1,a) and (3,1,a)). The eigenfrequencies of these modes are located in the respective third-octave band. At higher frequencies, the contributions are distributed between several axial and radial modes.

Radiation from each mode is orthogonal in the domain of the wheel. The wheel modes are not orthogonal with respect to sound radiation. Therefore, during the pass-by, different modes can interact even with respect to the radiated sound power, characterised by the pass-by levels. A strong variation of the sound pressure level when removing one mode does therefore not necessarily mean that this mode is the strongest contributor, but has a

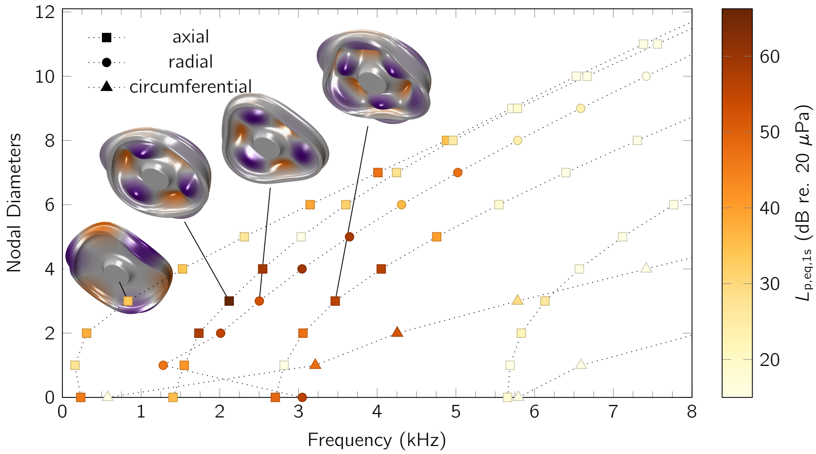

Figure 5.46: Contribution of each mode to the 1 s equivalent sound pressure level $L_{\mathrm{p,eq,1s}}$.

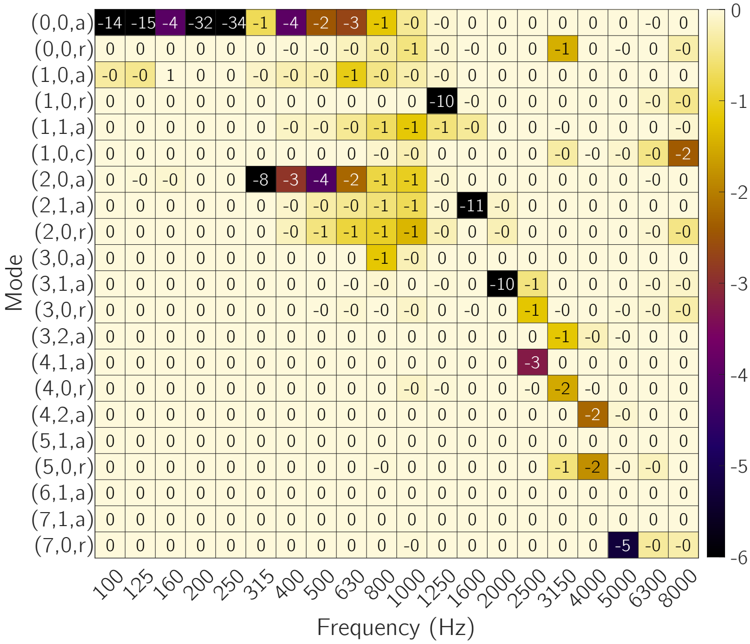

Figure 5.47: Effect of removing the contribution of a single mode on the $L_{\mathrm{p,eq,1s}}$, in dB. The figure contains only a selection of modes, as modes with a negligible effect are not shown.

strong influence on the result. However, Figure 5.48 shows that single modes dominate the pass-by signal at certain frequencies corresponding to their eigenfrequencies. During the pass-by, these frequencies are shifted according to the Doppler-effect.

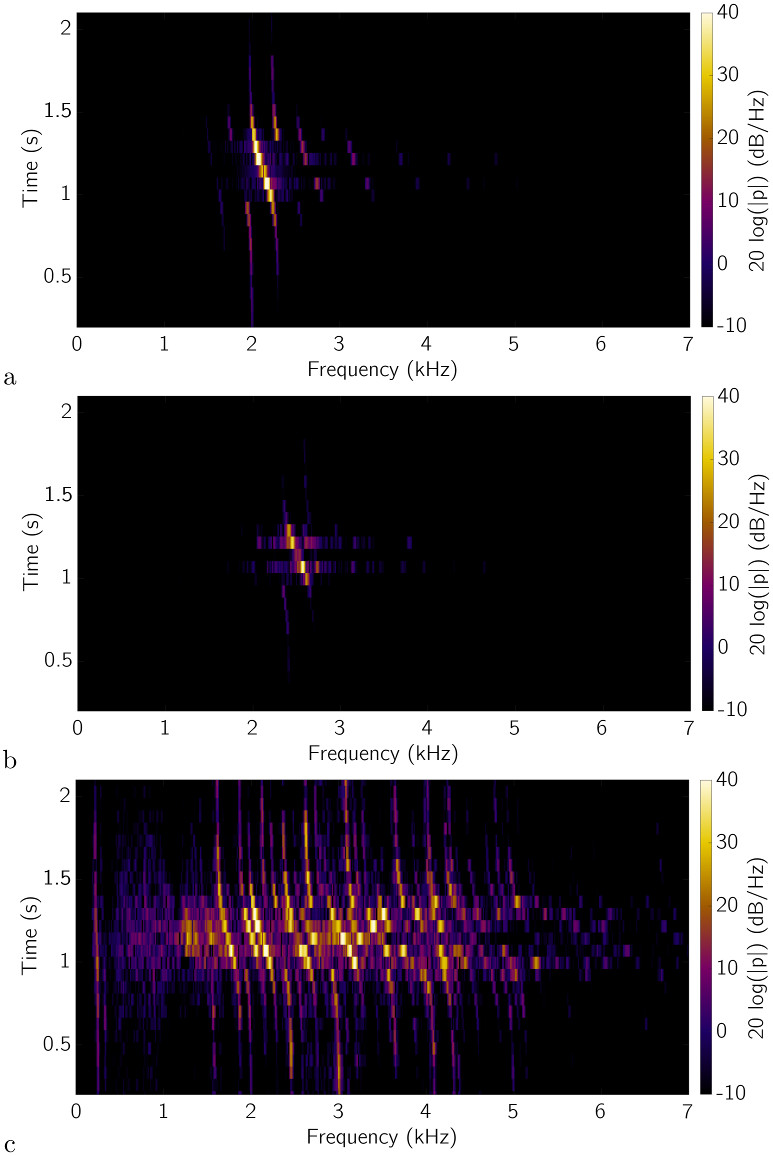

Figure 5.48: Spectrogram of a the pass-by sound pressure at a stationary microphone position. Top (a): mode (3,1,a), (b) mode (3,0,r), (c) total.

6 Conclusions and Future Work

A modular simulation tool for railway rolling noise has been developed. It aims for modelling vibrations in, and sound radiation from, wheels and different types of track in a frequency range relevant for human perception, i.e., frequencies between 20 Hz and 7 kHz. The wide frequency range demanded to combine beneficial numerical methods to make the resulting simulation tool detailed enough for, for example, an auralisation of the pass-by sound signals, while at the same time being efficient enough to, for example, conduct parameter studies to research noise mitigation measures. The following two subsections summarise the work and present conclusions for the track and wheel simulation. In Section 6.3, steps towards an integrated model are described as well as future work needed to overcome limitations of the present work is discussed.

6.1 Simulation of track vibrations and sound radiation

A central task of the thesis work was to develop models for predicting the vibrations and sound radiation for for ballasted and ballastless tracks.

6.1.1 An advanced model to predict railway track vibration and radiation

The structural track models presented in this thesis are mainly based on a WFE approach for the rail coupled to, for example, sleepers or a ballastless track surface. For the frequency range of interest, it is relevant to include all wave types in the rail. For this, the WFE method proved to be an efficient tool for predicting receptances as needed in the complete rolling model. The approach also allows for analysing the dispersion of different waves in the rail to gain better understanding for the vibrations of different track designs. Although the WFE method assumes the rail to be an infinite, continuous waveguide, discrete supports can be introduced by coupling the waveguide to sleepers in discrete points. It was found that including about 100 sleepers is typically sufficient for accurately predicting relevant receptances.

The discrete support was able to reproduce phenomena such as the pinned-pinned resonances which occur whenever the width of two sleeper bays is an integer multiple of a wavelength in the rail. Capturing these resonances is relevant not only for accurately predicting the rolling contact forces, but also the sound radiation from the rail. Including rail seats in discrete positions in the continuous rail model can be realised by introducing coupled reaction forces at the locations of the rail seats. This modelling approach successfully reproduced the measured transfer receptances of a discretely supported, ballasted track.

The WFE approach was also found suitable for modelling the structural response of a ballastless track. The support layers can be modelled in detail by their cross-section, while the assumption of propagating waves along the track limits the numerical effort. Introducing virtual forces at the locations of the rail seats allowed coupling two infinite structures, the rail and the support structure, in a finite number of discrete points. This modelling approach was validated by comparison to measurements on a full-scale test rig in *Paper A*. In this validation, it is observed that measurement uncertainties are introduced by the presence of discontinuities in the rail, the excitation position, and the adjacent structure on either side of the test track which have to be considered in the modelling to make the validation meaningful. To simulate the dynamic response of tracks with booted sleepers, the model was further extended to include a finite number of sleepers between the continuous rail and the continuous support structure as presented in *Paper E*.

A similar approach to the WFE approach for predicting vibration can be used to calculate the sound radiation from the track. Even here, it is necessary to make the assumption that the geometry is constant along the track. The approach allows transforming the sound field along the track into Fourier domain and describing the 3D sound field around the track to be described by 2D sound fields at different wavenumbers. This so-called WBE approach, in turn, allowed a substantial increase of the numerical efficiency by reducing the number of 2D BE problems to be solved for a high resolution 3D sound field shown in *Paper C*. A similar methods has been previously investigated in the context of calculating sound radiation from bridges [137]. Specific adaptions for calculating the spatial sound field radiated from the rail and sleepers were presented in this thesis. The efficiency of the presented approach proved necessary when aiming for a high frequency, time domain prediction of the pass-by sound.

Structure-borne and air-borne quantities were predicted in time domain by using moving Green's functions. It is demonstrated that the WFE and WBE methods allow an efficient prediction by simulating a moving force on the rail. Results show a Doppler shift that is observed at a stationary receiver, not due to the relative motion of the source and the receiver, but instead due to the compression and elongation of the waves in the rail during the pass-by.

6.1.2 The acoustic performance of different track designs

The developed track models have been used for various parameter studies. A variation of parameters in the ballastless track model showed that the rail is the primary sound source among the track components and that the rail pad stiffness is the main direct lever among the track parameters to control the sound emitted from the rail. The slab surface contributes to the sound radiation at low frequencies, and more so with increasing rail pad stiffness. A continuous support has the potential to reduce the total radiated sound at high frequencies. However, increasing the rail pad stiffness on ballastless tracks increases the load on the concrete layers and ground-borne vibration. A follow-up up study was conducted to investigate if similar noise mitigation effects can be achieved without increasing the load on the support structure. The ballastless track model with booted sleepers was used for this purpose, and the boot stiffness, the sleeper mass and the rail pad stiffness were varied. By simulating rolling contact forces, other loads on the track, and the radiated sound power for different sets of track parameters, it was found that the observed rolling forces and track loads depend on the combination of all three parameters. On the other hand, the predicted sound power level depends mostly on the elasticity of the rail pad. Since the sleepers function as dynamic vibration absorbers, decreasing the sound power level leads to higher loads on the sleepers. Accepting this and taking advantage of the sleepers as dynamic vibration absorbers, the sound power was reduced up to 10 dB, for a given combined surface roughness, while not increasing the peak load on the track support. It was observed that, in this context, a softer boot stiffness leads to a larger potential for noise mitigation.

A second focus was given to the question which model complexity is needed for a reliable prediction of track vibrations and radiation. Due to the modular approach, the dynamic model of the rail is easily exchanged by, for example, an analytical beam model. One can conclude that similar predictions of the radiated sound power can be made by Euler-Bernoulli and Timoshenko beam models and WFE-based models up to 2.5 kHz. At higher frequencies, the Timoshenko beam model produces a closer match, although only if the WFE-based rail is in its symmetry axis. Asymmetric excitation on the rail head created differences especially at the cut-on frequency of the lateral bending wave between 60 Hz and 100 Hz and above 4 kHz. Although the radiation ratio is predicted almost identical by all dynamic models, this is not true for the radiated sound power under realistic excitation. Comparing the cross-sectional directivity of the Timoshenko- and the WFE-based model shows a high agreement at symmetric excitation, while the lateral bending wave introduces larger differences for eccentric excitation on the WFE-based rail. The spatial decay of the sound field along the rail is similar for the Timoshenko-beam model and the WFE-based model. Both show similar slopes as the standard track decay rate which measures the decay of vibrational energy in the rail. This relationship between the structure-borne track decay rate and the decay of sound pressure along the track has been explored in more detail. The calculated acoustic responses to a force impulse excitation on the rail is rather short, decaying about 30 dB in 20 ms for all tracks. The Euler-Bernoulli beam theory does not seem to fit for time-domain estimation of sound field quantities, as, due to the higher bending stiffness, the bending wave speed is over-estimated, and the first wave front arrives significantly earlier compared to the Timoshenko-beam theory or the WFE model. The dispersion of the waves in the rail is observed in the changing pressure impulse response over distance. Large differences are observed between the Timoshenko-beam model and the WFE-based model. Since the difference does not affect the sound power, its relevance for human perception should be investigated.

Finally, the radiation from the rail was investigated more closely. For this, the acoustic transfer functions, i.e., the sound pressure in a receiving position due to velocity at different surface points on the rail, are investigated. It shows that surface normal vibration anywhere in the concave section on the side of the rail spreads the sound broadly on either side of the rail, while the vibration on the rail head is more directive.

6.2 Simulation of wheel vibrations and sound radiation

The wheel is the second dominant source of rolling noise, dominating in the frequency range where the hearing is most sensitive. The wheel vibration and sound radiation is most often modelled based on its modal behaviour, which is the approach used here.

6.2.1 The use of WFE, FBEM and moving Green's functions for simulating sound radiation from the wheel

A model for the dynamic behaviour of the wheel was developed based on the WFE method. In analogy to the rail where wave propagation in an infinite waveguide is assumed, here waves propagate around the symmetry axis of the wheel. The main difference is that here, only discrete wavenumbers exist, while the wavenumber spectrum is continuous for the rail. Since the wave field around the circumference of the wheel needs to be continuous, only integer numbers of wavelengths fit around the circumference. The approach allows for an efficient identification of wheel modes, calculation of the dispersion relation and calculation of relevant receptances.

In addition, a tool for calculating the sound radiation from the wheel was developed that uses the Fourier series Boundary Element method. This method aptly integrates with the curved WFE method, as each BE Fourier order corresponds to one integer wavenumber. The method was extended by including the ground as a perfectly reflective surface by using half-space Green's functions. The extension has the disadvantage of coupling previously decoupled Fourier orders, however, the number of degrees of freedom in the BE model is still significantly lower than in a full 3D model. Still, the straightforward use of this method did not appear numerically feasible for calculating the pass-by sound pressure signals of a wheel.

Therefore, for predicting the pass-by sound pressure signals of a wheel in time domain, a calculation approach was developed that makes use of the modal behaviour of the wheel and the method of equivalent sources. The approach followed here is to first calculate the acoustic impulse response function from each mode with a unit modal amplitude on a reference surface and then approximate this field on the reference surface by spherical harmonics. This allows for evaluating the BE model with a relatively low frequency resolution. Further, the spherical harmonics description of the sound field allows the efficient calculation of the impulse responses while changing the relative position of wheel and receiver without the need for re-evaluating the BE problem. The long dynamic impulse response of the wheel can this way be captured in an analytical expression for the modal decay in time domain, and together with the contact forces be included in so-called source terms. These source terms, convolved with the predicted acoustic impulse responses for each mode, predict the contribution of each mode on the pass-by signal. The total pressure is evaluated by summing the contributions of all modes.

6.2.2 The stationary and pass-by sound radiated by a wheel

The presented model has been used to evaluate the sound radiation from a railway wheel in the presence of a reflective plane, such as a slab track surface. The radiation efficiencies for different modes of the wheel are in agreement with those found in literature. The effect of a reflecting plane on the radiated sound power of a railway wheel was shown to be rather small, so that the free-wheel assumption typically used in literature is valid above about 150 Hz, even for wheels on slab tracks or tram wheels on embedded rails. The sound pressure produced by a vibrating wheel in an acoustic half-space was compared to the wheel in free space and to an approximation of the half-space by mirror-sources. It is found that the approximation via mirror-sources can not generally predict the sound pressure in specific points correctly, except below 100 Hz. In a second step, the sound radiation from a vibrating wheel moving along a straight track was calculated. Evaluating the modal contributions of one example wheel to radiated sound for one example wheel and rail roughness, it was found that mainly the axial modes $(0, 0, a)$ and $(2, 0, a)$ are responsible for the sound pressure level below 1 kHz, above which the three modes $((1, 0, r)$, $(2, 1, a)$ and $(3, 1, a))$ dominate the third-octave band that contains their respective eigenfrequency up to 2 kHz. For higher frequencies, the contribution is more evenly shared between several higher modes. The directivity of individual modes is rather complex, increasingly so for higher order modes. At high frequencies, the main radiation direction is lateral to the sides of the wheel, even for radial modes. This complex directivity means that different modes dominate the sound pressure at different relative positions between the wheel and the receiver position.

6.3 Future work towards a combined simulation tool for railway rolling noise

The presented work describes a modelling approach for predicting pass-by signals from track and wheel. Future research can address limitations in the current model or explore research questions that can be answered with the existing modelling approach.

Some limitations are listed in the following. Regarding the prediction of the structural vibrations, one often discussed assumption is that nonlinearities of the track have been linearised, such as the stiffness of the ground and the rail pads. This assumption is necessary due to the frequency domain calculation of the track vibration, and with this approach, there is no simple way to avoid this. Nevertheless, this is a standard assumption and the model is able to predict the transfer receptances of real, yet unloaded, tracks. The linear model of the rail pads used in this thesis considers, as of now, the vertical and lateral direction to be decoupled. This simplification is currently only due to the lack of a more accurate model of the rail pad. Since the WFE rail provides the 3D motion of the rail foot, a 3D coupling through the rail pad could be realised. While possible to use more elaborate models, here, sleepers were approximated by simple masses.

Secondly, wheel rotation is disregarded when determining the moving Green's functions.

Including the wheel rotation is possible as mentioned in Section 2.4.1. It is further known that several wheels can dynamically interact through the rail [177]. Wheels on different rails are of course also coupled though the wheelset, which is currently not included. The effect of both of those couplings on the sound radiation from wheels and rail could be investigated.

Further research also concerns the acoustic predictions. The acoustic absorption of the track and on the propagation path to the receiver is not included in the sound radiation model of the track or the wheel. Including absorption in the method presented in Section 3.2, which allows an efficient calculation of the sound field around a railway track, is not straightforward. Including absorption in the sound radiated by wheel modes is possible by using a 3D BE model as for example presented by Brick et al. [156]. The rotation of the wheel is disregarded in the sound radiation as well, and including this rotation is a possible improvement of the method. However, the acoustic geometry surrounding the wheel including brakes, bearing housings, the bogie and the vehicle underbody might have a significant effect on the wheel directivity as well. An analysis of the necessary degree of detail in such a calculation is necessary. The additional geometrical features might be more conveniently included in Cartesian rather than cylindrical coordinates. The equivalent source method employed to characterise the sound field produced by the vibrating wheel showed that a maximum expansion order of 35 or higher is found to be required to satisfy the chosen error measures. However, depending on the application, much lower SH orders might be sufficient. Future work might consider a perceptual evaluation of the required maximum SH expansion order for the auralisation of a pass-by. Another aspect influencing the sound radiation is that the turbulent flow of air around the wheel and the track is ignored, which might have some effect on the sound radiation.

Parts of the model have been validated by analytical models or by comparison to measurements in laboratory or in-situ conditions. The complete model has only been validated in a qualitative way by comparing to results found in the literature. A validation of the whole modelling chain is therefore very desirable. For this, however, a variety of the input data are needed such as, among others, the track and wheel properties, the roughness of the wheel and rail running surfaces, the wheel loads and vehicle speed, ideally the contact position, and several more. A well validated model has numerous potential applications beyond those presented in this thesis. Since the simulation tool combines models for structural vibration and sound radiation, it can, for example, aid the optimisation of track and wheel designs and explore potential noise mitigation measures.

Being able to predict the sound field around the track and the wheel in time domain, based on the force input in both components, opens up the opportunity to auralise the pass-by of trains. This allows for predicting sound levels based on the non-linear interaction between the wheel and the rail. This way, the effect of transient events in the rolling contact, for example due to wheel flats, on human perception, can be investigated. In addition, stationary noise which is inadequately captured by equivalent levels, such as tonal noise occurring after rail grinding, can be analysed with a psychoacoustic perspective. In the long term, this detailed physical model could possibly be simplified and combined with models for other noise sources such as aerodynamic to produce a tool for demonstration of railway noise and communication to the public when planning new tracks.

7 Summary of the appended papers

Paper A: Calibration and validation of two models for the dynamic response of slab track using data from a full-scale test rig

This paper aims to validate two modelling approaches for slab track dynamics by comparison to transfer function measurements on a full-scale slab track. Impact hammer measurements were performed on a slab track test facility in the State Key Laboratory of Traction Power, South West Jiaotong University, Chengdu, P.R. China. The measurements provide transfer functions between excitations on the rail and displacements on the slab and substructure. Two finite element modelling approaches are developed to model the dynamic behaviour of this track. The first model is a three-dimensional finite element model, in which the rails are modelled as Rayleigh–Timoshenko beams and the concrete slab and support layer are modelled using linear plate elements. The second model uses a waveguide finite element modelling approach, assuming a constant cross-section for the rail and the track and exponentially decaying, propagating waves along the track. A two-step procedure is applied to calibrate the models, including (i) a parametric study and (ii) a genetic algorithm. Finally, the transfer functions calculated with both calibrated models are compared with the measurements. A satisfactory agreement is found between the measured and calculated transfer functions, both for those TFs included in the calibration and for others that were not included in the parameter matching. This implies that both models can successfully represent the dynamic properties of the test rig and can be considered validated.

Paper B: The Influence of Track Parameters on the Sound Radiation from Slab Tracks

A frequency-wavenumber domain model is developed for the dynamic response of slab tracks, including the discrete coupling of rail and slab. The surface velocities are used as input to a wavenumber domain boundary element model. This enables the evaluation of the transfer function for a unit force input at the top of the rail to the total radiated sound power. A parameter study is conducted that focusses on (i) the stiffness of the rail pad, (ii) the thickness of the slab, and (iii) the type of support: continuous or discrete. As for ballasted tracks, increasing the stiffness of the rail pad is found to decrease the total radiated sound power. The stiffness of the rail pad is of major significance, especially for the discretely coupled rail. For a continuously supported rail, the total sound power is reduced, and the stiffness of the rail pad is less influential. The slab and rail contributions are calculated separately. An evaluation of the contribution of the slab vibration to the total sound shows a minor significance of the noise produced by the slab surface.

Paper C: Efficient calculation of the three-dimensional sound pressure field around a railway track

Sound radiation from railway track is efficiently modelled using a wavenumber domain Boundary element (or 2.5D BE) approach, since the 3D numerical solution is replaced by a series of 2D BE problems at each frequency, effectively reducing the computational load. However, when high spatial and temporal resolutions of the sound field are required, the number of necessary 2D calculations is still unfeasibly high. Two ways to decrease the computational load of such a computation are developed: First, an algorithm is developed that allows the calculation of the 3D sound pressure field around a railway track using a single 2D BE solution at each frequency and an appended interpolation and scaling operation. This is possible since the wavenumbers in the BE solution are identical for different combinations of frequencies and wavenumbers along the track. The method is validated by comparison to the standard 2.5D method and an analytical model. Secondly, a method to precalculate these acoustic transfer functions is described. Having precalculated these transfer functions, the sound radiation from varying track vibration can be calculated by simple multiplication and summation. Some of such precalculated transfer functions are presented and made available online.

Paper D: Towards time-domain modelling of wheel/rail noise: effect of the dynamic track model

The method developed in Paper C allows the calculation of transfer functions between a force acting on the rail and the sound pressure in a point near the railway track. The dynamic behaviour of the track is, therefore, part of this transfer function. Different dynamic track models, in turn, affect the radiated sound field in different ways. This paper explores the influence of this dynamic track model on the sound field around the railway track by comparing six modelling approaches, which involve different analytical and numerical approaches to modelling the rail as well as three different types of rail support. Several descriptors of the sound field are analysed, involving the sound power and radiation efficiency, the sound pressure along the track in frequency- and time-domain, and the spatial decay of the sound field.

Paper E: Optimising components in the rail support system for dynamic vibration absorption and pass-by noise reduction

This paper features an application of the methods developed in Papers A-D by exploring the radiated sound from the track and the forces introduced into the track substructure during the pass-by of a realistic force on the rail. The paper explores two-stage elastic supports, featuring an elastically supported mass on the slab track surface, as a means to reduce noise while not increasing the tack loads (and hence the ground vibrations). The dynamic modelling approach is based on two coupled waveguide Finite Element models, one for the rail and one for the slab and other track support layers, comparable to Paper A and Paper B. An analytical formulation for the two-stage elastic supports is introduced here. The acoustic radiation from the three components, the slab track, the sleepers, and the rail, is modelled via acoustic transfer functions introduced in Paper C. Track forces and noise radiation are compared for several setups with parametrised rail support components in a time-domain simulation. The results show that (I) the rail pad stiffness is the major lever for adjusting the radiated sound power, (II) the lower stiffness is important for adjusting the rolling contact forces and load on the track components, and (III) that optimising for a lower sound power generally produces higher rolling contact forces.

Paper F: Sound Radiation from Railway Wheels including Ground Reflections: A half-space formulation for the Fourier Boundary Element Method

This paper develops a method to evaluate the sound radiation from axisymmetric bodies based on the curved Waveguide Finite Element (WFE) and Fourier series Boundary Element Method (FBEM). A half-space formulation of the Green's functions is integrated in the Boundary Element Method to account for ground reflection from an acoustically hard ground. The acoustically hard ground could, for example, be a slab track surface or the street surface in an embedded rail tram system. The developed method is compared to analytical models and noise measurements of a vibrating steel disk in an unechoic environment. Furthermore, the radiation ratio of a full-size railway wheel is compared to published literature, and a similar behaviour is observed. The influence of the reflective plane on the radiation efficiency of railway wheels is researched. It is found that for the researched railway wheel, there is no major influence of the track surface on the radiation efficiency. However, the sound pressure at specific receiver positions can be significantly different. An approximation of the half-space by a mirror source does not yield a close agreement across the frequency spectrum.

Paper G: On the efficient simulation of pass-by time signals from railway wheels

Paper G develops a method to simulate the pass-by noise of the railway wheels in the time domain. Radiation from train wheels is typically the dominant source of rolling noise above about 2 kHz to 4 kHz. Although wheel vibrations can be conveniently calculated with the WFE method in cylindrical coordinates, predicting the sound pressure in a linear line of receivers is more challenging. Aiming for a spatial resolution adequate for auralising the pass-by rolling noise is computationally expensive with a BE approach. Such an auralisation further requires a high temporal resolution, which, in combination with the low structural damping of the wheel, produces a dense and wide frequency spectrum of the radiated sound. To overcome these challenges, this paper uses a modal approach for both the vibration and the radiation of the wheel, as outlined below.

First, the radiation from mode shapes with a unit amplitude to a reference sphere is calculated in a BE model. These radiation functions are short in time, i.e. fairly flat in frequency domain, allowing a coarse frequency resolution in the calculation. Then, the sound field on the reference sphere is described by a set of spherical harmonics equivalent sources. This allows to, for each mode, efficiently calculate transfer functions to the sound pressure at an arbitrary position along the track. Green's functions are obtained via the inverse Fourier transform of these transfer functions. Next, a source signal is calculated which describes the excitation of the wheel modes over time and space, based on the contact forces between the rail and the wheel, the movement of the wheel along the track, and the frequency response of each mode. Now, at each time step, this modal amplitude can be scaled with the Green's function corresponding to the mode and the relative position between the wheel and the stationary observer. Convolution of the scaled Green's functions with the source signal generates the pass-by pressure signal of one mode. Finally, summing the contributions of all included modes produces the total pressure signal.

In this way, it is numerically feasible to calculate pass-by signals of several seconds in the frequency range of interest. The approach also facilitates an analysis of the most dominant wheel modes and determines a few modes as main contributors to the pass-by signal for the specific case of wheel, rail, contact geometry, and roughness considered here. An analysis of the directivity of several wheel modes found that most structural modes, including radial modes, radiate dominantly in the axial direction, especially at high frequencies. However, because of the interaction of several regions on the surface, the radiation is rarely purely axial; instead, the main lobes in the directivity are at an angle with the wheel axis. The method can be extended to include reflections from the ground and other surrounding surfaces, such as the floor of the wagon, by using a 3D BE solver.

References

[1] United Nations. Sustainable transport, sustainable development. Interagency report for second Global Sustainable Transport Conference. 2021.

[2] International Energy Agency. The Future of Rail: Opportunities for energy and the environment. OECD Publishing. 2019.

[3] International Transport Forum. ITF Transport Outlook 2021. OECD Publishing. 2021.

[4] International Transport Forum. Transport brief: Keeping 1.5°C Alive: Transport at COP26. OECD Publishing. 2021.

[5] European Commission, Directorate-General for Mobility and Transport. EU transport in figures : statistical pocketbook 2021. Publications Office. 2021.

[6] Inventory of U.S. Greenhouse Gas Emissions and Sinks 1990-2020. EPA 430-R-22-003. U.S. Environmental Protection Agency. 2022.

[7] The European Commission. White Paper: Roadmap to a Single European Transport Area - Towards a competitive and resource efficient transport system. 2011.

[8] European Environmental Agency. Share of energy consumption from renewable sources in Europe. URL: `https://www.eea.europa.eu/ims/share-of-energy-consumption-from` (visited on 10/18/2022).

[9] European Commission. Directorate General for Energy., European Commission. Directorate General for Climate Action. and European Commission. Directorate General for Mobility and Transport. EU energy, transport and GHG emissions, trends to 2050 :reference scenario 2013. LU: Publications Office. 2014.

[10] International Union of Railways. High Speed Traffic in the World. 2020.

[11] Anders Lindfeldt. Railway capacity analysis: methods for simulation and evaluation of timetables, delays and infrastructure. PhD thesis. Stockholm: KTH Royal Institute of Technology, 2015.

[12] R. M. Andrew. Global CO2 emissions from cement production, 1928–2018. *Earth System Science Data.* **11**(4) (2019), 1675–1710.

[13] International Union of Railways. Rail Transport and Environment: Facts and Figures. 2015.

[14] International Union of Railways. Carbon footprint of railway infrastructure. 2016. ISBN: 978-2-7461-2500-1.

[15] World Health Organisation, ed. Burden of disease from environmental noise: quantification of healthy life years lost in Europe. Copenhagen: World Health Organization, Regional Office for Europe. 2011.

[16] C. Eriksson, T. Bodin and J. Selander. Burden of disease from road traffic and railway noise – a quantification of healthy life years lost in Sweden. *Scandinavian Journal of Work, Environment & Health.* **43**(6) (2017), 519–525.

[17] T. Münzel et al. Environmental Noise and the Cardiovascular System. *Journal of the American College of Cardiology.* **71**(6) (2018), 688–697.

[18] ISO. *Acoustics — Description, measurement and assessment of environmental noise — Part 1: Basic quantities and assessment procedures.* Standard ISO 1996-1:2016(E). Geneva, Switzerland: International Organization for Standardization, 2016.

[19] International Union of Railways. UIC NETWORK NOISE & VIBRATION. 2019.

[20] J. Kaku and M. Yamashita. Impact noise from railroads. *Journal of Sound and Vibration.* **120**(2) (1988), 333–337.

[21] P. T. Torstensson et al. Wheel–rail impact loads and noise generated at railway crossings – Influence of vehicle speed and crossing dip angle. *Journal of Sound and Vibration.* **456** (2019), 119–136.

[22] J. C. O. Nielsen et al. “Wheel–Rail Impact Loads, Noise and Vibration: A Review of Excitation Mechanisms, Prediction Methods and Mitigation Measures”. *Noise and Vibration Mitigation for Rail Transportation Systems.* Ed. by G. Degrande et al. Vol. 150. Notes on Numerical Fluid Mechanics and Multidisciplinary Design. Cham: Springer International Publishing. 2021, pp. 3–40.

[23] D. J. Thompson. Railway noise and vibration: mechanisms, modelling and means of control. 1st ed. Amsterdam ; Boston: Elsevier. 2009. ISBN: 978-0-08-045147-3.

[24] D. J. Thompson. Wheel-rail Noise Generation, Part I: Introduction And Interaction Model. *Journal of Sound and Vibration.* **161**(3) (1993), 387–400.

[25] A. Pieringer, W. Kropp and D. J. Thompson. Investigation of the dynamic contact filter effect in vertical wheel/rail interaction using a 2D and a 3D non-Hertzian contact model. *Wear.* Proceedings of the 8th International Conference on Contact Mechanics and Wear of Rail / Wheel Systems, Florence, 2009 **271**(1) (2011), 328–338.

[26] C. Mellet et al. High speed train noise emission: Latest investigation of the aerodynamic/rolling noise contribution. *Journal of Sound and Vibration.* **293**(3-5) (2006), 535–546.

[27] X. Zhang et al. The effects of ballast on the sound radiation from railway track. *Journal of Sound and Vibration.* **399** (2017), 137–150.

[28] R. J. Diehl, R. Nowack and G. Hölzl. Solutions for acoustical problems with ballastless track. *Journal of Sound and Vibration.* **231**(3) (2000), 899–906.

[29] S. Van Lier. The vibro-acoustic modelling of slab track with embedded rails. *Journal of Sound and Vibration.* **231**(3) (2000), 805–817.

[30] U. Moehler et al. The New German Prediction Model for Railway Noise "Schall 03 2006": An Alternative Method for the Harmonised Calculation Method Proposed in the EU Directive on Environmental Noise. *Acta Acustica united with Acustica.* **94**(4) (2008), 548–552.

[31] P.-E. Gautier. Slab track: Review of existing systems and optimization potentials including very high speed. *Construction and Building Materials.* **92** (2015), 9–15.

[32] F. Poisson. "Railway Noise Generated by High-Speed Trains". *Noise and Vibration Mitigation for Rail Transportation Systems.* Ed. by J. C. O. Nielsen et al. Vol. 126. Notes on Numerical Fluid Mechanics and Multidisciplinary Design. Berlin, Heidelberg: Springer Berlin Heidelberg. 2015, pp. 457–480.

[33] R. Görlich, R. Diehl and G. Hölzl. "DE19706542A1". Pat. 197 06 542.2 (München). 2007.

[34] G. Müller and M. Möser. Handbook of Engineering Acoustics. (2013).

[35] X. Zhang et al. The noise radiated by ballasted and slab tracks. *Applied Acoustics.* **151** (2019), 193–205.

[36] European Commission. Joint Research Centre. ICHP. Common noise assessment methods in Europe (CNOSSOS-EU): to be used by the EU member states for strategic noise mapping following adoption as specified in the environmental noise directive 2002/49/EC. Publications Office. 2012.

[37] S. P. Timoshenko. Method of analysis of statical and dynamical stress in rails. Zurich; (1926), 407–418.

[38] D. J. Thompson. Wheel-rail Noise Generation, Part III: Rail Vibration. *Journal of Sound and Vibration.* **161**(3) (1993), 421–446.

[39] J. C. O. Nielsen and A. Igeland. Vertical dynamic interaction between train and track influence of wheel and track imperfections. *Journal of Sound and Vibration.* **187**(5) (1995), 825–839.

[40] K. Knothe and S. L. Grassie. Modelling of Railway Track and Vehicle/Track Interaction at High Frequencies. *Vehicle System Dynamics.* **22**(3-4) (1993), 209–262.

[41] A. Nordborg. Wheel/rail noise generation due to nonlinear effects and parametric excitation. *The Journal of the Acoustical Society of America.* **111**(4) (2002), 1772–1781.

[42] C.-M. Nilsson et al. A waveguide finite element and boundary element approach to calculating the sound radiated by railway and tram rails. *Journal of Sound and Vibration.* **321**(3-5) (2009), 813–836.

[43] A. H. W. M. Kuijpers, G. Verbeek and J. W. Verheij. An improved acoustic Fourier boundary element method formulation using fast Fourier transform integration. *The Journal of the Acoustical Society of America.* **102**(3) (1997), 1394–1401.

[44] D. J. Thompson and C. J. C. Jones. Sound radiation from a vibrating railway wheel. *Journal of Sound and Vibration.* **253**(2) (2002), 401–419.

[45] C. Hoever. The simulation of car and truck tyre vibrations, rolling resistance and rolling noise. Doctoral thesis. Chalmers University of Technology, 2014, pp. 1–118.

[46] D. J. Thompson, B. Hemsworth and N. Vincent. Experimental validation of the twins prediction program for rolling noise, part 1: description of the model and method. *Journal of Sound and Vibration.* **193**(1) (1996), 123–135.

[47] D. J. Thompson, P. Fodiman and H. Mahé. Experimental validation of the twins prediction program for rolling noise, part 2: results. *Journal of Sound and Vibration.* **193**(1) (1996), 137–147.

[48] D. J. Thompson and C. J. C. Jones. A review of the modelling of wheel/rail noise generation. *Journal of Sound and Vibration.* **231**(3) (2000), 519–536.

[49] J. C. O. Nielsen et al. Train-Track Interaction and Mechanisms of Irregular Wear on Wheel and Rail Surfaces. *Vehicle System Dynamics.* **40**(1-3) (2003), 3–54.

[50] D. P. Connolly et al. Benchmarking railway vibrations – Track, vehicle, ground and building effects. *Construction and Building Materials.* **92** (2015), 64–81.

[51] A. Pieringer. Time-domain modelling of high-frequency wheel/rail interaction. Doctoral Thesis. Gothenburg, Sweden: Chalmers University of Technology, 2011.

[52] S. L. Grassie et al. The Dynamic Response of Railway Track to High Frequency Vertical Excitation. *Journal of Mechanical Engineering Science.* **24**(2) (1982). Publisher: IMECHE, 77–90.

[53] P. J. Remington. Wheel/rail noise— Part I: Characterization of the wheel/rail dynamic system. *Journal of Sound and Vibration.* **46**(3) (1976), 359–379.

[54] P. J. Remington. Wheel/rail noise—Part IV: Rolling noise. *Journal of Sound and Vibration.* **46**(3) (1976), 419–436.

[55] P. J. Remington. Wheel/rail rolling noise, I: Theoretical analysis. *The Journal of the Acoustical Society of America.* **81**(6) (1987), 1805–1823.

[56] D. J. Thompson. Wheel-rail Noise Generation, Part II: Wheel Vibration. *Journal of Sound and Vibration.* **161**(3) (1993), 401–419.

[57] D. J. Thompson. Wheel-rail Noise Generation, Part IV: Contact Zone And Results. *Journal of Sound and Vibration.* **161**(3) (1993), 447–466.

[58] D. J. Thompson. Wheel-rail Noise Generation, Part V: Inclusion Of Wheel Rotation. *Journal of Sound and Vibration.* **161**(3) (1993), 467–482.

[59] M. Heckl. Proposal for a railway simulation program. A Workshop on Rolling Noise Generation (1989), 128–148.

[60] T. X Wu and D. J Thompson. A hybrid model for the noise generation due to railway wheel flats. *Journal of Sound and Vibration.* **251**(1) (2002), 115–139.

[61] A. Pieringer. A numerical investigation of curve squeal in the case of constant wheel/rail friction. *Journal of Sound and Vibration.* **333**(18) (2014), 4295–4313.

[62] I. Zenzerovic. Time-domain modelling of curve squeal: a fast model for one- and two-point wheel/rail contact. Doctoral thesis. Gothenburg, Sweden: Chalmers University of Technology, 2017.

[63] W. Kropp, J. Theyssen and A. Pieringer. The application of dither to mitigate curve squeal. *Journal of Sound and Vibration.* **514** (2021), 116433.

[64] T. Mazilu et al. Using the Green's functions method to study wheelset/ballasted track vertical interaction. *Mathematical and Computer Modelling.* **54**(1-2) (2011), 261–279.

[65] A. Pieringer, W. Kropp and J. C. O. Nielsen. The influence of contact modelling on simulated wheel/rail interaction due to wheel flats. *Wear*. Proceedings of the 9th International Conference on Contact Mechanics and Wear of Rail / Wheel Systems, Chengdu, 2012 **314**(1) (2014), 273–281.

[66] X. Sheng, X. Xiao and S. Zhang. The time domain moving Green function of a railway track and its application to wheel–rail interactions. *Journal of Sound and Vibration.* **377** (2016), 133–154.

[67] X. Li, J. C. O. Nielsen and P. T. Torstensson. Simulation of wheel–rail impact load and sleeper–ballast contact pressure in railway crossings using a Green's function approach. *Journal of Sound and Vibration.* **463** (2019), 114949.

[68] M. Chen, Y. Sun and W. Zhai. High efficient dynamic analysis of vehicle–track–subgrade vertical interaction based on Green function method. *Vehicle System Dynamics.* **58**(7) (2020), 1076–1100.

[69] D. J. Thompson and N. Vincent. Track Dynamic Behaviour at High Frequencies. Part 1: Theoretical Models and Laboratory Measurements. *Vehicle System Dynamics.* **24**(sup1) (1995), 86–99.

[70] J. J. Kalker. Variational Principles of Contact Elastostatics. *IMA Journal of Applied Mathematics.* **20**(2) (1977), 199–219.

[71] M. Kleiner, B.-I. Dalenbäck and P. Svensson. Auralization-An Overview. *Journal of the Audio Engineering Society.* **41**(11) (1993), 861–875.

[72] G. Degrande et al. SILVARSTAR - Soil Vibration and Auralisation Software Tools for Application in Railways; State-of-the-art and concept of the vibration prediction tool. European Commission. 2021.

[73] Reto Pieren et al. SILVARSTAR - Soil Vibration and Auralisation Software Tools for Application in Railways. Deliverable D4.1: Methodology for auralisation adn virtual reality of railway noise. European Commission. 2021, p. 31.

[74] R. Pieren et al. Auralization of railway noise: Emission synthesis of rolling and impact noise. *Applied Acoustics.* **127** (2017), 34–45.

[75] X. Zhang et al. An engineering model for the prediction of the sound radiation from a railway track. *Journal of Sound and Vibration.* **461** (2019), 114921.

[76] Coenraad Esveld. Modern Railway Track. Ed. by Dior Zwarthoed-van Nieuwenhuizen. 2nd ed. Zaltbommel, The Netherlands: MRT-Productions. 2001.

[77] Jannik Theyssen. Modelling the acoustic performance of slab tracks. en. Licentiate Thesis. Gothenburg, Sweden: Chalmers University of Technology, 2020.

[78] E. Aggestam. Slab track optimisation considering dynamic train–track interaction. Doctoral Thesis. Gothenburg, Sweden: Chalmers University of Technology, 2021.

[79] I. Elishakoff. Who developed the so-called Timoshenko beam theory? *Mathematics and Mechanics of Solids.* **25**(1) (2020), 97–116.

[80] S. P. Timoshenko. On the correction for shear of the differential equation for transverse vibrations of prismatic bars. *The London, Edinburgh, and Dublin Philosophical Magazine and Journal of Science.* **41**(245) (1921), 744–746.

[81] M. Hetényi. Beams on elastic foundation: theory with applications in the fields of civil and mechanical engineering. 13. pr. University of Michigan studies Scientific series 16. Ann Arbor, Mich: The University of Michigan Press. 1946.

[82] P. J. Remington. Wheel/rail rolling noise: What do we know? What don't we know? Where do we go from here? *Journal of Sound and Vibration.* **120**(2) (1988), 203–226.

[83] E. Tassilly and N. Vincent. A linear model for the corrugation of rails. *Journal of Sound and Vibration.* **150**(1) (1991), 25–45.

[84] M. L. Munjal and M. Heckl. Vibrations of a periodic rail-sleeper system excited by an oscillating stationary transverse force. *Journal of Sound and Vibration.* **81**(4) (1982), 491–500.

[85] J. C. O. Nielsen. Eigenfrequencies and eigenmodes of beam structures on an elastic foundation. *Journal of Sound and Vibration.* **145**(3) (1991), 479–487.

[86] B. Ripke and K. Knothe. Simulation of High Frequency Vehicle-Track Interactions. *Vehicle System Dynamics.* **24**(1) (1995), 72–85.

[87] D. M. Mead. Wave propagation in continuous periodic structures: research contributions from southampton, 1964–1995. *Journal of Sound and Vibration.* **190**(3) (1996), 495–524.

[88] M. A. Heckl. Railway noise - can random sleeper spacings help? *Acustica.* **81** (1995).

[89] M. A. Heckl. Coupled waves on a periodically supported timoshenko beam. *Journal of Sound and Vibration.* **252**(5) (2002), 849–882.

[90] T. X. Wu and D. J. Thompson. A double timoshenko beam model for vertical vibration analysis of railway track at high frequencies. *Journal of Sound and Vibration.* **224**(2) (1999), 329–348.

[91] M. Heckl. Bending Wave Propagation on Periodic Structures. *The Journal of the Acoustical Society of America.* **32**(11) (1960), 1512–1513.

[92] D. J. Mead. A general theory of harmonic wave propagation in linear periodic systems with multiple coupling. *Journal of Sound and Vibration.* **27**(2) (1973), 235–260. (Visited on 11/01/2022).

[93] Ruth M. Orris and M. Petyt. A finite element study of harmonic wave propagation in periodic structures. *Journal of Sound and Vibration.* **33**(2) (1974), 223–236.

[94] K. Knothe, Z. Strzyzakowski and K. Willner. Rail Vibrations in the High Frequency Range. *Journal of Sound and Vibration.* **169**(1) (1994), 111–123.

[95] L. Gavrić. Computation of propagative waves in free rail using a finite element technique. *Journal of Sound and Vibration.* **185**(3) (1995), 531–543.

[96] I. Bartoli et al. Modeling wave propagation in damped waveguides of arbitrary cross-section. *Journal of Sound and Vibration.* **295**(3) (2006), 685–707.

[97] J. Ryue et al. Decay rates of propagating waves in railway tracks at high frequencies. *Journal of Sound and Vibration.* **320**(4-5) (2009), 955–976.

[98] X. Sheng, C. J. C. Jones and D. J. Thompson. Responses of infinite periodic structures to moving or stationary harmonic loads. *Journal of Sound and Vibration.* **282**(1-2) (2005), 125–149.

[99] X. Zhang et al. A model of a discretely supported railway track based on a 2.5D finite element approach. *Journal of Sound and Vibration.* **438** (2019), 153–174.

[100] G. Lombaert et al. The experimental validation of a numerical model for the prediction of railway induced vibrations. *Journal of Sound and Vibration.* **297**(3-5) (2006), 512–535.

[101] P. Galvín et al. A 2.5D coupled FE-BE model for the prediction of railway induced vibrations. *Soil Dynamics and Earthquake Engineering.* **30**(12) (2010), 1500–1512.

[102] P. Alves Costa, R. Calçada and A. Silva Cardoso. Track–ground vibrations induced by railway traffic: In-situ measurements and validation of a 2.5D FEM-BEM model. *Soil Dynamics and Earthquake Engineering.* **32**(1) (2012), 111–128.

[103] A. Dijckmans et al. Mitigation of railway induced ground vibration by heavy masses next to the track. *Soil Dynamics and Earthquake Engineering.* **75** (2015), 158–170.

[104] D. Ghangale et al. "A Methodology for the Assessment of Underground Railway-Induced Vibrations Based on Radiated Energy Flow Computed by Means of a 2.5D FEM-BEM Approach". *Noise and Vibration Mitigation for Rail Transportation Systems.* Ed. by G. Degrande et al. Vol. 150. Notes on Numerical Fluid Mechanics and Multidisciplinary Design. Cham: Springer International Publishing. 2021, pp. 445–453.

[105] H. Li, D. J. Thompson and G. Squicciarini. A 2.5D acoustic finite element method applied to railway acoustics. *Applied Acoustics.* **182** (2021), 108270.

[106] T. Gras et al. On a coupling between the Finite Element (FE) and the Wave Finite Element (WFE) method to study the effect of a local heterogeneity within a railway track. *Journal of Sound and Vibration.* **429** (2018), 45–62.

[107] S. L. Grassie. Dynamic modelling of concrete railway sleepers. *Journal of Sound and Vibration.* **187**(5) (1995), 799–813.

[108] Z. G. Li and T. X. Wu. Modelling and analysis of force transmission in floating-slab track for railways. *Proceedings of the Institution of Mechanical Engineers, Part F: Journal of Rail and Rapid Transit.* **222**(1) (2008), 45–57.

[109] W. Zhai, K. Wang and C. Cai. Fundamentals of vehicle–track coupled dynamics. *Vehicle System Dynamics.* **47**(11) (2009), 1349–1376.

[110] X. Yang et al. Effect of track irregularity on the dynamic response of a slab track under a high-speed train based on the composite track element method. *Applied Acoustics.* **99** (2015), 72–84.

[111] E. Aggestam, J. C. O. Nielsen and R. Bolmsvik. Simulation of vertical dynamic vehicle–track interaction using a two-dimensional slab track model. *Vehicle System Dynamics.* **56**(11) (2018), 1633–1657.

[112] W. Zhai et al. High-speed train–track–bridge dynamic interactions – Part I: theoretical model and numerical simulation. *International Journal of Rail Transportation.* **1**(1-2) (2013), 3–24.

[113] S. Zhu and C. Cai. Stress intensity factors evaluation for through-transverse crack in slab track system under vehicle dynamic load. *Engineering Failure Analysis.* **46** (2014), 219–237.

[114] E. Poveda et al. A numerical study on the fatigue life design of concrete slabs for railway tracks. *Engineering Structures.* **100** (2015), 455–467.

[115] E. Aggestam and J. C. O. Nielsen. Simulation of vertical dynamic vehicle–track interaction using a three-dimensional slab track model. *Engineering Structures.* **222** (2020), 110972.

[116] J. S. Theyssen et al. Calibration and validation of the dynamic response of two slab track models using data from a full-scale test rig. *Engineering Structures.* **234** (2021), 111980.

[117] J. S. Theyssen, A. Pieringer and W. Kropp. "The Influence of Track Parameters on the Sound Radiation from Slab Tracks". *Noise and Vibration Mitigation for Rail Transportation Systems.* Ed. by G. Degrande et al. Vol. 150. Notes on Numerical Fluid Mechanics and Multidisciplinary Design. Cham: Springer International Publishing. 2021, pp. 90–97.

[118] P. Galvín, A. Romero and J. Domínguez. Fully three-dimensional analysis of high-speed train–track–soil-structure dynamic interaction. *Journal of Sound and Vibration.* **329**(24) (2010), 5147–5163.

[119] W. Zhai et al. Experimental investigation into ground vibrations induced by very high speed trains on a non-ballasted track. *Soil Dynamics and Earthquake Engineering.* **72** (2015), 24–36.

[120] D. J. Thompson, C. J. C. Jones and N. Turner. Investigation into the validity of two-dimensional models for sound radiation from waves in rails. *The Journal of the Acoustical Society of America.* **113**(4) (2003), 1965–1974.

[121] D. Duhamel. Efficient calculation of the three-dimensional sound pressure field around a noise barrier. *Journal of Sound and Vibration.* **197**(5) (1996), 547–571.

[122] S. N. Chandler-Wilde. The boundary element method in outdoor noise propagation. *Institute Of Acoustics Proceedings.* Institute of Acoustics Proceedings **19**(8) (1997), 27–50.

[123] X. Zhang, G. Squicciarini and D. J. Thompson. Sound radiation of a railway rail in close proximity to the ground. *Journal of Sound and Vibration.* **362** (2016), 111–124.

[124] X. Sheng, T. Zhong and Y. Li. Vibration and sound radiation of slab high-speed railway tracks subject to a moving harmonic load. *Journal of Sound and Vibration.* **395** (2017), 160–186.

[125] H. Li et al. Using a 2.5D boundary element model to predict the sound distribution on train external surfaces due to rolling noise. *Journal of Sound and Vibration.* **486** (2020), 115599.

[126] E. Ntotsios, D. J. Thompson and M. Hussein. The effect of track load correlation on ground-borne vibration from railways. *Journal of Sound and Vibration.* **402** (2017), 142–163.

[127] N. Vincent et al. Theoretical optimization of track components to reduce rolling noise. *Journal of Sound and Vibration.* **193**(1) (1996), 161–171.

[128] J. C. O. Nielsen. Acoustic optimization of railway sleepers. *Journal of Sound and Vibration.* **231**(3) (2000), 753–764.

[129] X. Zhang, D. J. Thompson and G. Squicciarini. Sound radiation from railway sleepers. *Journal of Sound and Vibration.* **369** (2016), 178–194.

[130] G. W. C. Kaye and E. J. Evans. The sound-absorbing properties of some common out-door materials. *Proceedings of the Physical Society.* **52**(3) (1940), 371–379.

[131] M. E. Delany and E. N. Bazley. Acoustical properties of fibrous absorbent materials. *Applied Acoustics.* **3**(2) (1970), 105–116.

[132] Y. Champoux and M. R. Stinson. On acoustical models for sound propagation in rigid frame porous materials and the influence of shape factors. *The Journal of the Acoustical Society of America.* **92**(2) (1992), 1120–1131.

[133] K. Attenborough, I. Bashir and S. Taherzadeh. Outdoor ground impedance models. *The Journal of the Acoustical Society of America.* **129**(5) (2011), 2806–2819.

[134] K. Heutschi. Sound Propagation over Ballast Surfaces. *Acta Acustica united with Acustica.* **95**(6) (2009), 1006–1012.

[135] R. A. Broadbent, D. J. Thompson and C. J. C. Jones. The acoustic properties of railway ballast. *Euronoise 2009.* (2009), 10.

[136] X. Zhang, D. J. Thompson and G. Squicciarini. Effects of Railway Ballast on the Sound Radiation From the Sleepers (2015), 6.

[137] Q. Li, X. Song and D. Wu. A 2.5-dimensional method for the prediction of structure-borne low-frequency noise from concrete rail transit bridges. *The Journal of the Acoustical Society of America.* **135**(5) (2014), 2718–2726.

[138] Q. Li and D. J Thompson. Prediction of rail and bridge noise arising from concrete railway viaducts by using a multilayer rail fastener model and a wavenumber domain method. *Proceedings of the Institution of Mechanical Engineers, Part F: Journal of Rail and Rapid Transit.* **232**(5) (2018), 1326–1346.

[139] E. Schneider, K. Popp and H. Irretier. Noise generation in railway wheels due to rail-wheel contact forces. *Journal of Sound and Vibration.* **120**(2) (1988), 227–244.

[140] C.-M. Nilsson. Waveguide finite elements applied on a car tyre. Doctoral thesis. Stockholm: Royal Institute of Technology, 2004.

[141] S. Finnveden and M. Fraggstedt. Waveguide finite elements for curved structures. *Journal of Sound and Vibration.* **312**(4-5) (2008), 644–671.

[142] P. Sabiniarz and W. Kropp. A waveguide finite element aided analysis of the wave field on a stationary tyre, not in contact with the ground. *Journal of Sound and Vibration.* **329**(15) (2010), 3041–3064.

[143] J. Fayos et al. An Eulerian coordinate-based method for analysing the structural vibrations of a solid of revolution rotating about its main axis. *Journal of Sound and Vibration.* **306**(3) (2007), 618–635.

[144] L. Baeza et al. High frequency railway vehicle-track dynamics through flexible rotating wheelsets. *Vehicle System Dynamics.* **46**(7) (2008), 647–659.

[145] L. Baeza et al. Prediction of rail corrugation using a rotating flexible wheelset coupled with a flexible track model and a non-Hertzian/non-steady contact model. *Journal of Sound and Vibration.* **330**(18-19) (2011), 4493–4507.

[146] A. Pieringer, L. Baeza and W. Kropp. "Modelling of Railway Curve Squeal Including Effects of Wheel Rotation". *Noise and Vibration Mitigation for Rail Transportation Systems.* Ed. by J. C. O. Nielsen et al. Vol. 126. Notes on Numerical

Fluid Mechanics and Multidisciplinary Design. Berlin, Heidelberg: Springer Berlin Heidelberg. 2015, pp. 417–424.

[147] P. T. Torstensson, J. C. O. Nielsen and L. Baeza. Dynamic train–track interaction at high vehicle speeds—Modelling of wheelset dynamics and wheel rotation. *Journal of Sound and Vibration.* **330**(22) (2011), 5309–5321.

[148] S. Vidoli and F. Vestroni. Veering Phenomena in Systems With Gyroscopic Coupling. *Journal of Applied Mechanics.* **72**(5) (2004), 641–647.

[149] L. Baeza et al. Eulerian models of the rotating flexible wheelset for high frequency railway dynamics. *Journal of Sound and Vibration.* **449** (2019), 300–314.

[150] X. Sheng, Y. Liu and X. Zhou. The response of a high-speed train wheel to a harmonic wheel-rail force. *Journal of Physics: Conference Series.* **744** (2016), 012145.

[151] A. F. Seybert et al. A special integral equation formulation for acoustic radiation and scattering for axisymmetric bodies and boundary conditions. *The Journal of the Acoustical Society of America.* **80**(4) (1986), 1241–1247.

[152] U. Fingberg. Ein Modell für das Kurvenquietschen von Schienenfahrzeugen. Fortschritt-Berichte VDI. Reihe 11, Schwingungstechnik. VDI Verlag. 1990. ISBN: 978-3-18-144011-7.

[153] T. Zhong et al. Vibration and sound radiation of a rotating train wheel subject to a vertical harmonic wheel–rail force. *Journal of Modern Transportation.* **26**(2) (2018), 81–95.

[154] G. Cheng et al. An investigation into the effects of modelling assumptions on sound power radiated froma high-speed train wheelset. *Journal of Sound and Vibration.* **495** (2021), 115910.

[155] F. Fabre et al. Sound radiation from railway wheels including ground reflections: A half-space formulation for the fourier boundary element method. *Journal of Sound and Vibration.* **493** (2021), 115822.

[156] H. Brick and M. Ochmann. A half-space BEM for the simulation of sound propagation above an impedance plane. *The Journal of the Acoustical Society of America.* **123**(5) (2008), 3418–3418.

[157] W. Kropp et al. On the sound radiation of a rolling tyre. *Journal of Sound and Vibration.* **331**(8) (2012), 1789–1805.

[158] B. N. Alemdar and P. Gülkan. Beams on generalized foundations: supplementary element matrices. *Engineering Structures.* **19**(11) (1997), 910–920.

[159] X. Zhang, D. J. Thompson and X. Sheng. Differences between Euler-Bernoulli and Timoshenko beam formulations for calculating the effects of moving loads on a periodically supported beam. *Journal of Sound and Vibration.* **481** (2020), 115432.

[160] C.-M. Nilsson and S. Finnveden. Input power to waveguides calculated by a finite element method. *Journal of Sound and Vibration.* **305**(4-5) (2007), 641–658.

[161] L. Cremer, M. Heckl and B. A. T. Petersson. Structure-Borne Sound. Berlin, Heidelberg: Springer Berlin Heidelberg. 2005.

[162] I. Karasalo. Exact Finite Elements for Wave Propagation in Range-Independent Fluid-Solid Media. *Journal of Sound and Vibration.* **172**(5) (1994), 671–688.

[163] T. Wu. Boundary Element Acoustics. WIT Presss. 2000. ISBN: 978-1-85312-570-6.

[164] F. Wullens and W. Kropp. Wave content of the vibrating filed of a rolling tyre. *Acta Acustica united with Acustica.* **93** (2007), 48–56.

[165] B. Soenarko. A boundary element formulation for radiation of acoustic waves from axisymmetric bodies with arbitrary boundary conditions. *The Journal of the Acoustical Society of America.* **93**(2) (1993), 631–639.

[166] P. M. Juhl. The Boundary Element Method for Sound Field Calculations. Doctoral thesis. Copenhagen: Technical University of Denmark, 1993.

[167] Earl G. Williams. Fourier Acoustics: Sound Radiation and Nearfield Acoustical Holography. Academic Press. 1999.

[168] A. Politis. Microphone array processing for parametric spatial audio techniques. Doctoral thesis. Aalto University, 2016.

[169] D. J. Thompson et al. Assessment of measurement-based methods for separating wheel and track contributions to railway rolling noise. *Applied Acoustics.* **140** (2018), 48–62.

[170] EN 15461:2008 Railway applications – Noise emission – Characterisation of the dynamic properties of track sections for pass by noise measurements.

[171] W. Zhai et al. Full-scale multi-functional test platform for investigating mechanical performance of track–subgrade systems of high-speed railways. *Railway Engineering Science.* **28**(3) (2020), 213–231.

[172] M. Wang et al. Experimental study on dynamic performance of typical nonballasted track systems using a full-scale test rig. *Proceedings of the Institution of Mechanical Engineers, Part F: Journal of Rail and Rapid Transit.* **231**(4) (2017), 470–481.

[173] A. Pieringer and W. Kropp. Model-based estimation of rail roughness from axle box acceleration. *Applied Acoustics.* **193** (2022), 108760.

[174] J. Theyssen. RailRad - calculate the acoustic radiation from railway track using pre-calculated transfer functions. URL: `https://github.com/janniktheyssen/railrad` (visited on 06/28/2022).

[175] J. Theyssen. *Database for RailRad calculation method for simulating sound radiated by railway track vibrations.* Dataset Version 1.0.0. Chalmers University of Technology, 2022. DOI: `10.5281/zenodo.6772099`.

[176] A. Pieringer et al. "Acoustic Monitoring of Rail Faults in the German Railway Network". *Noise and Vibration Mitigation for Rail Transportation Systems*. Ed. by G. Degrande et al. Vol. 150. Notes on Numerical Fluid Mechanics and Multidisciplinary Design. Cham: Springer International Publishing. 2021, pp. 242–250.

[177] T. X. Wu and D. J. Thompson. Vibration analysis of railway track with multiple wheels on the rail. *Journal of Sound and Vibration.* **239**(1) (2001), 69–97.

[178] C. Zang, H. Grafe and M. Imregun. Frequency–domain criteria for correlating and updating dynamic finite element models. *Mechanical Systems and Signal Processing.* **15**(1) (2001), 139–155.

[179] A. Zangeneh et al. Dynamic Stiffness Identification of Portal Frame Bridge–Soil System using Controlled Dynamic Testing. *Procedia Engineering.* **199** (2017), 1062–1067.

A Appendix to Chapter 3

A.1 Optimisation of the spatial inverse Fourier integral for the rail

Section 3.3.1 presents a method for semi-analytically integrating (3.39) to get a spatial representation of the sound field radiated by the rail. The term $p(\kappa, \omega)$ is largely determined by the surface velocity, which can have a large dynamic range, and so the intervals need to be small in proximity to the wavenumber κ_c in the structure. This section describes an algorithm to generate these intervals.

Each interval is described by two surrounding integration points. These are defined based on the desired number of integration points (n_{ip}) and the minimum and maximum distance ($\kappa_{\min}$ and $\kappa_{\max}$) from k_c. Figure A.1 shows an example of such a distribution around 4 rad/m, with $\kappa_{\max}$=4.5 rad/m and n_{ip}=19. First, a geometrically spaced series of $(n_{\text{ip}})/2 - 1$ numbers is generated between $\kappa_{\min}$ to $\kappa_{\max}$ (I). The distance between the numbers thus increases logarithmically towards $\kappa_{\max}$. Then, a negative copy of all values is added to the list of numbers, as well as the number zero (II, III). The list now contains values between -$\kappa_{\max}$ and $\kappa_{\max}$, with a narrow spacing around 0 rad/m. Finally, k_c is added to each number resulting in a symmetrical spacing of the values around the desired peak in the wavenumber spectrum (IV). If the integration is carried out only over the positive side of the wavenumber spectrum, negative values can be neglected or multiplied with -1. The wavenumber k_c needs to be chosen such that it corresponds with the highest surface velocity in the rail, for example at the the vertical bending wave for a beam bending model.

If several wave types exist (as is the case for a WFE-based rail), each can be surrounded with this distribution. The distributions can overlap, and so no adapted weighting function of the integration points is used. For models with a single wave type, it is possible that a more appropriate weighting function produces more accurate results with less integration points, but this has not been investigated. The three parameters n_{ip}, $\kappa_{\min}$ and $\kappa_{\max}$ need to be selected based on the properties of $p(\kappa, \omega)$.

An optimisation of these parameters was carried out, however, instead of (3.39), the

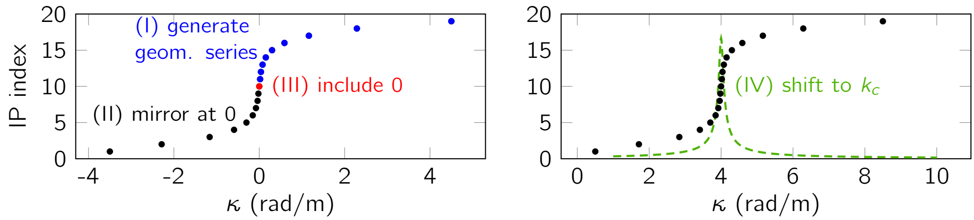

Figure A.1: Example distribution of integration points around $k_c = 4$ rad/m.

Table A.1: Parameters for continuously supported Euler-Bernoulli rail

Rail bending stiffness	EI	6.4 MNm^2
Rail mass per unit length	m'	60 kg
Rail damping loss factor	η_r	0.001
Pad stiffness per unit length	s'	216 MN/m
Pad damping loss factor	η_s	0.2

integral expression for calculating the transfer mobility of a continuously supported Euler-Bernoulli beam based on was used,

$$Y^{\mathrm{int}}(x) = \frac{j\omega}{2\pi} \int_{-\infty}^{\infty} \frac{\mathrm{e}^{-jkx}}{EIk^4 + s - m'\omega^2} \mathrm{d}k \tag{A.1}$$

which can be evaluated using a Riemann sum comparable to the original problem. The variables are presented in Table A.1. The beam model is used for three reasons: With its oscillatory term multiplied with a more slowly varying function, this expression is qualitatively comparable. More importantly, this optimisation of the integration points is only necessary because of the poles in the integrand of underlying rail models such as this one. And finally, the integration can be solved by sum of residues [23],

$$Y^{\mathrm{res}}(x) = \frac{\omega}{4EIk_p^3} \left(\mathrm{e}^{-jk_p x} - j\mathrm{e}^{-k_p x}\right) \text{ for } x \geq 0 \tag{A.2}$$

which eliminates the need for solving the integral numerically and serves as the reference in the following. The variable k_p refers to propagating waves as described in [23].

As a first step, n_{ip} is set to 101 which was empirically found suitable. The bounds $\kappa_{\min}$ and $\kappa_{\max}$ are investigated using a parametric investigation and a genetic algorithm. The transfer functions calculated via (A.1) and (A.2) are compared using the Frequency Response Assurance Criterion (FRAC) and Frequency Amplitude Assurance Criterion (FAAC) as described in [178, 179]. Both criteria approach unity for vanishing differences between the frequency spectra produced by both integration methods. The index i corresponds to the index of the location x at which the integrals are evaluated, which is done in steps of 25 m from 0 m to (and including) 100 m. A frequency range from 0 Hz to 7 kHz with a frequency step of 5 Hz is chosen.

The combined criterion ϵ

$$\epsilon = \sum_{i=1}^{5} ((FRAC_i - 1)^2 + (FAAC_i - 1)^2) \tag{A.3}$$

produces a single-value indicator for the quality of the integration, which is to be minimized in the optimization [179]. Figure A.2 shows this indicator for combinations of $\kappa_{\min}$ and $\kappa_{\max}$. It is visible that an optimum combination of both parameters exists. A genetic algorithm was therefore used to find this optimum point, with only the two variables $\log_{10}(\kappa_{\min})$ and $\log_{10}(\kappa_{\max})$. The genetic algorithm was implemented in the software

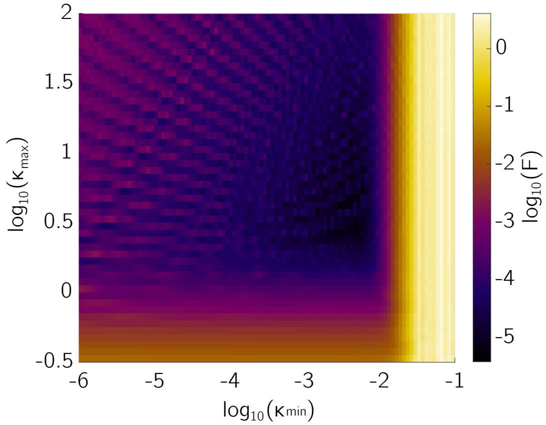

Figure A.2: The indicator for the quality of integration F for $n_{\mathrm{ip}} = 101$.

MATLAB using the `ga` function. In 52 generations, the genetic algorithm converged to a mean fitness value of $2.3 \cdot 10^{-5}$ for the settings $\log_{10}(\kappa_{\mathrm{min}})$ = -2.31 and $\log_{10}(\kappa_{\mathrm{max}})$ = 0.51, which matches the expected optimum from Figure A.2. Note that these bounds depend on the shape of the peak and therefore, among others, on the material damping in the rail.

Including n_{ip} in the optimisation is not meaningful as it converges to the upper bound. To investigate its effect, the indicator value ϵ was evaluated using the bounds κ_{min} and κ_{max} found in the genetic algorithm for different numbers of integration points. Figure A.3 shows that a doubling of the number of integration points leads to a decrease of ϵ in the order of a magnitude, up to about 120 integration points.

Table A.2: Parameters used in the genetic algorithm

	lower bound	upper bound	result
$\log_{10}(\kappa_{\min})$	-15	1	-2.31
$\log_{10}(\kappa_{\max})$	-1	3	0.5

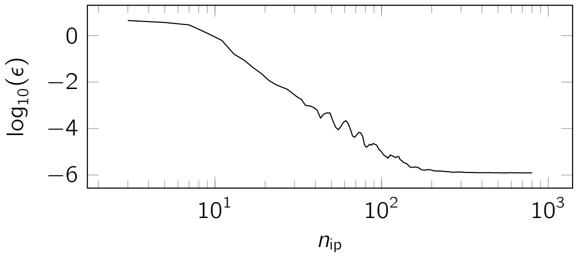

Figure A.3: Quality of integration in dependency of the number of integration points when using the resulting $\kappa_{\min}$ and $\kappa_{\max}$ found in the genetic algorithm.

A.2 Validation of the method for calculating the 3D sound field from 2D solutions

To investigate the validity of the modelling approach described in Section 3.2.2, comparisons to the standard WBEM and an analytical solution for the case of a breathing cylinder are carried out. Figure A.4 presents the cross-section of the geometry. The

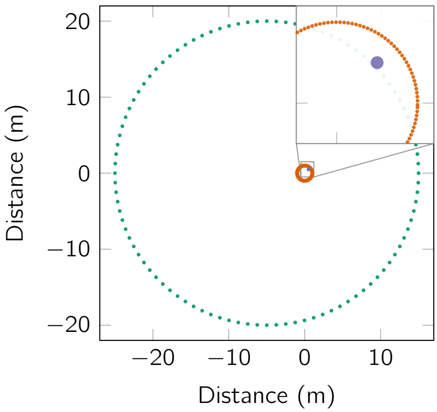

Figure A.4: Cross-section of the setup for the validation calculation. The thick blue dot marks the location of the line source. The smaller, orange circle represents the surface of the WBE structure while the larger, green circle of points are positions at which the sound pressure is evaluated.

analytical model is based on a breathing line source, located at $(0.5, 0.5)$ m. Assuming a

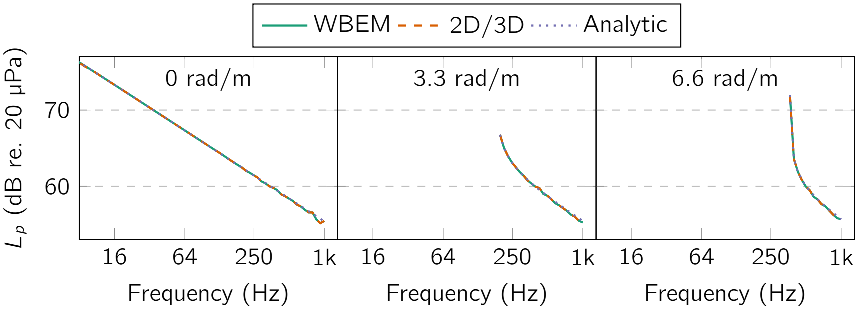

Figure A.5: Calculated pressure at one field point. The wavenumber κ along the structure is given in the top right corner.

unit pressure excitation $\hat{p} = 1\ Pa$, the pressure produced by this source at any location in the field is given by

$$p = -\frac{j}{4}\hat{p}\mathrm{H}_0^{(2)}(\alpha r) \tag{A.4}$$

where r describes the distance between source and receiver.

The radiating surface in the WBEM model consists of a cylinder with 1 m radius centred at $(0, 0)$ m, enclosing the line source. Its surface normal velocity at each element of this cylinder v_n is prescribed such that it matches the velocity in the sound field created by the breathing cylinder.

$$v_n = \frac{\alpha}{4\omega\rho} H_1^{(2)}(\alpha r)\frac{\partial r}{\partial n} \tag{A.5}$$

where r is the distance from the breathing line source to the element, n is the unit normal vector on the boundary. This way, the pressure on and outside of the surface of the cylinder should be identical up to numerical accuracy, within the general limitations of the Boundary Element method. Finally, the WBE model is used to solve the 2D BE problem described in (3.30) for $\kappa_0 = 1$ µ rad/m and a frequency spectrum from 0 Hz to 1000 Hz and a resolution of 2 Hz. The sound pressure on the surface and in the field at other wavenumbers is then calculated using the method introduced above.

Frequency spectra of the sound pressure are calculated for three wavenumbers at 120 receiver points which are arranged in a circle with 20 m radius centred at $(-5, 0)$ m. Firstly, the sound pressure at one such receiver is compared for all three methods in Figure A.5. The three models produce very similar results. The effect of the cut-on frequency at higher wavenumbers is visible for $\kappa = 3.3$ rad/m and $\kappa = 6.6$ rad/m, as no radiation into the far field occurs below 182 Hz and 364 Hz, respectively.

In a second step, the WBEM calculation and the presented method are compared to the analytical model. Figure A.6 presents the mean error of each receiver point. Both methods predict the analytical result with high accuracy. A decreasing accuracy with increasing frequency is expected due to the resolution of the BE mesh, which is observed for both methods. Once can conclude that the suggested approach is a suitable extension to the WBEM when dense frequency and wavenumber spectra are calculated.

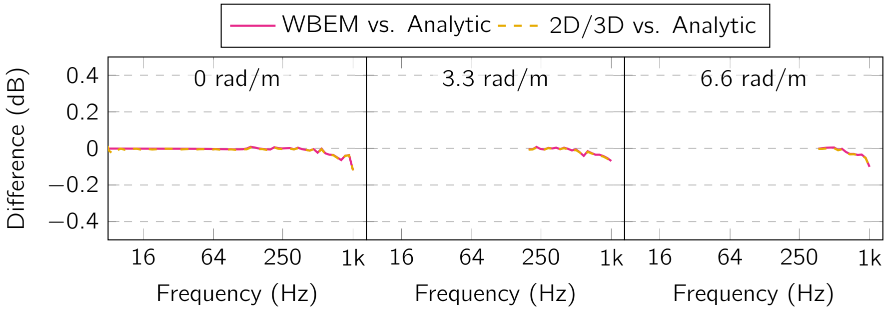

Figure A.6: Comparison of the mean difference at all field points.

A.3 Modelling railway sleepers flush with the surrounding plane

It is convenient to model the sleeper surface flush with the surrounding plane when modelling of the sleeper sound radiation. This is common practise, see for example [23, 75]. However, Nielsen [128] observed minor differences in the radiation efficiency between a 3D sleeper geometry in a finite, 1.5 m x 1.5 m baffle compared to a 2D piston in an infinite baffle. In reality, the sleeper protrudes a few centimetres from the plane in the case of a system with booted sleepers, or up to the height of a standard sleeper for a ballasted track. The wavenumber-domain formulation of sleeper radiation presented in Section 5.6.3 requires that the sleepers are modelled flush with the the surface.

To quantify the effect of the protrusion, a simple box with the width and depth comparable to a single booted sleeper (0.3 m x 0.78 m) and variable height was modelled in the in-house software BEMLab [156]. The top and bottom of the box were prescribed with a constant velocity v in outward direction, simulating the effect of half the box height h placed in an infinite baffle. The sound pressure was calculated on a sphere around the box, from which the sound power P radiated by the box was derived. From this, the radiation ratio σ was obtained as

$$\sigma = \frac{P}{\rho_0 c_0 S \overline{\langle v \rangle}} \tag{A.6}$$

with the density in air ρ_0, the speed of sound in air c_0 and the spatially and temporally averaged normal velocity $\overline{\langle v \rangle}$ over the surface S. Figure A.8 shows the radiation ratio for different protrusions h. The height of the sleeper only marginally affects the radiation ratio.

A comparison of the directivity is shown in Figure A.9. While at 50 Hz there is minor spread between the curves, differences of about 5 dB are observed at 200 Hz and 400 Hz. Further, it is observed that the radiation pattern becomes more directive with increasing frequency. At 800 Hz there is a large spread of over 10 dB at two angles. The maximum spread over frequency and angle is quantified in Figure A.10. At around 450 Hz, certain

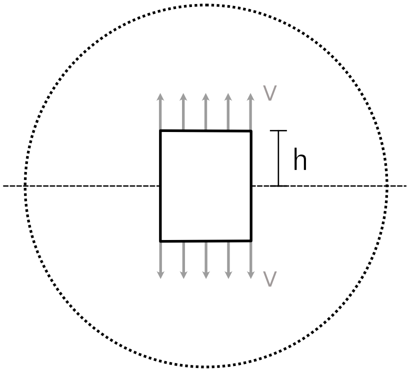

Figure A.7: Sketch of the cross-section of the 3D BEM model for investigating the effect of the protrusion of the sleeper through the infinite baffle. The top and bottom of the central box have a prescribed normal velocity v. The sound pressure is evaluated on a sphere with 30 m radius around the structure.

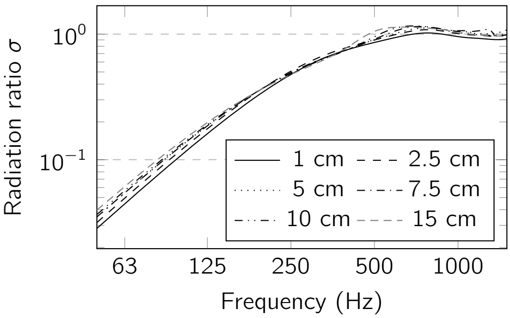

Figure A.8: Radiation efficiency σ for different heights of the sleeper.

angles emerge which the spread is maximum. Here, the wavelength in air is the same range as the dimensions of the object, leading to interference from the two sides of the object. When the sound radiation from the sleepers is limited to low frequencies, a flush model for the sleepers can be acceptable.

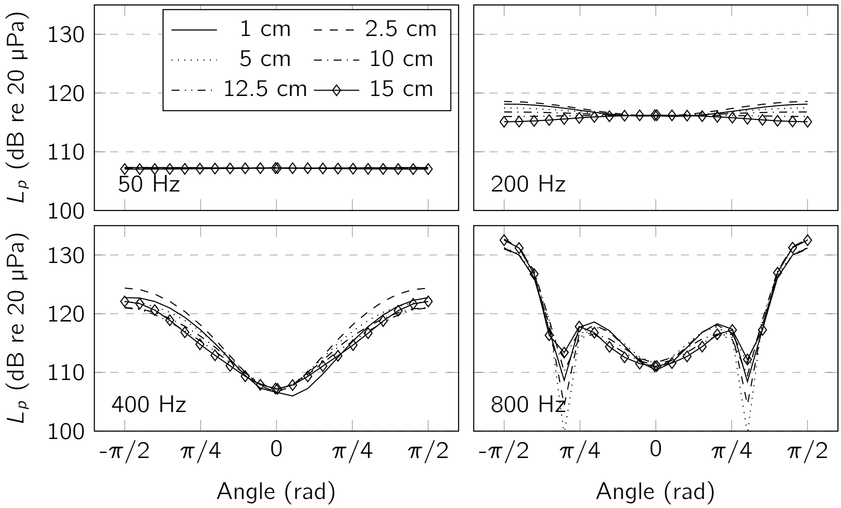

Figure A.9: Directivity of a rectangular piston protruding an infinite baffle with different heights at selected frequencies.

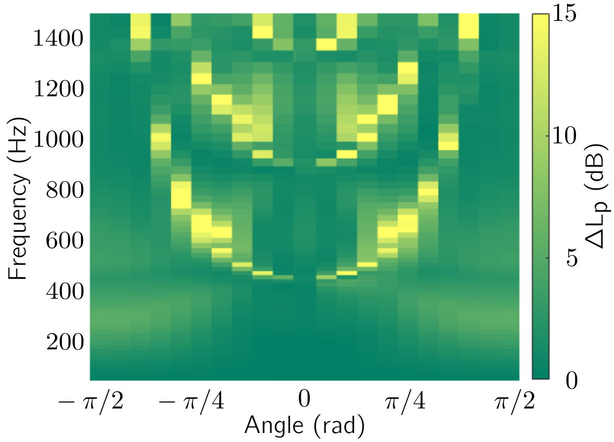

Figure A.10: Maximum sound pressure difference between the sleepers with different heights over frequency and angle.